Passive Binary-Modulated Backscatter in Microwave Networks with Applications to RFID

by

Daniel Gregory Kuester

B.S., University of Colorado, 2007

B.M., University of Colorado, 2007

M.S., University of Colorado, 2010

A thesis submitted to the

Faculty of the Graduate School of the

University of Colorado in partial fulfillment

of the requirements for the degree of

Doctor of Philosophy

Department of Electrical, Computer and Energy Engineering

2012

This thesis entitled:

Passive Binary-Modulated Backscatter in Microwave Networks with Applications to RFID

written by Daniel Gregory Kuester

has been approved for the Department of Electrical, Computer and Energy Engineering

_____

Zoya Popović

_____

Dr. Josh Gordon

Date _____

The final copy of this thesis has been examined by the signatories, and we

Find that both the content and the form meet acceptable presentation standards

Of scholarly work in the above mentioned discipline.

Kuester, Daniel Gregory (Ph.D., Electrical Engineering)

Passive Binary-Modulated Backscatter in Microwave Networks with Applications to RFID

Thesis directed by Professor Zoya Popović

This thesis solves the problem of inexpensive performance test and characterization for passive binary backscatter communication. The approach examines link behavior in realistic environments, measurable performance metrics to characterize this behavior, and testbed design for accurate test and measurement of these parameters. The ultimate goal is to improve system design practices and support test standard development.

The principal result is a theory of backscatter signaling based on linear microwave network theory that is suitable for metrology, test engineering, and link analysis. The parameter is simple and clearly defined for measurement and link analysis suitable in any linear propagation environment including free space, line-of-sight, and deep fading. The theory is built on a clearly defined and justified BPSK definition for arbitrary binary-modulated backscatter power. A measurable figure of merit is developed that gives an absolute lower bound on the modulation power in backscatter received by monostatic transceivers from passive transponders.

The concepts are applied to passive monostatic UHF RFID operating in the far-field, which is the most common use of passive backscatter. Measurements of commercial RFID readers and tags validate the theory and confirm the utility of the figure of merit defined by this thesis. This becomes the basis for a simple new method for specifying RFID device performance to maximize communication speed by optimizing the backscatter link. The approach developed here is expected to gain importance in the future as backscatter losses increase because of increased passive RFID communication range increases.

Dedication

To my wife Kirsten. Thanks!

Acknowledgments

Professor Zoya Popović, my doctoral thesis advisor in the Electrical, Computer and Energy Engineering Department at the University of Colorado, has overseen this writing and counseled my professional development. The other students in her research group have been excellent friends and collaborators. Prof. Dejan Filipovic also offered valuable advice as my masters degree academic advisor. Profs. Tim Brown and Albin Gasiewski, were also kind to spend their time serving on my thesis committee.

These professors and countless others here at the university also contributed to my professional development through hard work teaching during the past ten years. My education did not start at the university, and I owe a lot of my career direction and interests to Roger Briggs, former physics teacher at Fairview High School, and Brad White, former algebra teacher at Burbank Middle School (now at Fairview). My less formal education in computers as powerful tools began in high school under the tutelage of my good friend David Trowbridge, to whom I also owe an extended debt.

David Novotny and Jeff Guerrieri, with the RF fields group in the NIST electromagnetics division, hired me to support the RFID project in the summer of 2007. They have supported and encouraged my work, and its dissemination at conferences and in journals. Mr. Novotny was careful not to reflect too much of his own grad school experience on me. Dr. Perry Wilson and Dr. Josh Gordon, also with the RF fields group, surpassed their normal responsibilities at NIST by serving on my thesis committee. Dr. Gordon, in particular, took extra time to represent the interests of NIST during my meetings with Prof. Popović. Dr. Randy Direen and Jason Coder were also very helpful when I needed an extra pair of hands. Dr. Michael Souryal, with NIST in Gaithersburg, MD, and Dr. Leonardo Rinzani, in Building 1, were also very enjoyable to work with.

Bert Coursey, recently retired from the Office of Science and Technology at the U. S. Department of Homeland Security, personally ensured the funding of this work that lasted the duration of my graduate career. I wish him a happy retirement.

Christoph Rosol, formerly with the Max Plank Institute for the History of Science, was extremely helpful and informative about my historical queries.

The valuable support from my family and friends has made this endurance activity fulfilling and sustainable for the past five and a half years. My parents deserve special blame for rearing their firstborn in an environment that gave the impression this kind of thing could be a good idea. My sisters prevented anything from going to my head, and humored my short foray into constitutional law.

My lovely wife Kirsten has been wonderful and patient and supportive. I borrowed some motivation from her to write this, but now she can have it back. I'll return the favor with a bit of strength for the next months.

Dan Kuester, December 2012

Contents

List of Tables

List of Figures

List of Acronyms

AIDC automatic identification and data capture

AWGN additive white gaussian noise

ASK amplitude-shift keying

BER bit error rate

BLF base link frequency

BPSK binary phase-shift keying

BIPM Bureau International des Poids et Mesures

C1G2 class 1 generation 2

CRC cyclic redundancy check

CW continuous-wave

DUT device under test

EIRP effective isotropic radiated power

EPC electronic product code

FER frame error rate

FET field-effect transistor

IFF identify friend or foe

IQ in-phase and quadrature

LLRP low-level reader protocol

LNA low-noise amplifier

LO local oscillator

LP linearly-polarized

NIST National Institute of Standards and Technology

PLL phase-locked loop

PR-ASK phase-reversing amplitude-shift keying

PSD power spectral density

PSK phase-shift keying

RCS radar cross-section

RF radio frequency

RFID radio frequency identification

RSSI received signal strength indicator

RMS root mean square

SIR signal-to-interference ratio

SNR signal-to-noise ratio

UHF ultra-high frequency

UPC universal product code

Chapter 1

Introduction

If we steal thoughts from the moderns, it will be cried down as plagiarism; if from the ancients it will be cried up as erudition.

Charles Caleb Colton,

Lacon: or, Many things in few words (1824)

When you take stuff from one writer, it's plagiarism, but when you take it from many writers, it's called research.

John Burke (1938)

Stealing from one author is plagiarism; from many authors, research.

Walter Moers, *The City of Dreaming Books* (2007)

The goal of the work in this thesis is detailed development of analysis tools and measurement practices for ensuring adequate signal power in communication by binary-modulated backscatter. The approach is centered on testing with supporting network theory, and on connection and comparison to older work to shed light on some common inconsistencies in technical literature.

The dominant use of passive backscatter communication today is ultra-high frequency (UHF) radio frequency identification (RFID), specified in the (approximately) harmonized EPC Global Class 1 and

ISO/IEC 18000-6C communication standards [1, 2]. The passive backscatter theory and test methods developed here are applied extensively to passive UHF RFID to stay grounded in reality and offer immediate applicable benefits. Concepts in this thesis, however, apply more broadly to any communication based on passive binary-modulated backscatter.

1.1 Communication by Digitally-Modulated Backscatter

Backscatter for communication is uncommon. Receivers must detect weak backscatter modulation and reject strong interference leaked from the transmitter. This can be overcome in part by adding adaptive carrier cancellation at the cost of greater design complexity. Receiver hardware for "long-distance" backscatter communication (more than about 10 m) is therefore more complex than communication by transmission.

, Still, backscatter communication can benefit a transponder by use of very little power during communication.

1.1.1 Historical Work on Modulated Scattering

Scattered modulation sidebands can be caused by 1) Doppler shift, so that the radar receiver effectively detects radial motion between radar antennas and at least part of the target, or 2) deliberate design of a human-made target that modulates the reflections. In modern RFID, this is achieved by electronics attached to an antenna called load modulation.

Work during the second world war showed early interest in modulation sidebands scattered from both radar targets and loaded antennas. A significant problem to be solved was identify friend or foe (IFF) — discriminating between friendly and enemy aircraft on radar [3, pp. 119-122]. The German Luftwaffe first developed a crude approach to IFF: multiple aircraft performed synchronous roll maneuvers, collectively reflecting signature Doppler sidebands, but only toward the sides of the aircraft. By 1941, they replaced this method with an active transmitting IFF transponder on each aircraft, the FuG 25a Erstling, illustrated in Fig. 1.1a. Wattson-Watt in Britain tried load modulation with a dipole antenna stretched across the wings of a fighter aircraft in the late 1930s. By mechanically or electronically shorting and unshorting

the antenna over time, airmen would reflect signal codes to identify themselves to British radar operators. Received signals at radar stations were very weak, however, so (like the Germans) the British developed active transponders to transmit IFF codes.

Later work in more sensitive radar systems identified more sources of Doppler sidebands in electromagnetic reflections off of aircraft. These include mechanical vibrations [4] and rotating propellers [5]. These factors must be mitigated in modern stealth aircraft to minimize detectability to radar.

By the mid-1940s, Russian inventor Léon Theremin developed a covert passive spy device based on load modulation of acoustic audio [9][10, p. 7]. Soviet children presented the American ambassador in Moscow with a United States State Department seal, which he placed in his office at the embassy. Hidden inside the seal was an antenna loaded by a piezoelectric crystal. When illuminated by a powerful UHF radio source across the street, reflected signals from the antenna were modulated with the acoustic audio in the ambassador's office. The listening device later became known in the American press as "The Thing," pictured in Fig. 1.1b. Downconversion to audio with a direct conversion receiver let Soviet agents listen to conversations in the ambassador's office. Theremin's device was not discovered until the 1950s; even then, Britain had to reverse engineer it, after the United States government failed.

The first public literature on communication by backscatter was published by Harry Stockman in the late 1940s, working at what is now the Air Force Research Laboratories [8]. Presumably he did not know about Theremin's earlier work. Stockman discussed various approaches to load modulation and modulation by translating or rotating reflectors mechanically. Initial experiments demonstrated a mechanically rotated reflector approach, illustrated in Fig. 1.1c. The work was not sanctioned by the laboratory, and Stockman was fired for improper use of Air Force property soon after publishing his paper.

Load modulation also found use for field measurements, starting with Richmond's 1955 paper [11]. Measuring transmission power loss between an antenna and a probe required feed cables to each, perturbing the measured field. Applying load modulation to the probe's terminal with a compact battery powered device removes one of those cables at the expense of dynamic range, since the received modulation reflected from the modulation load is weak. The concept has more recently been extended (espe-

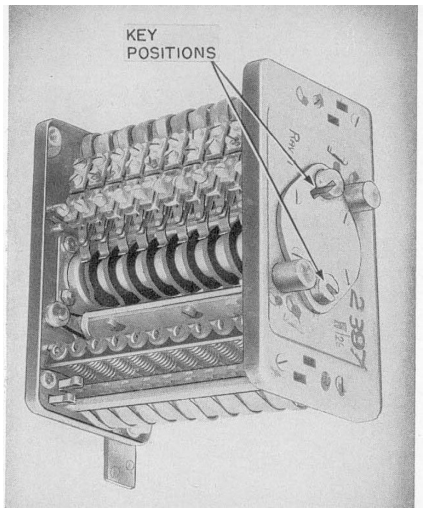

(a) Early 1940s

(b) Mid-1940s

(c) Late 1940s

Figure 1.1: Historical backscatter modulation devices: (a) The first German IFF system, the FuG 25a Erstling [6], (b) a replica of Léon Theremin's covert listening device "The Thing," [7] (c) Stockman's mechanically modulated backscatter device [8]

cially by Bolomey) for near-field imaging of biological tissues with arrays of modulated field probes or by mechanically scanning a single modulated field probe [12, pp. 1-30][13].

The first commercial applications of backscatter communication that are similar to RFID were patented in the mid-1970s [14]. These were targeted at inventory management, making them true precursors to modern RFID.

1.1.2 Physical Operation

Key optimization goals in passive backscatter are to 1) minimize power consumption and 2) maximize the proportion of incident power that can be reflected as a communication signal.

Circuits that realize simple communication by transmission and backscatter are compared in Fig. 1.2. Like up- and down-conversion in digital communication transmitters, the mixing process in backscatter modulation is represented as a mixer. Instead of the usual 3 ports for LO, RF, and baseband, however, the LO and RF become incident and reflected waves of a single combined port, so the "reflective mixer" has only 2 ports.

In wireless backscatter communication, the LO is broadcast over the air as the carrier. Because there is no other RF signal source, the reflected modulation from the reflective mixing in the transponder appears to the transceiver as shifted to the carrier frequency. Any other transponder in the transceiver antenna's field of view that mixes another signal with the carrier adds its own modulation to the backscatter signal received by the reader, causing interference.

Backscatter transponders, by receiving the LO over the air, do not need their own RF oscillator or phase-locked loop (PLL). Removing these circuits reduces power consumption and total area (and therefore cost) of a tag chip. The penalty is that backscatter received by readers from tags is weak, limiting communication range and increasing the complexity and cost of the transceiver. Thus, backscatter is well suited for short range communication where hardware cost and complexity are concentrated in the transceiver, and the transponder operates at very low power. Chapter 2 will show that received binary-modulated backscatter can always be classified as binary phase-shift keying (BPSK).

Operation at short range and very low power makes backscatter transponders well suited to operate

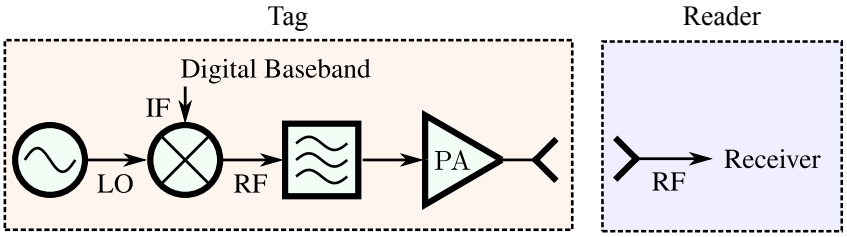

(a) Transmission topology (ASK)

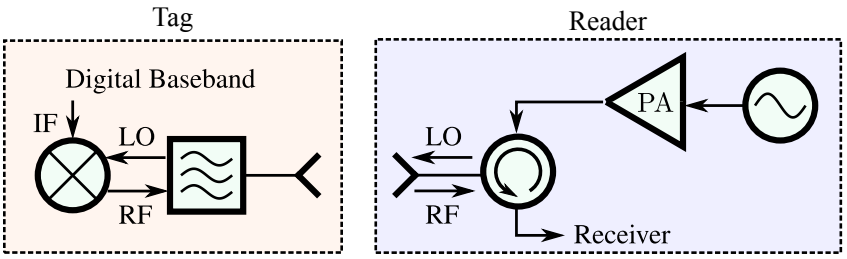

(b) Backscatter topology (load-modulated)

Figure 1.2: Circuit topologies of (a) active (transmitting) modulation and (b) passive (backscattering) modulation. The backscattering topology effectively moves the LO out of the transponder into the reader. The LO and RF signals in the backscatter modulation are incident and reflected waves sharing the same port.

passively by power harvesting. They may rectify some of the LO power to replace a battery as the DC power supply to form a fully passive transponder — further reducing tag chip size and cost. An alternative is a battery-assisted transponder, where the rectified LO helps recharge the battery. Power supply requirements also limit reader-to-tag link range, consistent with the short range of backscatter communication.

Digitally modulated backscatter can be realized by time-varying the impedance loading the transponder antenna. A simple approach to binary modulation, used in RFID, is adding a FET in shunt at the antenna load, so digital baseband data at the FET gate switches the antenna load between a short and another load. Very recent work has investigated other n-ary modulation schemes as far as 4QAM [15], and BPSK data rates as high as 30 Mbps [16].

1.2 Passive UHF RFID

The original stated purpose of passive UHF RFID was to automatically identify objects located near a door or a human operator. The purpose is like that of barcodes, but with some added ability:

(1) Longer operating range (sometimes more than 10 m);

(2) Operation without line of sight through dielectrics;

(3) Both reading and writing of a few kilobits to chips on tagged objects; and

(4) Faster inventory (up to a few hundred tags per second).

The ability to write data to a tag can give RFID systems a limited memory for the state of a tagged object without the need to consult a database. The memory could include physical location, sensor data like ambient temperature and pressure, or description of the tagged object.

1.2.1 RFID Product Taxonomy and Jargon

Wireless systems that are the focus of this document are sometimes called **EPC C1G2** or **ISO 18000-6C** RFID, after the standards that define their operation. These are approximately equivalent, in that

ISO 18000-6C is kept harmonized with the EPC standard. Both standards are interchangeable for the purposes of this thesis.

UHF RFID integrates work from several disciplines with different conventions and terminology: antenna design, power harvesting, digital communication, radar, semiconductors, digital and analog circuit design, and signal processing. In combining them, the RFID community has evolved its own jargon that is reviewed briefly below.

A **reader** (sometimes called an **interrogator**) is a **transceiver** which transmits and receives signals to communicate with tags. It "reads" data from any tags that respond, as its name implies, but can also write data to tags. Some new commercial reader products enable **localization**, estimating the position of the tag in space, with the phase of backscattered signals from tags and an array of reader receive antennas.

A reader that relies on cables for power and external antennas is known as a **fixed reader**, because it is typically immobile. In free space, these readers can communicate with the most sensitive passive tags beyond 12 m from their antennas when transmitting at 36 dBm effective isotropic radiated power (EIRP). A **mobile reader** (or **handheld reader**) is usually battery powered and integrated with a small antenna. Because batteries limit practical transmit power and smaller antennas have less gain, mobile readers usually can detect tags at significantly reduced range; as a correlary, research in this thesis demonstrates that these readers have less strict sensitivity requirements when operating with passive tags.

A **tag** is a transponder that receives signals from a reader and responds with requested data. These data are at minimum an identification number, but may also include user or sensor data stored in the tag's on-chip memory. Mass-produced tags embedded inside a human-readable paper label are called **inlays**, and are typically produced by the office paper industry.

The power supply for a tag may be either a battery, in which case it is an **active tag**, or the incident signal, in which case it is a **passive tag**. A fully active tag responds to reader communication by powered transmission out of its antenna. More power-constrained passive tags respond with **backscatter**, by modulating the impedance loading its antenna which creates modulation sidebands around reflections at the reader. When a tag with a battery communicates with backscatter to reduce power consumption, it is

known as a **battery-assisted passive (BAP) tag** or a **semi-passive tag**. The most common type of these tags in deployments is the passive tag, because it is least expensive.

1.2.2 Inventory and Automation in some Historical Context

The most basic motivation for RFID is to enable counting and tracking of collections of objects large enough to require inventory. Humans have counted goods and belongings for millenia. The "Ishango bone," pictured in Fig. 1.3, was excavated in 1950 by the Belgian professor J. de Heinzelin [17]. It is inscribed with ticks that demonstrate counting and possibly arithmetic. Archaeologists estimate that it is a few tens of thousands of years old.

Over the tens of millenia since, the human population has grown by orders of magnitude. The number of human-created objects has grown on a similar scale, thanks to industrialization and mass production. In the past century, automatic counting has become increasingly common place.

Some early automatic identification and data capture (AIDC) machines were electrically powered punchcard scanners that identified markings mechanically. One of the first was for the 1890 tabulating machine invented by Herman Hollerith, pictured in Fig. 1.4. The reader pulled pins across a punchcard above a grounded well of mercury, so that holes in the punchcard would short the pins. In 1890, United States federal government used this machine to tally its census of all 60 million citizens — an inventory of population. Each address was sent one punchcard, and each respondant mailed their card back to the Census Bureau in Washington, D.C. Punch cards grew in ubiquity for input and storage when digital computers were invented in the mid-20th century until magnetic storage and keyboards with video displays became increasingly common from the 1970s. Today, punch cards are still a highly visible part of the voting process in elections in the United States and other countries.

Mid-20th century work in optical identification techniques [22–24] resulted in barcodes. Use of the universal product code (UPC) for identifying consumer goods began in 1974. Widespread use of barcodes began to allow monitoring large inventories with computer databases, which were particularly useful for large organizations that could save the money by improving efficiency.

The somewhat vague term AIDC has recently been coined to encompass the practice of monitoring

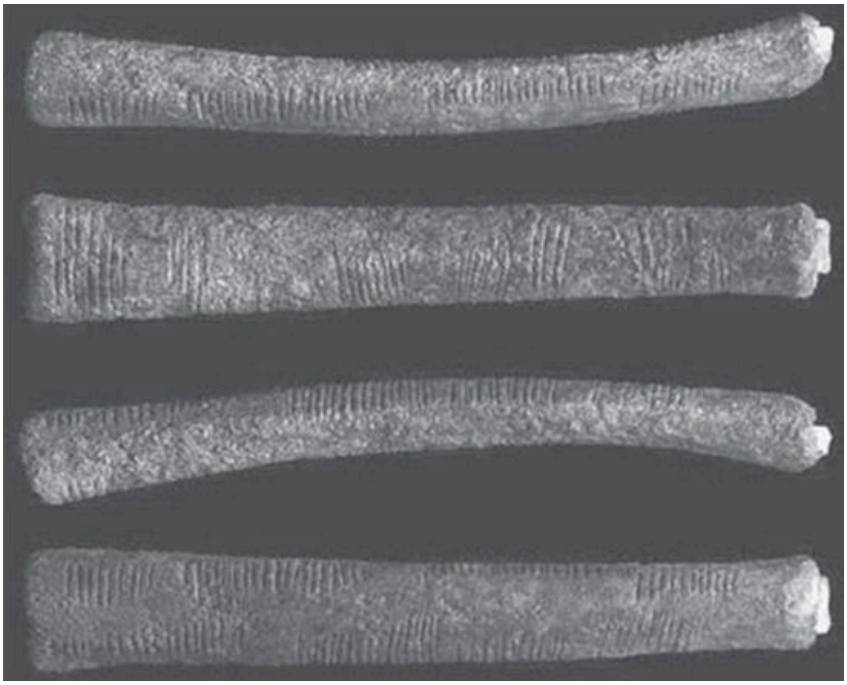

(a)

(b)

Figure 1.3: The (a) Lebombo bone, discovered in the 1970s near the Swaziland border [18, p. 12], and (b) Ishango bone, discovered in 1950 by J. de Heinzelin near the Nile headwaters. [19]. Both show prehistoric records of counting.

.

(a)

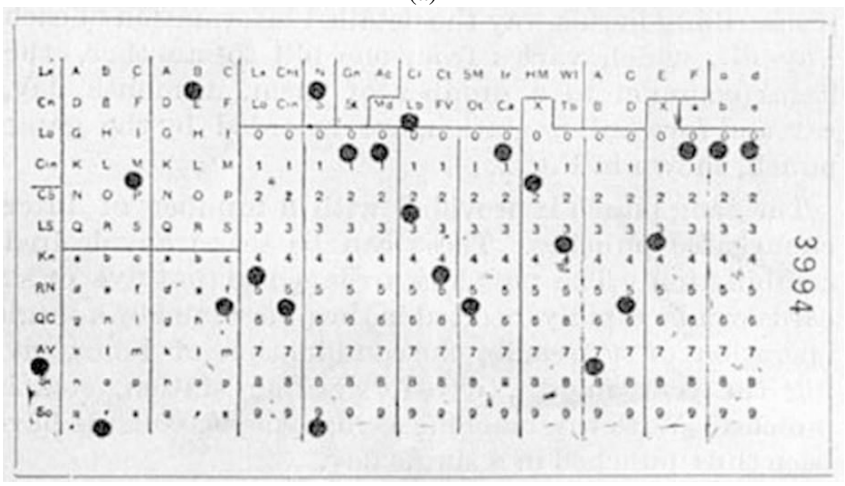

(b)

Figure 1.4: Herman Hollerith's 1890 punchcard reader in the Computer History Museum in Mountain View, CA, US. [20, 21].

.

	Physics	"Max Range"	Rewriteable	Typ. Storage
Punchcard	Mechanical	Contact	No	10^2 bit
UPC Barcode	Optical	$10^{-2} - 10^{-1}$ m	No	10^1 bit
QR Code, 33x33	Optical	$10^{-1} - 10^{0}$ m	No	10^3 bit
ISO 14443 RFID	RF (HF)	$10^{-2} - 10^{-1}$ m	Yes	$10^2 - 10^6$ bit
EPC RFID, C1G2	RF (UHF)	$10^{-1} - 10^{1}$ m	Yes	$10^2 - 10^3$ bit

Table 1.1: Comparison of AIDC tools based on human-made targets

and classifying these objects automatically by computer. Modern passive UHF RFID is often described as an example of AIDC. This term is often used in industry literature, but is not defined in an "official" way in standards. For this thesis, we can think of AIDC in broad terms as the class of tools that enable computers to rapidly absorb information about the physical world with little operator effort.

Modern digital imaging and computers have enabled image processing methods for AIDC that previously required "biological" intelligence: faces and objects in photographs, or written characters in human languages. Punchcards, barcodes, or RFID tags are examples of tools which gather data from human-made inputs that are mainly meaningful to machines. RFID tags are an extreme example — stored data is entirely inaccessible except to an RFID reader, which communicates with RF communication signals humans cannot directly sense.

Table 1.1 compares basic features of various AIDC tools that use human-made targets. Economic factors such as cost are an important constraint in the practical efficacy of each tool, but we exclude them because they are outside the technical scope of this thesis.

1.2.3 Physical Layer Operation

Passive UHF RFID employs bidirectional and half-duplex communication between a reader and a tag, illustrated by Fig. 1.5. The reader always initiates communication: first, the carrier to power up the field of tags, and then modulation with encoded commands. Compliant tags do not perform any backscatter modulation before a request by the reader. In the forward link, a reader antenna radiates a carrier wave within 860 MHz to 960 MHz. A tag reflecting digital modulation centered at the same frequency for reception by a reader forms the return link.

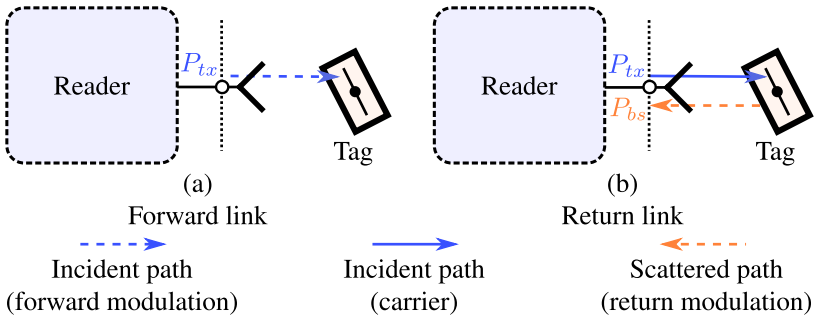

Figure 1.5: The two links of half-duplex ISO 18000-6C RFID communication, shown for the monostatic (shared transmit and receive antenna) case. In the forward link (a), a reader sends a modulated request to a tag, which rectifies the incident wave to power its circuitry. In the return link (b), the tag reflects a modulated reply to the reader.

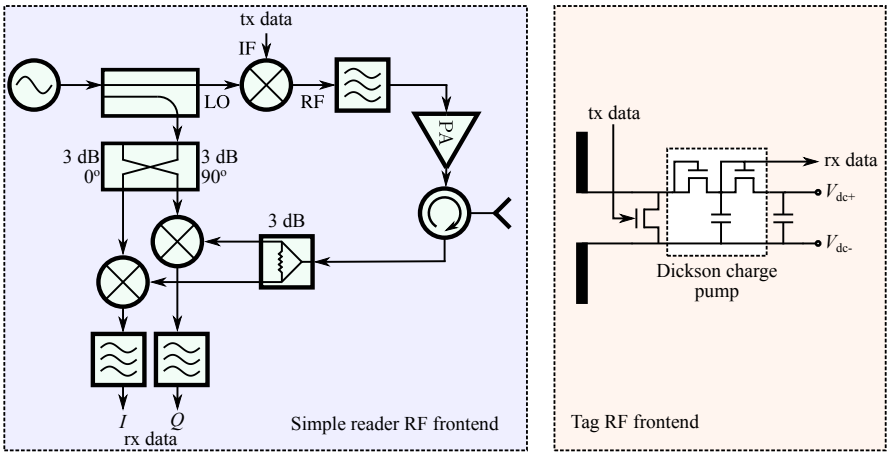

Figure 1.6: Examples of simple RF frontends for readers and tags. Forward link modulation is based on ASK, requiring only power envelope detection in the tag. Return link modulation is generated by shorting the tag antenna load to reflect back to the reader, which detects the backscatter with an IQ demodulator.

RF Hardware

Block diagrams of simple but functional RF frontends of passive UHF RFID hardware are shown in Fig. 1.6. Readers usually transmit between about 20 dBm to 30 dBm (peak) into an antenna with about 4 dBi to 8 dBi of gain. The lower bound of these numbers affects the desired read range and antenna beam width, and the upper end is determined by national regulations. In the United States and Europe, the product of these (sum of dB quantities) is limited to 35 dB to 36 dB, and available power into the reader antenna is limited to about 30 dBm. Modern passive UHF RFID tag chips need to absorb around -15 dBm to turn on. The transducer loss between a fixed reader's coaxial RF output and a tag chip is therefore limited to about 45 dB at 30 dBm transmit power or 35 dB loss at 20 dBm transmit power. This is discussed more in Chapter 3.

After a brief power-up period, the reader modulates the carrier with data according to RFID protocols at 40 kbps to 160 kbps. Modulation from the reader is usually amplitude-shift keying (ASK) or phase-reversal ASK (ASK with $180°$ phase shift between binary symbols). At a fixed data rate, phase-reversing amplitude-shift keying (PR-ASK) uses less bandwidth at a given data rate than the ASK. Standards also permit single-sideband ASK, but this is rare in practice because it requires a more expensive IQ modulator in the reader transmitter.

The tag rectifies some of the RF power that is available from its antennas to supply power. Rectification is generally realized with a simple and compact but inefficient Dickson charge pump [25]. Since there is no battery on the tag, the tag turns off soon after the reader carrier is turned off (assuming no other source of strong radiation), unlike the more complicated but more capable sensor platforms with batteries and power management (as proposed in, e.g., [26]). The ASK-based modulation from the reader varies the transmit power and thus the power available for harvesting by the tag; the tag therefore needs some shunted power supply capacitance to sustain power for up to about 10 µs during modulation.

The tag reflects power to the reader by shorting the shunted field-effect transistor (FET) at the antenna terminals with the "tx data" signal. Switching between the short and the power harvesting state enables data rates between 40 kbps and 640 kbps. Chapter 2 will demonstrate that this realizes the mixing as illustrated by Fig. 1.2. Shorting the antenna to create this modulation also shorts the charge pump and therefore the tag power supply. The buffer capacitor at the DC output sustains tag power here just as in the forward link.

The LO in both links comes exclusively from inside the reader, which must set the carrier frequency within the limitations of appropriate national RF emissions regulations. In the United States, a reader carrier frequency must be at at one of 50 channels spread evenly between 902.75 MHz and 927.25 MHz, switching ("hopping") to each one and dwelling no more than 400 ms. In most of Europe, readers may only transmit full power in one of 10 channels between 865.6 MHz and 867.6 MHz, and do not have to hop but must wait for an unused channel before transmission. These are only examples; other areas of the world have still different rules. Readers sold commercially are often able to operate in only one of these regions. In contrast, passive tags are designed for matching and backscattering across the entire 860 MHz to 960 MHz band and are therefore usable internationally.

A challenge that was mitigated in some second-generation RFID reader products was desensitization caused by a strong received carrier. Since the carrier does not convey data, it is not useful for communication. Unfortunately, some carrier leaks from the transmitter into the receiver, primarily because of imperfect antenna matching and circulator isolation in monostatic systems or by antenna-to-antenna coupling in bistatic systems. The result is that the leaked power may reasonably be over 60 dB stronger than

received modulation, so a low-noise amplifier (LNA) saturates and fails to amplify transponder signals. The receiver desensitizing signal is known in the literature as simply the carrier, leakage, or the leaking carrier.

The approach taken to solve this problem in long-range RFID readers is an adaptive feed-forward cancellation, illustrated by Fig. 1.7a. Papers that propose these systems refer to them equivalently as a **leakage canceller** [27, 28], **isolator** [29, 30], or **carrier suppression** system [31]. The ability to suppress this carrier is characterized by its tx-rx isolation (in decibels) [27, 30, 32], which may be the absolute system isolation (transmitter carrier power divided by receiver carrier power) or as relative improvement realized by the isolator. The author built a prototype in 2007 during early work on detection, pictured mounted next to bistatic antennas in Fig. 1.7b, which increased isolation by 60 dB.

Data Protocol and Capabilities

Signaling from the reader in the forward link controls the signal rate and timing of both the forward and return links, and transmits commands to the field of tags. There are only a few simple commands:

(1) "Singulation:" an inventory of all or some of the tags that respond to the reader.

(2) "Read:" retrieving data from memory on one tag.

(3) "Write:" storing data into nonvolatile tag memory of one tag.

A reader usually performs singulation before a read or write command or any change of carrier frequency to identify the tags that are available for reading or writing. For inventory purposes, singulation is the most common command and by far the slowest.

Typical tags have a 96 bit identification number. At the maximum 640 kbps data rate, we can imagine "ideal communication" (nonstop communication from one tag at a time with no symbols wasted on the protocol) could singulate tags faster than 6000 per second. In practice, well-optimized singulation with passive UHF RFID protocols are limited to a few hundred tags per second, and only in communication with a large number of tags.

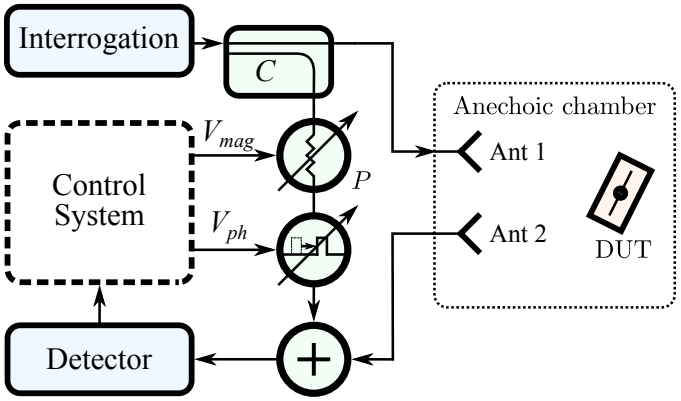

(a)

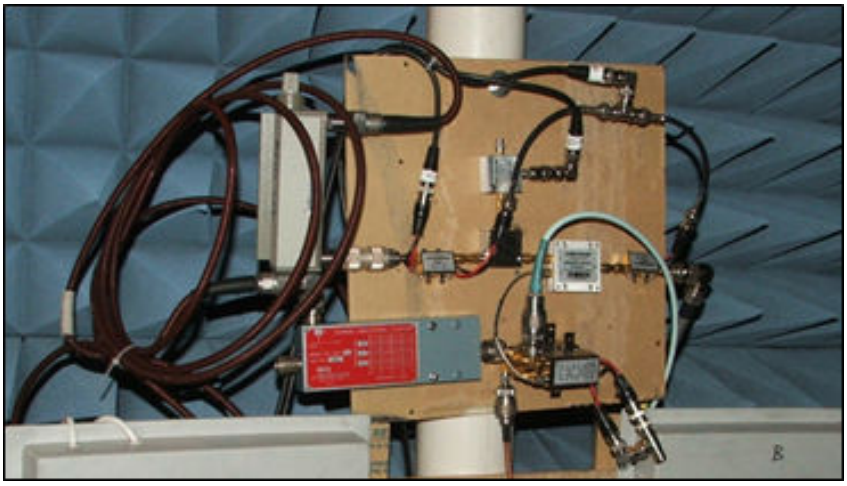

(b)

Figure 1.7: General architecture adaptive isolator (a) and a realized prototype constructed by the author in (b). A computer operates the variable attenuation and phase shift over GPIB with a DC power supply, adjusting with a steepest descent algorithm until the leaked carrier signal is minimized. The substrate is a 30 cm $\times$ 30 cm square.

The reason for the inefficiency is that tags do not generally "know" when to answer to avoid collisions (simultaneous responses), and a reader does not generally "know" which tags will respond. The solution to this in passive UHF RFID standards is known as "slotted aloha." Work since 2004 has investigated the performance of slotted aloha with additive white gaussian noise (AWGN) [33], multipath fading [34], and active interference [35]. Other authors have suggested more efficient alternative algorithms with Markov process modeling [36] or CDMA [37], but so far standards have not adopted these approaches.

1.2.4 Standards

A significant motivation behind this work was to support standards development to promote robust, reliable, and interoperable communication in U.S. federal government RFID deployments. Most of this effort is focused on test methods, which are less complete than the standards that define the communication protocol and standards.

Communication Protocol

Standards-compliant readers incorporate **anticollision**, the part of the protocol that enables the reader to select one tag out of many to respond at a time.

Test Standards

Results from tests that comply with existing standards have the advantage of implicitly conveying measurement details, giving a sense of the accuracy of the measurements and how they might help predict behavior in realistic use. If the standards give methods that achieve low measurement uncertainty, careful testing between different labs can validate conclusions by repeating the same tests in their own facilities. At present, test methods in existing standards are continuing to improve, but do not yet detail test methods necessary for complete device characterization.

Performance test standard ISO/IEC 18046-3 [38] outlines a general test for the threshold field strength necessary to activate a tag, but offers no specific approach for determining field strength. Tag scattering, which is becoming a more significant system range constraint as tags improve [39] and especially when

interference is present [40], is addressed only in protocol conformance test standards.

The 2006 version of standard ISO 18047-6 [41] prescribes a tag backscattering conformance test characterized as the difference between the radar cross section values between the tag's two load modulation states. The test method calibrates measurements of tag backscattering against the change in received power caused by adding a thin rod to the test environment. Adding and removing the entire thin rod calibration standard introduces systemic error by modulating the structural-mode scattering from the rod, which interacts with multipath in the test environment differently [39] from a tag's antenna-mode [42][43] scattering. The use of such an electrically small calibration target requires faith in the accuracy of the analysis used to compute its radar cross-section (RCS), which makes the measurement result untraceable to fundamental physical standards of any national metrology laboratory. These errors may make measurement results challenging to repeat between different testbeds, and as a result some parties may choose not to undertake the expense of running the tests. This approach can introduce significant systemic error by neglecting phase, though many existing papers have discussed how phase can be included, e.g., [42][43][44].

The 2011 version of the ISO 18047-6 conformance test standard computes "Delta RCS" for a device-under-test by inserting measurements of range and antenna gain parameters into the radar equation, incorporating measured phase. The uncertainty of results from this approach has been estimated at approximately 2 dB in a paper that used a similar approach [45]. With spectrum analyzer backscatter measurements, however, drift and automatic realignments corrupt the relative accuracy of measurements of tags taken at different times.

While calibration errors may not introduce problems in comparing tag performance, they will introduce errors in measurements of the absolute signal levels in and out of a reader. To avoid this problem, at the sacrifice of the generality offered by a "black box" tag characterization, results in this thesis are from measurements of available power transmitted into and received from the test antennas. Transmitted power is measured with a directional coupler and power sensor, and backscattered power is measured with the calibration introduced in [46].

1.3 Microwave and Communication Parameter Definitions

1.3.1 Real-valued, Analytic, and Time-Domain Voltages

The veritable cornucopia of available communication test instruments takes advantage of a wide variety of signal representations. Oscilloscopes show real-valued time domain voltage, spectrum analyzers show the power spectrum in the frequency domain, and signal analyzers give baseband signals as complex voltages in the time or frequency domains, as eye diagrams, or as constellations.

A very general tool that helps move between these is Gabor's complex analytic signal [47]. In particular, given a general excitation that includes but is not limited to a sinusoidal carrier, the analytic signal be expressed as a product of "instantaneous frequency" and the complex baseband vector.

Consider a real-valued receiver voltage, $v(t)$. The corresponding complex analytic signal (also known as complex envelope) is:

$$\mathcal{V}(t) = v(t) + j\mathscr{H}[v(t)], \tag{1.1}$$

where the imaginary part is the Hilbert transformation of $v(t)$,

$$\mathscr{H}[v(t)] = \text{p.v.} \int_{-\infty}^{+\infty} \frac{v(t-\tau)}{\pi\tau} d\tau. \tag{1.2}$$

The p.v. denotes Cauchy principal value integration. The inverse transformation from the analytic signal back to the real-valued signal is $v(t) = \text{Re}(\mathcal{V}(t))$.

The Hilbert transform defined here is not well-defined or analytically solvable for all classes of continuous signals $v(t)$. For narrowband digital signals, however, the transform has some simple key properties:

(1) Linearity: For signals $v_1(t)$ and $v_2(t)$ and real constants k_1 and k_2,

$$\mathscr{H}[k_1 v_1(t) + k_2 v_2(t)] = k_1\mathscr{H}[v_1(t)] + k_2\mathscr{H}[v_2(t)]. \tag{1.3}$$

The transformation from $v(t)$ to $\mathcal{V}(t)$ is therefore also linear.

(2) Sinusoidal transform pair [48][p. 18]:

$$\mathscr{H}[\cos(2\pi f t + \phi)] = \sin(2\pi f t + \phi), \tag{1.4}$$

for frequency and phase f and ϕ.

(3) Bedrosian's product theorem [49, 50]: For two signals $v_1(t)$ and $v_2(t)$, if $v_1(t)$ has no spectral energy above some frequency f, and $v_2(t)$ has no energy below f, then

$$\mathscr{H}[v_1(t)v_2(t)] = v_1(t)\mathscr{H}[v_2(t)]. \tag{1.5}$$

This represents is behavior of an ideal lossless and mixing process.

Combining each identity with the definition of the analytic signal makes it possible to decompose the communication signals into modulation and carrier components. In narrowband communication that uses a sinusoidal signal as a carrier (like UHF RFID), the complex signal is related to the complex-valued root mean square (RMS) baseband signal, $V(t)$, as

$$\mathcal{V}(t) = \sqrt{2}V(t)e^{2\pi f_c t}. \tag{1.6}$$

The exponential term is the sinusoidal case of the instantaneous frequency [51]. Other instantaneous frequency signals are also valid if their spectral power is exclusively at higher frequencies than $V(t)$ [49] (though certain other cases are valid as well [50]). In the RF mixing process, the instantaneous frequency represents the LO, the baseband represents the IF, and the analytic signal represents the RF (upconverted baseband) signal in the communication mixing process.

1.3.2 Fourier Transform

This thesis follows the Fourier transform defined as

$$\mathscr{F}[v](f) = \int_{-\infty}^{+\infty} v(t)e^{-j2\pi ft}dt. \tag{1.7}$$

This is the definition followed by instrument manufacturers in terms of unitary frequency rather than radial frequency [52–54], avoiding some normalizing factors. The corresponding inverse transform is

$$v(t) = \int_{-\infty}^{+\infty} \mathscr{F}[v](f)e^{j2\pi ft}df. \tag{1.8}$$

This is related to the positive half-space of the transformed analytic signal as [48, p. 9]:

$$\mathscr{F}[v](f) = \begin{cases} \frac{1}{2}\mathscr{F}[\mathcal{V}(t)](f), & f > 0 \\ \mathscr{F}[\mathcal{V}(t)](0), & f = 0 \\ \frac{1}{2}\mathscr{F}[\mathcal{V}(t)](-f) & f < 0. \end{cases} \tag{1.9}$$

Spectrum analyzers often show power spectral density (PSD) defined only in the positive half-space of the frequency domain. This includes power from negative frequency components "folded" onto the positive half space. The PSD of a signal absorbed into a load with impedance Z, with units of power per frequency, is

$$\begin{aligned} \text{PSD}[v(t)](f) &= 2\frac{|\mathscr{F}[v(t)](f)|^2}{\text{Re}(Z)} \\ &= \frac{|\mathscr{F}[V(t)](f - f_c)|^2}{\text{Re}(Z)}. \end{aligned} \tag{1.10}$$

This is the "ideal" continuous PSD, with the factor of 2 discrepancy arising from the RMS definition of the complex baseband signal $V(t)$. The actual PSD trace displayed on an instrument will be altered by discritization, compression, uneven frequency response, spurious harmonics, impedance mismatch, and windowing. It is defined for $f \geq 0$ and normalized to the real part of the instrument port impedance, $\text{Re}(Z)$.

1.3.3 Pseudowave Scattering Parameters

Network analysis in this thesis primarily employs "pseudowave" S-parameters. These parameters are considered in great detail in [55]. They describe steady-state behavior of waves traveling between microwave networks relative to some reference impedance, Z_0. They are equivalent to "traveling-wave" S-parameters [56] only in transmission lines with characteristic impedance equal to Z_0. Dependence on frequency in this thesis is implicit, and not shown for power or network parameters.

Each Z_0 will be assumed real and identical at all ports for this work, to simplify expressions of power. The incident and scattered pseudowaves at port m are

$$a_m = e^{-j\phi_0}\frac{V_m + I_m Z_0}{2\sqrt{Z_0}} \text{ (incident wave)}, \tag{1.11}$$

and

$$b_m = e^{-j\phi_0} \frac{V_m - I_m Z_0}{2\sqrt{Z_0}} \text{ (scattered wave).} \tag{1.12}$$

V_m and I_m are time-harmonic voltage and current phasors with defined with RMS magnitudes. These are waves at the single radial frequency $\omega = 2\pi f$. The normalization to $2\sqrt{Z_0}$ allows unit a_m or b_m to correspond with unit power as $|a_m|^2$ and $|b_m|^2$. The phase rotation ϕ_0 shared by a and b denotes normalization to an arbitrary zero phase reference.

In these terms, each pseudowave scattering parameter between two ports n and m is

$$S_{mn} = \frac{a_m}{b_n}. \tag{1.13}$$

The S_{mn} elements of an $M \times N$-port network form an $M \times N$ matrix $[S]$.

When all ports are terminated in Z_0, S_{mn} are related to incident and scattered power by

$$\frac{\text{Scattered power to } Z_0 \text{ load, port } m}{\text{Incident power from a } Z_0 \text{ source, port } n} = |S_{mn}|^2 \tag{1.14}$$

The convention in this text is to refer to reflection coefficients of *loaded* $[S]$ as ρ with subscripts, and transmission coefficients of loaded $[S]$ as τ with subscripts. In this case, each port's load needs to be specified except m (and n for τ), which are still referenced to Z_0.

The relationship between ρ and a port input impedance, Z, is

$$\rho = \frac{Z - Z_0}{Z + Z_0} \tag{1.15}$$

(with all other ports are terminated in Z_0). The ρ looking into port m of a multiport network is the same as a scattering matrix element S_{mm} only if all ports are terminated in impedance Z_0. Detailed analysis for finding loaded Z and ρ are given in many network theory texts like [56].

1.3.4 Power Wave Parameters

An alternative to pseudowave scattering parameters are power waves [57]. These are compared extensively in [55]. They are popular in RFID literature, and in use by some nonlinear circuit simulation software like AWR Microwave Office. In some cases they are ambiguously referred to as "reflection

coefficients" or "transmission coefficients," which may cause confusion with pseudowave reflection coefficients.

In this network parameter system, each port m is terminated by a physical load, Z_m, not the arbitrary reference Z_0. Incident and scattered pseudowaves at port m are [57]

$$\tilde{a}_m = e^{-j\phi_0} \frac{V_m + I_m Z_m}{2\sqrt{\text{Re}\, Z_m}} \text{ (incident wave)}, \tag{1.16}$$

and

$$\tilde{b}_m = e^{-j\phi_0} \frac{V_m - I_m Z_m^*}{2\sqrt{\text{Re}\, Z_m}} \text{ (scattered wave)}. \tag{1.17}$$

Like all other phasors in this thesis, V_m and I_m have RMS magnitudes. An $M \times N$ power scattering matrix $[\tilde{S}]$ and each element $\tilde{S}_{mn}$ (composed of $\tilde{a}_m$ or $\tilde{b}_n$) are defined much like $[S]$.

These parameters describe interaction between a network and its load, unlike pseudowaves, which characterize the network when loaded with some Z_0 that can be chosen arbitrarily. The power wave reflection coefficient $\tilde{S}_{mm}$ is related to available reflected power from port m terminated in Z by

$$\frac{\text{Reflected power absorbed by generator}}{\text{Available incident power}} = |\tilde{S}_{mm}|^2 = \left|\frac{\tilde{a}_m}{\tilde{b}_m}\right|^2 = \left|\frac{Z - Z_m^*}{Z + Z_m}\right|^2. \tag{1.18}$$

The result is a compact representation of reflected and transmitted power in simple one-ports. Power delivered into port m is

$$\frac{\text{Power delivered to port } m}{\text{Available incident power}} = 1 - |\tilde{S}_{mm}|^2. \tag{1.19}$$

The compactness of power absorption expressions with power waves belies underlying complexity in their use. Changing any Z_m at a non-isolated port of $[\tilde{S}]$ causes the power normalization of each $\tilde{a}_m$ and $\tilde{b}_m$ to change as well. The wave parameters in (1.16) and (1.17) depend on both Z_m and Z_m^*; this means that a graphical representation needs an extra dimension to represent $\angle Z_m$, in addition to the two on a Smith chart. There is no "3D Smith chart" of this type in broad use [58] (the extra dimension in [59] is to support $|\rho| > 1$). There are also no instruments that directly measure power waves, so they have to be computed indirectly from pseudowave measurements with a network analyzer. This complicates measurement uncertainty estimation, which is understood and expressed primarily in terms of pseudowaves [60, 61].

These challenges are surmountable and for some uses may be outweighed by the convenience of equations (1.18) and (1.19). In this work, we mainly use power waves to convey conceptual problems compactly, but also give expressions in terms of more measurable pseudowaves. This lets us leverage mature test engineering and metrology and use well-trodden S-parameter network analysis.

1.3.5 Time-Harmonic Linear Power Absorption and Mismatch

The subject of power normalization with respect to voltages and currents can become thorny and generally unpleasant when waves are involved. Other authors already discuss this in great detail (see for example [62, pp. 77-79]). Combining too many normalization conventions could complicate notation and distract from the main ideas of this thesis. Some effort is made here, therefore, to define signal quantities clearly, so physical meaning is clear, and theory and simulation and measurement results can all be compared directly.

This thesis defines voltages solely at the interface between networks, as illustrated in the phasor domain Fig. 1.8(a,b), *never* as Thevenin equivalent circuits like Fig. 1.8(c). These circuits are truly equivalent only in the sense that they excite in the same voltages and currents as in the actual source. They are *nonphysical*, however, in the sense that an RF generator is never actually realized as a zero-impedance voltage source in series with a lossy resistor. Their impedances behave as a voltage divider, reducing the voltage V presented across Z_L compared to the Thevenin voltage, according to Fig. 1.8(c).

Voltage and current phasors and baseband signals are defined as RMS to match the convention of instrument manufacturers — this *is* a metrology-focused thesis, after all. This has the side-effect of simplifying normalizing constants: power delivered into Z_L is simply

$$\text{Power delivered into } Z = \text{Re}(V_{rms} I_{rms}^*) = \frac{|V_{rms}|^2}{\text{Re } Z}. \tag{1.20}$$

The relationship between this "available power," the power available to a Z_0 load (by pseudowaves with magnitudes $|b|$ or $|a|$), and the power actually delivered into a load depends on the generator and load impedances. Assume that our generator and load of Fig. 1.8 have reflection coefficients ρ_G and ρ_L. The power wave reflection coefficient between this feed and generator is $\tilde{\rho}$.

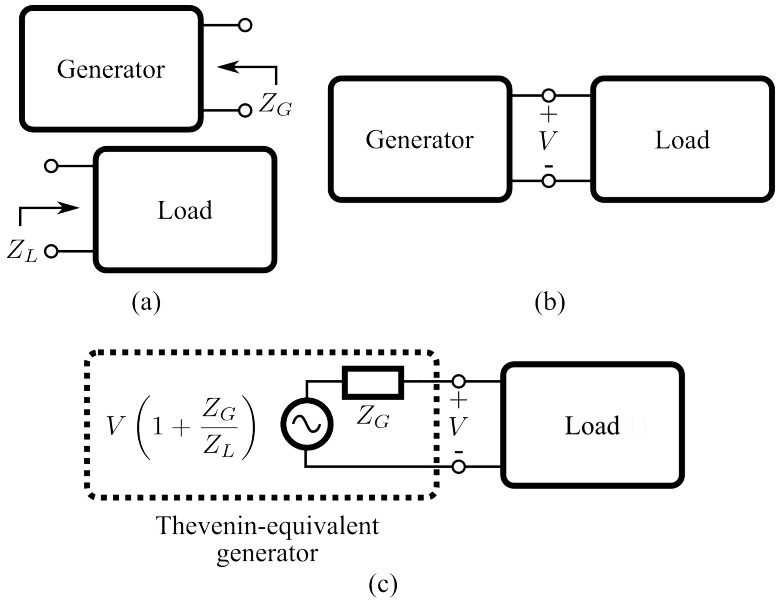

Figure 1.8: In this thesis, for (a) arbitrary generator and load, voltages V are defined at (b) the interface between them. This is different from (c) Thevenin-equivalent source voltage.

The "conjugate match efficiency" is defined as [56]:

$$\frac{\text{Power delivered into } Z_L}{\text{Power delivered if } Z_L = Z_G^*} = \frac{(1-|\rho_L|^2)(1-|\rho_G|^2)}{|1-\rho_L\rho_G|^2}, = \frac{4\text{Re}(Z_L)\text{Re}(Z_G)}{|Z_L+Z_G|^2} = 1-|\tilde{\rho}|^2. \quad (1.21)$$

This is between 0 (no power delivered) and 1 (the conjugate match case).

The "Z_0 match efficiency" is:

$$\frac{\text{Power delivered into } Z_L}{\text{Power delivered if } Z_L = Z_0} == \frac{1-|\rho_L|^2}{|1-\rho_L\rho_G|^2}. \quad (1.22)$$

Despite the name, this can be larger than 1 when $|1-\rho_L\rho_G| < 1$.

This lets us define when we might be able to assume the source and receiver transfer all available power. A tight definition of "well-matched" for this thesis is 20 dB of return loss at both the receiver and where it is connected; this corresponds to match efficiency greater than 96%, or less than 0.2 dB of mismatch loss. This is in many cases reasonable.

The convention in this work is that variables labeled P with subscripts mean "available power to a conjugate-matched load." The sole exceptions are P_L and P_{bs}, power delivered into the tag chip and backscattered power delivered into the reader receiver.

1.4 Measurement Uncertainty

Measurement uncertainty is the quantitative complement of measurement accuracy. It is qualitatively equivalent to say a measurement has "small uncertainty" as to say it is "very accurate." Unlike accuracy, however, there is a more defined (though not rigorous) quantitative practice underpinning the calculation and expression of measurement uncertainty. This section offers a brief overview of the concept of uncertainty as a basis for its use in the remainder of the thesis.

The practice of estimating and expressing measurement uncertainty is described for international purposes by the Bureau International des Poids et Mesures (BIPM) guide on uncertainty of measurement ("GUM") [63], and within National Institute of Standards and Technology (NIST) (where much of the work for this thesis was performed) by Technical Note 1297 [64]. Uncertainty statements performed in this thesis are computed and expressed according to the processes described in these documents as carefully as possible.

We expect that there is in general more than one kind of error contributing to the total uncertainty of a physical measurement. Each source of error could be systematic (deterministic and predictable), or random (non-deterministic or stochastic). A systematic error that can be identified and modeled can often be removed analytically from the measurement result. If the measurement involves independent samples of a zero-mean random error, averaging can mitigate its effect on measurement uncertainty. Repeatability (or precision) is the complement of these random components of uncertainty: the extent to which a measurement gives the same result when repeated many times.

Classifying a source of error as systematic or random depends in part on whether it is measured as part of the experiment. In microwave network measurements, for example, mismatch can alter the power absorbed by a power sensor. If the circuit is invariant with time, the mismatch effects might characterized with a network analyzer to be de-embedded from the final measurement result, removing it as a source of error. On the other hand, if the network is a pair of antennas in an anechoic chamber, multiple reflections between the antennas change as a function of the distance between them; sweeping antenna position thus results in hard-to-predict error in measured power that can be assumed random.

Consider a measurement result represented by a random variable Y. The measurement process is modeled by some function $f(X_1, X_2, ..., X_n)$, which ideally incorporates all n different sources of variability or error. Each source of error has a standard deviation which we call the **standard uncertainty** $u_i = u(x_i)$. If these errors are uncorrelated, the **combined uncertainty** of the measurement result y, $u_c(y)$, is computed as

$$u_c(y) = \sqrt{\sum_{i=1}^{n} \left(\frac{\delta f}{\delta x_i} u(x_i) \right)^2}. \tag{1.23}$$

This is the law of propagation of uncertainty simplified for uncorrelated X_i. Each sum term is the sensitivity of the of x_i and the variance of X_i.

Approaches to estimating each $u(x_i)$ are classified into two types. Statistical approaches are known as "type A;" these are based more on analysis of the data than on physical models for the error terms. This could be as simple as measuring the standard deviation of a data series. "Type B" estimates of $u(x_i)$ come from an assumed probability distribution for X_i. Type B is often very practical in microwave measurement: the thermal noise of a voltage signal is accurately described by the normal distribution,

mismatch error is accurately described by the U-shape distribution [65][66], and digitized rounding error is uniformly distributed. Thus, estimates of uncertainty in this work are generally "type B." Uncertainty estimation is so rough in part, however, because types "A" and "B" are both accepted approaches but may give different $u(x_i)$.

Despite the firm-sounding name, the "law" of propagation of uncertainty is a first-order Taylor series approximation that is only accurate if either:

(1) the errors X_i with the largest $u(x_i)$ are normally distributed; or,

(2) there are a large number of X_i with similar $u(x_i)$,

by the central limit theorem. When one of these conditions is assumed valid for a meaningful $u_c(y)$, Y can be assumed distributed normally. In this case, $u_c(y)$ is the standard deviation of Y, so we have only 68% confidence that the measurement is within $\pm u_c(y)$ of the "correct" value. Scaling $u_c(y)$ by a coverage factor $k > 1$ gives the **expanded uncertainty** of our measurement, U:

$$U = k u_c(y), \ (U \geq 0). \tag{1.24}$$

The value $k = 2$ is a common implicit choice in microwave measurements, corresponding to about 95% confidence that the "true" value of the measurement y lies in interval $[y - U, y + U]$, if combined error is normally distributed. Some older papers use $k = 3$ that suggests 99.7% confidence that y lies in the same interval (at the expense of larger reported U). This thesis uses $k = 2$.

Microwave measurements are often given as ratioed unitless quantities on a logarithmic scale as decibels. The **relative expanded uncertainty** is simply

$$U_r = \frac{U}{|y|}, \tag{1.25}$$

depending on the same coverage factor as U. When $k = 2$, U_r describes the probability that y of an ideal measurement of y normalized to the actual measurement of y is

$$\left| \frac{y - U}{y} \right| < \left| \frac{\text{Ideal } y}{y} \right| < \left| \frac{y + U}{y} \right| \tag{1.26}$$

or

$$|1 - U_r| < \left| \frac{\text{Ideal } y}{y} \right| < |1 + U_r| \,. \tag{1.27}$$

with about 95% confidence. When y is a power quantity, we can also convert to decibels,

$$10\log_{10}|1-U_r| < 10\log_{10}|\text{Ideal } y| - 10\log_{10}|y| < 10\log_{10}|1+U_r|\,. \tag{1.28}$$

For small errors, these bounds can be expressed as

$$-U_{dB} < |\text{Ideal } y|\,(\text{dB}) - |y|\,(\text{dB}) < +U_{dB}\ (\text{approximate}). \tag{1.29}$$

When $U_r < 0.25$ ($U_{dB} < 1$ dB), this approximation is valid and $U_{dB} \approx 4U_r$ to within 0.03 dB. The magnitude of measurement errors in this work is often small, so uncertainty estimates for measurements in dB are computed according to (1.29). On the order of $U_r > .2$, the absolute value of the two bounds are no longer approximately equal, and the supplied approximation for U_{dB} increases in error.

As a final note on uncertainty, a side-effect of the large numbers of assumptions in uncertainty estimation is that U is a subjective result. An estimate combined with large n is likely to need so many assumptions that they are difficult to list. The practice used in this document is to assume the largest (worst) reasonable value for each $u(x_i)$ to give conservative $u_c(y)$ and thus U.

1.5 Thesis Scope and Structure

The theoretical focus in this work is communication with binary-modulated passive backscattering transponders. This class of devices currently includes RFID, but in the near future the cost benefits to passive backscatter may see its use in other common applications like wireless sensing.

Practical application of the theory is to passive RFID tags with fixed readers following EPC Global Class 1 Generation 2 or ISO 18000-6C standards (which are considered identical, and synonymous with "passive UHF RFID" for the purposes of this thesis). This class of system is of interest for the following reasons:

- Most commercial RFID systems operating in the far field follow these standards.
- Many readers and tags from different vendors are marketed as compliant with these standards. This creates uncertainty about interoperability and performance when readers and tags from different vendors must be used together, which may benefit from improved test practices.

- Fixed readers operate unsupervised during normal use, so there is no human operator to work around reliability problems. More extensive tests and modeling are therefore necessary to ensure robust operation, but there is little relevant literature on this subject.

- A key feature of fixed readers is long range. At long range, backscattered tag response power is weak, which can strain link range and reliability. This imposes fundamental limitations on these communications that have not studied in detail.

- A fixed reader is usually more costly than a mobile reader. Improved understanding of the limitations of these fixed-reader systems may therefore have the greatest influence on end-user costs and benefits, compared to systems that use mobile readers.

Within this type of system, the goal is to predict backscatter signal levels into a reader. When the noise level inside the receiver is fixed, this corresponds to predicting signal-to-noise ratio (SNR) (in low-interference environments) or signal-to-interference ratio (SIR) (in higher-interference environments) relative to the tag backscatter. These data, in turn, predict reliability of tag communication and detection rate when interference is weak. This work approaches this problem with microwave network theory, to maximize the generality of the solution with arbitrary network blocks representing environmental loss effects.

The contributions of the remaining chapters toward these goals are organized as follows:

Chapter 2 discusses the most basic link parameter of backscatter modulation, signal power. It is not explicitly derived in terms of measurable signals by standards or other technical technical literature. This chapter investigates advantages and disadvantages to defining the modulation power as "classic" digital ASK or BPSK modulation schemes, and how they can be separated from the large leaked carrier. Passive UHF RFID encoding makes BPSK independent of the carrier, which simplifies spectral analysis and ensures that energy is conserved at all reference points for any passive tag modulation loads.

Chapter 3 presents models and characterizations of passive backscatter link power. High-level analysis of the benefits and risks in the use of RFID requires an understanding of what is possible within the bounds of physics, standards, and emission regulations. Fundamental power parameters and relationships defined in Chapter 2 enable informed discussion of device characterization and system behavior in

free space, and recent movement toward more general analysis based on network theory. This chapter formulates an alternative, more compact tag backscattering characterization than radar cross-section that applies in passive systems. With this metric, system designers can find a deterministic minimum bound to backscatter received from any passive tag under realistic fading conditions with a trivial computation.

Chapter 4 defines test methods for measuring backscatter power with calibration circuits. The devices and test methods generate reference signals suitable for transceiver or transponder performance tests. For transponders, approaches are investigated both 1) through fixed-loss coaxial networks and 2) over-the-air through antennas. For reader testing, a coaxial calibration device reflects adjustable modulation power into monostatic reader ports. The testbed is overspecified to result in lower uncertainty than required for realistic commercial device tests in order to rigorously validate the model.

Chapter 5 discusses use of the power measurements in testing transponder backscatter performance. This chapter compares the accuracy of radar cross section and backscatter figure of merit measurements, and propagation to estimates of received backscatter power. The received power estimate is always at least slightly greater than the uncertainty of the tag backscatter metric used to estimate it. Uncertainties for radar cross section measurements contribute negligibly to uncertainties in received power, as long as multipath is weak. In contrast, uncertainty of a minimum backscatter power bound estimate is the same as figure of merit measurement uncertainty. Thus, estimates of minimum backscatter power from the figure of merit are always more accurate than estimates of backscattered power from σ_{Δ}.

Chapter 6 gives techniques for reliable system design based on the device tests. With validated theory and measurement ability, we can now analyze system behavior of off-the-shelf commercial readers and tags. Use of the minimum backscattered tag power bound predicted in Chapter 3, coupled with information about the sensitivity and interference rejection of the reader, allows system designers to determine whether channel diversity schemes are necessary. Calibrated measurements of 20 different commercial tags suggest long-term trends of increasing communication range but lower inventory rate between fixed readers and passive tags. Finally, the application to RFID culminates with a system design approach for ensuring reliable backscatter communication.

Chapter 7 concludes the thesis with a brief summary, directions for future work, and extolls the

author's peer-reviewed publications.

Finally, Appendix I provides a table of link variables as a reference for the preceding chapters.

Chapter 2

Backscattered Receiver Signals and Power

> Professor Benson: "Young fellow, you and the others have to see and hear before you can know. I have one advantage over all of you: *calculus!*"
>
> "Il Pianeta degli Uomini Spenti" (1961)

Communication by backscatter is less broadly understood in the technical community than by powered transmission. This no surprise, since its use is rare. A side effect, however, is that basic signal and power definitions remain vague and undefined in standards, so there is no widely-accepted guidance or reference on the meaning of common parameters.

In backscatter literature, for example, the terms ASK and BPSK are typically implicitly assumed to refer to a digital signal constellation made of the two power wave states that realize load modulation [67, 68]. Current RFID standards [1, 2] explicitly allow tags to respond with either ASK or BPSK but define neither. The modulation signal received by a interrogator can also be defined many different ways which have not been discussed explicitly in the literature. Prior art has assumed at least three different normalizations without justification. The result is that Green and Nikitin [69, 70] compute "backscattered power" as twice that of Skali (and derived standards) [41, 44], which itself gives twice

the result of Karthaus and the author of this thesis [68, 71]. Without guidance from a standard blessing one of these, the same quantity could conceivably differ by a factor of up to 4 (6 dB) among different sources.

This chapter investigates the validity and spectral properties of various definitions of power given the requirement of power conservation at network interfaces. The basis is a model of backscatter modulation through microwave networks built with basic signal and network theory. The resulting contribution of this chapter is an explicit and carefully justified definition for modulation power in terms of receiver baseband signals. This definition then becomes the basis for discussion of backscattered power in later chapters. This type of analysis is necessary in the broader technical community to inform any future official decision about defining signal parameters.

2.1 Binary Load-Modulation States through Microwave Networks

A network model of a switched impedance loading a microwave network is illustrated in Fig. 2.1, following the topologies of [43] and [46]. This could be viewed as a complete passive RFID system model without loading by the interrogator (or with a Z_0-matched interrogator). The network parameters (besides impedances Z_L) are pseudowave S-parameters as defined in Section 1.3.3.

The three-port pseudowave network E represents the general case of any transmission effects between a transceiver and the load modulation. The transceiver could be bistatic by separate transmission and detection at ports 1 and 2, or monostatic by transmitting and detecting at either port 1 or port 2 and loading the other with Z_0. Port 3 is the interface between the tag's chip and antenna. The interrogator transmits into port 1 or 2. The transmission effects in E could include (but are not limited to) wireless propagation, test circuits, antennas, or transmission lines.

If the two networks are disconnected (Fig. 2.1a), transmission coefficients between the loaded ports in the reciprocal transmission are $E_{23} = E_{32} = b_3/a_2$ and $E_{31} = E_{13} = b'_3/a'_1$ (the notation for pseudowaves b' and a' indicates port 3 of E is not attached to Z_L). The reflection coefficients of the backscattering antenna and the modulator are $E_{33} = b'_3/a'_3$ and $\rho_L = b_L/a_L$, respectively. E and ρ_L are measurable by network analyzer if the modulator and transmission networks E can be disconnected

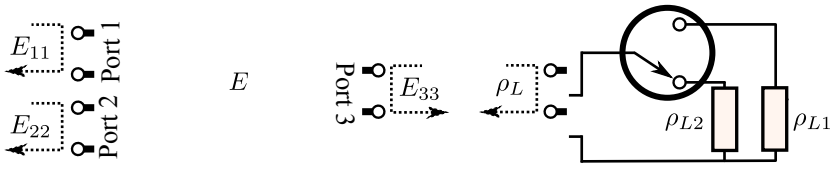

(a) disconnected

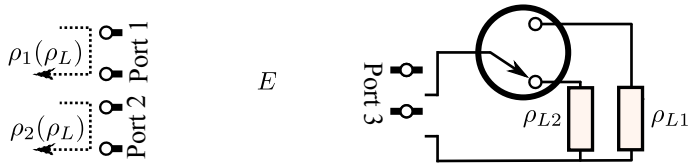

(b) connected in monostatic operation

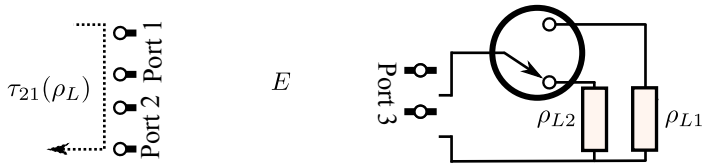

(c) connected in bistatic operation

Figure 2.1: Reflection and transmission coefficients presented to a Z_0-matched interrogator (a) disconnected from and (b,c) loading the 3-port pseudowave network $[E]$ in monostatic and bistatic. The modulator switches between $\rho_L \rightarrow \{\rho_{L1}, \rho_{L2}\}$ (impedances $Z_L \rightarrow \{Z_{L1}, Z_{L2}\}$).

into well-defined networks.

If the two networks are connected (Fig. 2.1b), ports 1 and 2 of E present loaded reflection coefficients ρ_1 and ρ_2 for monostatic detection. Bistatic detection into a Z_0-matched transceiver is characterized loaded transmission coefficients τ_{21} (excited at port 1) or τ_{12} (excited at port 2).

2.1.1 Bistatic Operation

Consider bistatic operation excited at port 1 of E as in Fig. 2.1c and detected at port 2. The transmission coefficient representing this process depends on the modulator load, $\tau_{21} \rightarrow \tau_{21}(\rho_L)$. An expression for $\tau_{21}(\rho_L)$ in terms of E, some arbitrary modulation load ρ_L, and the incident pseudowave is [56, p. 108]:

$$\tau_{21}(\rho_L) = E_{21} + E_{31}E_{23}\frac{\rho_L}{1 - E_{33}\rho_L}, \tag{2.1}$$

assuming that port 2 is isolated from port 1 or nontransmitting. Equivalently, τ_{21} can be defined in terms of transmission at port 2 and reception at port 1 by reversing subscripts 1 and 2.

Consider the two different load states, $\rho_L \rightarrow \{\rho_{L1}, \rho_{L2}\}$. Through dependence on ρ_L, $\tau_{21}(\rho_L)$ also takes two states. The change in the transmission coefficient presented between ports 1 and 2 is

$$\Delta\tau_{21} = \tau_{21}(\rho_{L2}) - \tau_{21}(\rho_{L1}) = \frac{E_{31}E_{23}}{(1 - E_{33}\rho_{L2})(1 - E_{33}\rho_{L1})}(\rho_{L2} - \rho_{L1}). \tag{2.2}$$

The average between the two states is $\overline{\tau}$:

$$\begin{aligned} \overline{\tau}_{21} &= \frac{\tau_{21}(\rho_{L2}) + \tau_{21}(\rho_{L1})}{2} \\ &= E_{21} + \frac{E_{31}E_{23}}{(1 - E_{33}\rho_{L2})(1 - E_{33}\rho_{L1})}(E_{33}\rho_{L2}\rho_{L1} + \frac{\rho_{L2} + \rho_{L1}}{2}). \end{aligned} \tag{2.3}$$

The change and mean of the transmission coefficient are related to $\tau_{21}(\rho_{L2})$ and $\tau_{21}(\rho_{L1})$ as,

$$\begin{aligned} \tau_{21}(\rho_{L1}) &= \overline{\tau}_{21} + \frac{1}{2}\Delta\tau_{21} \\ \tau_{21}(\rho_{L2}) &= \overline{\tau}_{21} - \frac{1}{2}\Delta\tau_{21}. \end{aligned} \tag{2.4}$$

The two states are thus centered at $\overline{\tau}_{21}$ on the complex plane and offset by $\pm\Delta\tau_{21}/2$.

2.1.2 Monostatic Operation

The monostatic equivalent of (2.2) at port 1 for the loaded reflection coefficient, $\rho_1(\rho_L)$, is [72]

$$\rho_1(\rho_L) = E_{11} + E_{31}E_{13}\frac{\rho_L}{1 - E_{33}\rho_L}. \tag{2.5}$$

The change in reflection coefficient between these states is

$$\Delta\rho_1 = \rho_1(\rho_{L2}) - \rho_1(\rho_{L1}) = \frac{E_{31}E_{13}}{(1 - E_{33}\rho_{L2})(1 - E_{33}\rho_{L1})}(\rho_{L2} - \rho_{L1}). \tag{2.6}$$

The change of subscripts and variables from (2.3) gives the average between the states as

$$\begin{aligned}\overline{\rho}_1 &= \frac{\rho_1(\rho_{L2}) + \rho_1(\rho_{L1})}{2} \\ &= E_{11} + \frac{E_{31}E_{13}}{(1 - E_{33}\rho_{L2})(1 - E_{33}\rho_{L1})}(\frac{1}{2}E_{33}\rho_{L2}\rho_{L1} + \frac{\rho_{L2} + \rho_{L1}}{2}).\end{aligned} \tag{2.7}$$

The mean and difference also decompose into $\rho_1(\rho_{L2})$ and $\rho_1(\rho_{L1})$ like τ_{21}:

$$\begin{aligned}\rho_1(\rho_{L1}) &= \overline{\rho}_1 + \frac{1}{2}\Delta\rho_1 \\ \rho_1(\rho_{L2}) &= \overline{\rho}_1 - \frac{1}{2}\Delta\rho_1.\end{aligned} \tag{2.8}$$

The states are thus centered at $\overline{\rho}_1$ on the complex plane and offset by $\pm\Delta\rho_1/2$.

Observe that the only difference between this monostatic derivation and the bistatic derivation is that subscripts that refer to port 2 have been renumbered to 1.

2.2 Backscatter as a Receiver Signal

2.2.1 Signal Anatomy

Consider an ideal and Z_0-matched transceiver. We showed in the previous section that the expressions for $\rho_{1,2}$ and $\tau_{21,12}$ take the same form and differ only in subscript indexing. If the Z_0-matched transceiver transmits a wave into either port 1 or 2, the corresponding port has a voltage phasor of $V_{tx}/\sqrt{Z_0}$ by (1.11) across its terminals. The receiver in the ideal transceiver outputs the complex baseband voltage, V, related to the scattered pseudowave $b/\sqrt{Z_0}$ exactly by (1.12), at either port 1 or 2. Thus, (2.5) and (2.1) relates V and V_{tx} with ρ_L and E:

$$\begin{aligned}V(\rho_L) &= V_{tx}E_{11} + V_{tx}E_{31}E_{13}\left(\frac{\rho_L}{1 - E_{33}\rho_L}\right) \text{ (monostatic)} \\ V(\rho_L) &= V_{tx}E_{21} + V_{tx}E_{31}E_{23}\left(\frac{\rho_L}{1 - E_{33}\rho_L}\right) \text{ (bistatic),}\end{aligned} \tag{2.9}$$

Each discrete ρ_L state therefore corresponds with a steady-state received voltage phasor, V. Note that $V(\rho_L)$ is the steady-state voltage; physical time-varying $V(t)$ include transient effects from the propaga-

tion environment, finite switching time in Z_L, and frequency-dependent circuit mismatch effects. Like $\rho_{1,2}$ and $\tau_{21,12}$, binary states of V can be expressed as a mean and a difference $\overline{V}$ and ΔV.

The terms $V_{tx}E_{11}$ and $V_{tx}E_{21}$ are invariant with ρ_L, and in our ideal receiver contribute only to $\overline{V}$ and not ΔV. In physical circuits, the invariant term is often much larger than the term on the right. This term therefore usually dominates $\overline{V}$.

The more complicated terms on the right of (2.9) determines ΔV, but in general also contributes to $\overline{V}$. The magnitude of the backscattered signal ΔV is proportional to the magnitudes $|E_{31,13}|$ and $|E_{32,23}|$. The ΔV has a phase that also depends E and ρ_L, but that is not important for communication (more so for tag position estimation [73]).

Thus, we expect that a received signal will change with ρ_L, but also contain constant independent components that may be much larger than the component associated with ρ_L.

2.2.2 Receiver Signals in the Time Domain

Let the load vary with time, $\rho_L \rightarrow \rho_L(t)$, producing time-varying received signal $V \rightarrow V(t)$. The time-varying baseband has a modulation component $V_{bs}(t)$ and interfering constant component V_{leak}, so

$$V(t) = V_{leak} + V_{bs}(t) \text{ (monostatic or bistatic).} \tag{2.10}$$

The analytic signal corresponding to the modulation, $\mathcal{V}_{bs}(t)$, is

$$\mathcal{V}_{bs} = \sqrt{2}V_{bs}(t)e^{j2\pi f_c t}, \tag{2.11}$$

recalling that baseband voltage phasors in this thesis are defined as RMS.

The analytic signal corresponding to the scattered wave into the matched receiver is therefore

$$\begin{aligned} \mathcal{V} &= \mathcal{V}_{leak}(t) + \mathcal{V}_{bs}(t) \\ &= \sqrt{2}e^{j2\pi f_c t}(V_{leak} + V_{bs}(t)). \end{aligned} \tag{2.12}$$

The real-valued time domain voltage at the receiver, $v(t)$, is related to the analytic signal as

$$v(t) = \text{Re}(\mathcal{V}) = \sqrt{2}\left(|V_{leak}|\cos\left(2\pi f_c t + \angle V_{leak}\right) + |V_{bs}(t)|\cos\left(2\pi f_c t + \angle V_{bs}(t)\right)\right). \tag{2.13}$$

This is the signal that would appear on an ideal Z_0-matched oscilloscope measurement trace.

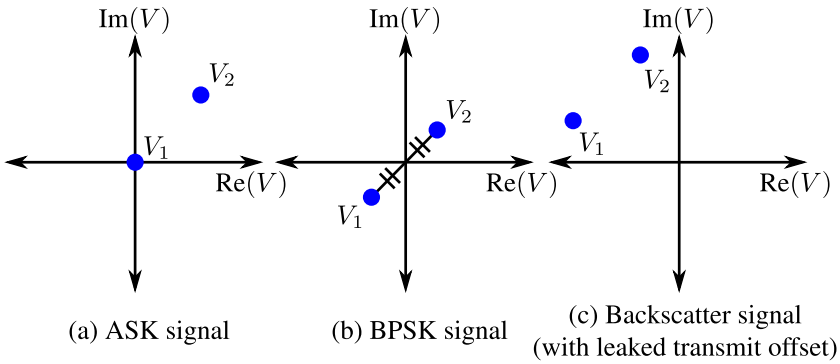

(a) ASK signal (b) BPSK signal (c) Backscatter signal (with leaked transmit offset)

Figure 2.2: Examples of digital modulation constellation diagrams, comparing ideal (a) amplitude-shift keying and (b) biphase-shift keying against (c) signals received at a interrogator with realistic leaked components.

2.2.3 Signal Decomposition

A fundamental problem in defining modulation power is separating V into the self-interfering leakage component, V_{leak}, and a backscatter modulation component, $V_{bs}(t)$. Consider first the two basic types of binary digitally-modulated symbol keying, ASK and BPSK. Their signal constellations [74] are illustrated on Fig. 2.2(a,b). The points V_1 and V_2 represent the two baseband states on the complex plane. In contrast, a more realistic constellation V for our received backscatter signal illustrated in Fig. 2.2(c). As illustrated, pure ASK requires $V_1 = 0$ or $V_2 = 0$, and BPSK requires $|V_1| = |V_2|$, so $V(t)$ is neither ASK nor BPSK.

Instead, we can define V_{leak} so that the remaining signal component is purely ASK or BPSK. This is illustrated in Fig. 2.3.

The "offset ASK" decomposition is shown in Fig. 2.3(a). Let the "leaked" offset state be defined as $V_{leak} = V_2$. This makes the decomposition appear as

$$\begin{aligned} V_{leak} \text{ (ASK case)} &= V_2 \\ V_{bs} \text{ states (ASK case)} &= \{0, V_1 - V_2\} = \{0, \Delta V\}. \end{aligned} \tag{2.14}$$

The V_2 and ΔV here characterize the carrier and modulation amplitudes of the V constellation, respectively.

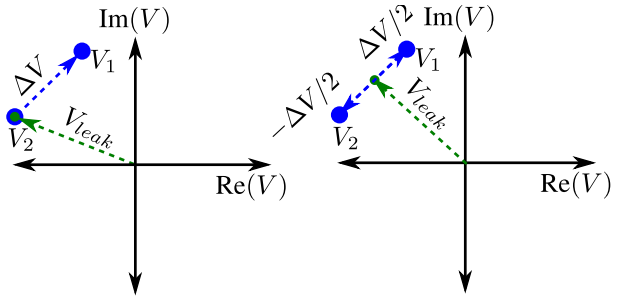

(a) ASK + leaked offset (b) BPSK + leaked offset

Figure 2.3: A digitally modulated baseband backscatter signal can be decomposed into $V(t) = V_{bs}(t) + V_{leak}$ as (a) offset ASK or (b) offset PSK.

Next, consider the "offset BPSK" definition as in Fig. 2.3(b).

$$\begin{aligned} V_{leak} \text{ (BPSK case)} &= \frac{1}{2}(V_2 + V_1) = \overline{V} \\ V_{bs} \text{ states (BPSK case)} &= \pm\frac{1}{2}(V_2 - V_1) = \pm\frac{1}{2}\Delta V. \end{aligned} \tag{2.15}$$

This is an even-odd decomposition of V. This time, $\overline{V}$ and $\Delta V/2$ are the carrier and modulation component amplitudes.

So far, defining received binary modulation encoding as either ASK or BPSK is legitimate for arbitrary ρ_{L1} and ρ_{L2}. The choice of definition determines both $V_{bs}(t)$ and V_{leak}, so the power contained in each component depends on this definition of received modulation encoding. Statements of digitally-modulated backscatter power therefore need either an implicit (for example, by use of standards) or explicit statement associating the power quantity with one of these definitions.

2.2.4 Frequency-Modulated Encoding in Passive UHF RFID

Defining V_{leak} and V_{bs} in terms of baseband modulation states in the time domain is convenient for describing RFID-specific communication. Currently, standards electronic product code (EPC) class 1 generation 2 (C1G2) and ISO 18000-6C agree on the same frequency modulation scheme for interrogator-to-tag communication. The "bi-phase space" symbol encoding defined by these standards is illustrated in Fig. 2.4.

At the beginning of each new symbol, the signal polarity switches. The maximum signal switching rate in this scheme is called "link frequency" in standards, and abbreviated here as f_m. The symbol

rate is f_m/M [1], where the signal parameter M is the number of subcarrier cycles per symbol. The parameter $M = 1$ corresponds to FM0, though the switching behavior is opposite from Miller encoding: FM0 switches at the maximum rate for data 1, and Miller switches at the maximum rate for data 0.

Increasing M moves communication sidebands away from the carrier. This reduces co-channel interference, but also the data rate. It is effectively repeating each symbol several times, increasing the integration time the interrogator receiver can use to improve the SNR and reduce the link error rate.

2.2.5 Passive RFID Backscatter Modulation in the Frequency Domain

Microwave system theory and measurement are most often performed in the frequency domain. In this work, backscatter spectral characteristics will specifically apply to analysis of mismatch, system bandwidth requirements, and receiver filter designs. It will also help interpret measurement traces on a spectrum analyzer.

The ASK Definition

Equation (2.14) defines the ASK component as switching between $V_{bs}(t) = \{0, \Delta V\}$. Standardized passive UHF tag backscatter spends nearly equal time in each state, so the time-average of $V_{bs}(t)$ will be about $\Delta V/2$ for long FM0- or Miller-encoded data streams. The ASK definition of modulation will therefore contains a carrier component equal to half of the total modulation power.

An instructive signal to examine is an infinite train of FM0 "1" symbols (hexadecimal value `FFFFFFFF...`) or Miller "0" (hexadecimal `00000000...`). This is a square wave with a Fourier sine series representation [75, pp. 111-113],

$$V_{bs}(t) = \frac{\Delta V}{2} \sum_{n=-\infty}^{+\infty} c_n \sin(n2\pi f_m t), \tag{2.16}$$

with coefficients

$$c_n = \begin{cases} \frac{j}{\pi n}(-1)^{(|n|-1)/2}, & (n \text{ odd}) \\ 0, & (n \neq 0 \text{ and even}) \\ \frac{1}{2}, & (n = 0). \end{cases} \tag{2.17}$$

Note that the time-averaged component, which corresponds with $c_n = 0$, is not zero.

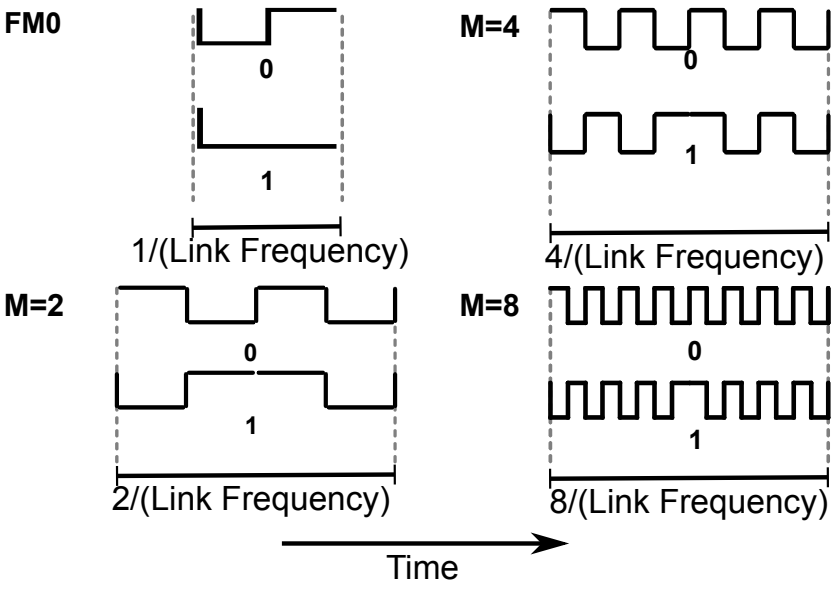

Figure 2.4: RFID tag backscatter digital encoding for FM0 and the various allowed Miller parameters $M = \{2, 4, 8\}$ [1].

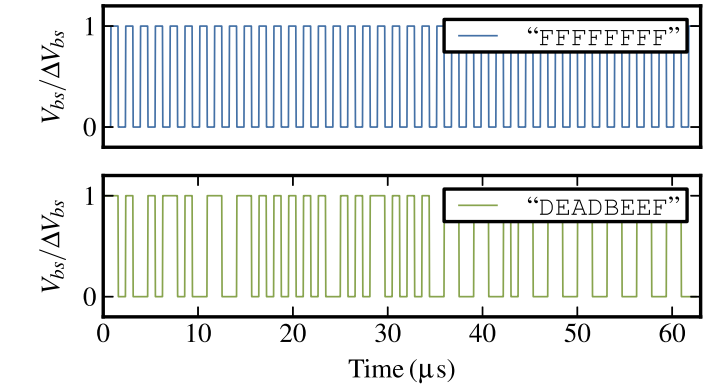

(a)

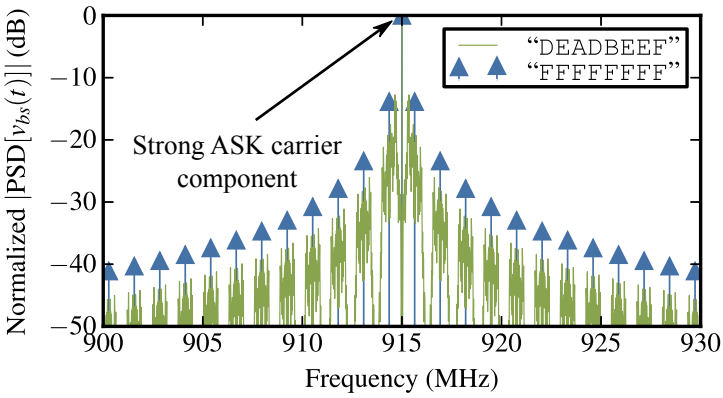

(b)

Figure 2.5: Spectral representation of the modulation component for a simplified ASK square pulse train and backscattered FM0 tag modulation for the arbitrary hexadecimal value `DEADBEEF` in (a) the time domain and (b) the frequency domain.

Let the integration bounds on our Fourier transform for this infinite pulse train approach $T_1 \to -\infty$ and $T_2 \to \infty$. Applying the transform pair $\mathcal{F}[\sin(f_0 t)] = -j\pi[\delta(f - f_0) - \delta(f + f_0)]$ to each sum term of (2.16) gives the transformed baseband signal as

$$\mathscr{F}[V_{bs}(t)](f) = \frac{\Delta V}{2} \sum_{n=-\infty}^{+\infty} c_n \delta(f - n f_m). \tag{2.18}$$

Frequency-shifting the baseband to the carrier for the modulated RF signal $v_{bs}(t)$ gives

$$\mathscr{F}[v_{bs}(t)](f) = \sum_{n=-\infty}^{+\infty} c_n \delta(f - f_c - n f_m). \tag{2.19}$$

Like the baseband, the separation between baseband harmonics is determined by the switching rate f_m.

Since $c_0 = \Delta V/4$, there is a signal at the carrier, even though this is the modulation component. In the frequency domain, this overlaps with the leaked component, so the two are not spectrally independent. Adding and subtracting the two will introduce interference depending on their relative phase.

Figure 2.5 compares this spectrum of $v_{bs}(t)$ as a train of FM0 "1" values against a numerical transform of an arbitrary 32-bit value. The switching rate of the modulation is $f_m = 640\,\text{kHz}$, the maximum rate permitted by RFID standards. As predicted, the carrier component is about $\Delta V/4$. The "0" symbols in the arbitrary-valued signal switch at a different rate than "1" symbols give the "slurred" sidebands.

The BPSK Definition

In the BPSK case, $V_{bs}(t)$ switches between $\pm\Delta V/2$.

Equal time in each state results in a near-zero DC component of $V_{bs}(t)$, but with the same sidebands as ASK. The corresponding Fourier coefficients are therefore

$$c_n = \begin{cases} \frac{j}{\pi n}(-1)^{(|n|-1)/2}, & (n \text{ odd}) \\ 0, & (n \neq 0 \text{ and even}) \\ 0, & (n = 0). \end{cases} \tag{2.20}$$

With no DC component in $V_{bs}(t)$, there is therefore no carrier component in $v_{bs}(t)$.

Is this reasonable to expect in realistic communication of arbitrary data? If the switching duty cycle is exactly 50%, as specified in standards, the only concern is whether equal time is spent in the "long"

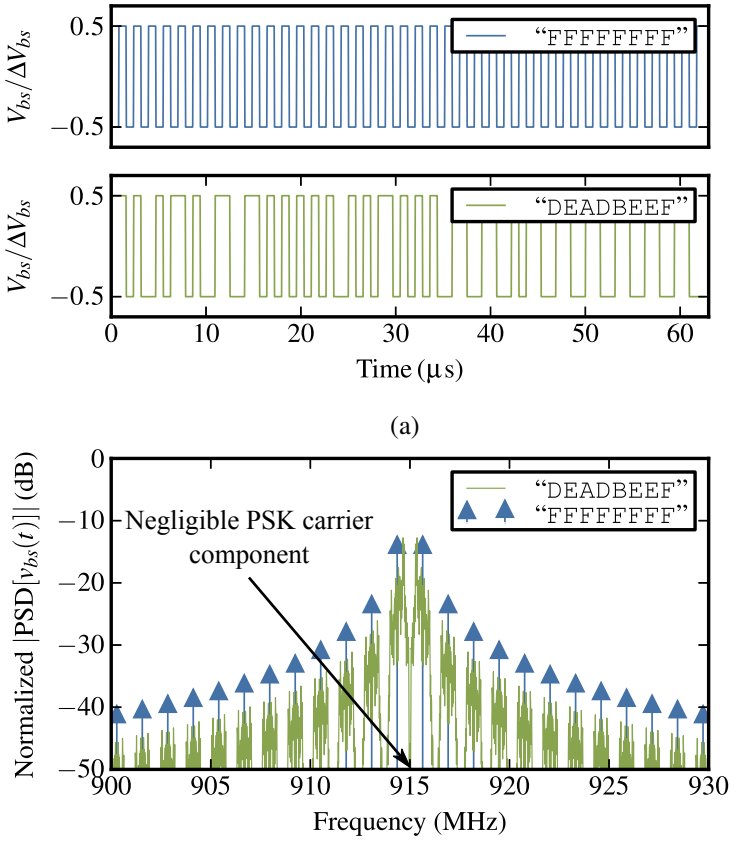

Figure 2.6: Spectral representation of the modulation component for a simplified ASK square pulse train and backscattered FM0 tag modulation for the arbitrary hexadecimal value `DEADBEEF` in (a) the time domain and (b) the frequency domain.

states: FM0-encoded data "0", or Miller-encoded data "1." There are only errors in this case when there are an odd number of "long" states; this error is given by

$$|\max[V_{bs} \text{ DC offset}]| = \frac{|\Delta V/2|}{M \times (\text{Number of bits in } [T_1, T_2])}. \tag{2.21}$$

As an example, a data stream containing a 96-bit tag EPC identification number has error below 1% of $\Delta V/2$ for the FM0 ($M = 1$) case. This is 40 dB less than the modulation power. For Miller modulation ($M = \{2, 4, 8\}$), this error is even smaller.

If the switching duty cycle timing is *not* 50%, there may also be a DC bias. Current standards require this timing to be within 45% to 55%. The V_{bs} received from a "standard-compliant" tag will therefore modulate BPSK with carrier offset less than 5% of $|\Delta V/2|$.

This spectrum is shown in Fig. 2.6, comparing the FM0 hexadecimal `FFFFFFFF...` train against the arbitrary hexadecimal value `DEADBEEF` in Fig. 2.6. The duty cycle here is exactly 50%. The 32-bit `DEADBEEF` data has an odd number of long "0" symbols, but its carrier component is still at least 40 dB below the largest sideband.

It therefore seems reasonable to assume that BPSK modulation and carrier power are spectrally separate, given a standard-compliant tag. Unlike ASK-defined modulation, these components can be measured in either the time or frequency domain.

2.3 Backscatter as Link Power: Z_0-Matched Case

2.3.1 Power in the Time Domain

Assume that a well-matched detector with input impedance Z absorbs our signal $v(t)$. The corresponding leaked power is

$$\text{Delivered leaked power} = \frac{1}{\text{Re}(Z)} \frac{1}{T_2 - T_1} \int_{T_1}^{T_2} |v(t)|^2 dt. \tag{2.22}$$

The integration bounds $T_2 > T_1$ suggest that there is some flexibility in how this power is defined. They need to be stated explicitly for clear discussion of communication power. To ensure small carrier components, they are defined in this thesis as spanning an integral number of symbols. Evaluating (2.22)

with (2.13) gives

$$\text{Leaked power delivered} = \frac{1}{\text{Re}(Z)} \frac{1}{T_2 - T_1} \int_{T_1}^{T_2} \left[\sqrt{2}|V_{leak}| \cos\left(2\pi f_c t + \angle V_{leak}\right)\right]^2 dt. \tag{2.23}$$

Assume that modulation is slow, so that the integration bounds span many carrier cycles ($T_2 - T_1 \gg 1/f_c$), making DC bias in $v(t)$ negligible. This leaked power therefore reduces to

$$\begin{aligned} \text{Leaked power delivered} &= \frac{|V_{leak}|^2}{\text{Re}(Z)} \\ &= \frac{|V(\rho_{L1})|^2}{\text{Re}(Z)} \text{ or } \frac{|V(\rho_{L2})|^2}{\text{Re}(Z)} \text{ (ASK definition)} \\ &= \frac{|\overline{V}|^2}{\text{Re}(Z)} \text{ (BPSK definition).} \end{aligned} \tag{2.24}$$

The power in the tag modulation component of the reflected signal, P_{bs}, can be computed the same way. When we assume the modulation signal is BPSK-modulated, only the phase changes, and the magnitude in either state is $|\Delta V/2|$. Like (2.24), this leads to

$$\text{BPSK modulation power delivered} = \frac{1}{4} \frac{|\Delta V|^2}{\text{Re}(Z)}. \tag{2.25}$$

The ASK modulation includes the carrier component with power $|\Delta V/2|^2/Z$. It is spectrally independent of the BPSK sidebands, so the total modulation power adds to

$$\text{ASK modulation power delivered} = \frac{1}{2} \frac{|\Delta V|^2}{\text{Re}(Z)}. \tag{2.26}$$

This definition of backscattered power matches [44] and the current versions of ISO 18047-6 and ISO 18046-3.

2.3.2 Power in the Frequency Domain

From Parseval's identity [76, p. 211],

$$\int_{-\infty}^{+\infty} |v(t)|^2 dt = \int_{-\infty}^{+\infty} |\mathscr{F}[v(t)](f)|^2 df. \tag{2.27}$$

If we define $v(t) = 0$ outside some finite interval, $[T_1, T_2]$, the left-hand side becomes equivalent to (2.22). Across this period the right side of (2.27) represents a sum of the power at each differential

frequency:

$$\begin{aligned}\text{Signal power} &= \frac{1}{\text{Re}(Z)} \int_{f_c - f_{bw}/2}^{f_c + f_{bw}/2} |\mathscr{F}[v(t)](f)|^2 df \\ &= \frac{1}{2\pi \text{Re}(Z)} \int_{-f_{bw}/2}^{f_{bw}/2} |\mathscr{F}[V(t)](f)|^2 df,\end{aligned} \tag{2.28}$$

across some bandwidth f_{bw}.

The ASK-defined signal includes carrier components from both the leaked and modulation components, so these components cannot be separated directly from spectral power measurements. These measurements *do* give the BPSK components, which are spectrally separate as in Figs. 2.5(b),2.6(b).

2.3.3 Power Absorption and Frequency-Independent Mismatch

BPSK Modulation Power

Let the interrogator have two ports with reflection coefficients ρ_{I1} and ρ_{I2}, connected to E as illustrated in Fig. 2.7. Further, let all reflection coefficients $\rho_{(\cdot)}$ consist of corresponding incident and scattered waves notated as $\rho_{(\cdot)} = b_{(\cdot)}/a_{(\cdot)}$.

In monostatic detection, the RMS voltage at port 1 interface, V_3, is the sum of the forward and reverse waves,

$$\begin{aligned}\frac{V_3}{\sqrt{Z_0}} &= a_1 + b_1 = a_1(1 + \rho_1) \\ &= a_{I1} + b_{I1} = a_{I1}(1 + \rho_{I1})\end{aligned} \tag{2.29}$$

Reflections at this interface cause $a_1 = b_{I1}/(1 - \rho_{I1}\rho_1)$, so the wave incident out of the antenna is related to b_{I1} as

$$a_{I1} = \frac{b_{I1}}{1 + \rho_{I1}} \frac{1 + \rho_1}{1 - \rho_{I1}\rho_1}, \tag{2.30}$$

in terms of the wave that is incident upon the modulation loads, a_L. If we let ρ_L in the modulator switch be such that $a_1(\rho_L)$ switches between $a_1(\rho_{L1})$ and $a_1(\rho_{L2})$, the change in the wave incident upon the interrogator, a_{I1}, becomes

$$\begin{aligned}\Delta a_{I1} &= \frac{b_{I1}}{1 + \rho_{I1}} \left[\frac{1 + \rho_1(\rho_{L2})}{1 - \rho_{I1}\rho_1(\rho_{L2})} - \frac{1 + \rho_1(\rho_{L1})}{1 - \rho_{I1}\rho_1(\rho_{L1})} \right] \\ &= \frac{b_{I1}}{1 + \rho_{I1}} \frac{(1 + \rho_{I1})(\Delta\rho_1)}{(1 - \rho_{I1}\rho_1(\rho_{L1}))(1 - \rho_{I1}\rho_1(\rho_{L2}))},\end{aligned} \tag{2.31}$$

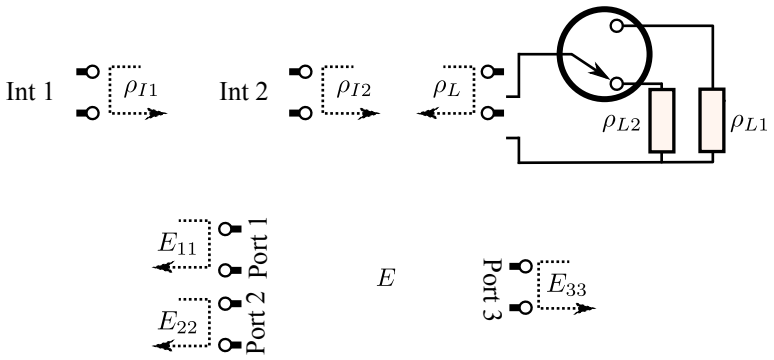

(a) disconnected interrogator and modulation load

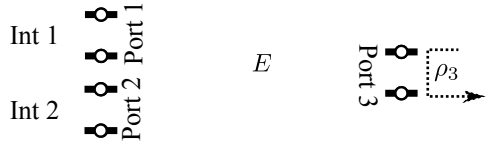

(b) modulator input loaded by arbitrary interrogator

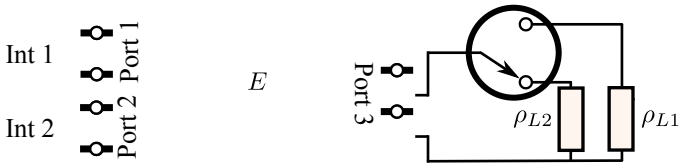

(c) interrogator and modulator loading *E*

Figure 2.7: The network model of Fig. 2.1 with arbitrary interrogator mismatch (a) disconnected, (b) loading the modulator input at port 3, and (c) fully connected.

so

$$\begin{aligned}\frac{|\Delta a_{I1}|^2}{|b_{I1}|^2} &= \left|\frac{\Delta\rho_1}{(1-\rho_{I1}\rho_1(\rho_{L1}))(1-\rho_{I1}\rho_1(\rho_{L2}))}\right|^2 \\ &= \left|\frac{\Delta\rho_1}{(1-\rho_{I1}\overline{\rho}_1)^2-(\rho_{I1}\Delta\rho_1)^2}\right|^2.\end{aligned} \tag{2.32}$$

In terms of BPSK modulation power delivered into the antenna, $P_{bs} = |\Delta a_{I1}|^2/[4(1-|\rho_{I1}|^2)]$, and available transmit power at the carrier, $P_{tx} = |b_{I1}|^2(1-|\rho_{I1}|^2)$,

$$\frac{P_{bs}}{P_{tx}} = \frac{1}{4}\left|\frac{1-|\rho_{I1}|^2}{(1-\rho_{I1}\overline{\rho}_1)^2-(\rho_{I1}\Delta\rho_1)^2}\right|^2 |\Delta\rho_1|^2. \tag{2.33}$$

The denominator term that includes $\Delta\rho_1$ accounts for multiple reflections of modulated waves between the interrogator and the modulation. These multiple reflection effects can sometimes be ignored, as when 1) $|\rho_{I1}|$ is "small," like many fixed interrogator systems with Z_0-matched coaxial ports, or if 2) $|\Delta\rho_1|$ is "small." A reasonable approximation for (2.33) in this special case is

$$\frac{P_{bs}}{P_{tx}} \approx \frac{1}{4}\left|\frac{1-|\rho_{I1}|^2}{(1-\rho_{I1}\overline{\rho}_1)^2}\right|^2 |\Delta\rho_1|^2. \tag{2.34}$$

This case, used in [71], is simply the Z_0 squared matching efficiency of (1.22), with the the BPSK leaked carrier coefficient $\overline{\rho}_1$.

Equation (2.33) in terms of impedances and power wave reflection coefficients is

$$\begin{aligned}\frac{P_{bs}}{P_{tx}} &= \left(\frac{\mathrm{Re}(Z_{I1})}{|Z_{I1}+Z_1(\rho_{L1})||Z_{I1}+Z_1(\rho_{L2})|}\right)^2 |\Delta Z_1|^2 \\ &= \frac{1}{4}|\Delta\tilde{\rho}_1|^2.\end{aligned} \tag{2.35}$$

The compact form based on the power wave term $\Delta\tilde{\rho}_1$ is favored in recent work on this subject [77, 78], but these have only studied modulation inside the tag ($\Delta\tilde{\rho}_L$) . Any passive ρ_L and E results in $|\tilde{\rho}_1| < 1$ and $|\Delta\tilde{\rho}_1| < 4$, so $P_{bs}/P_{tx} < 1$. This is what we should expect, since no energy is being added to the carrier in system. The original source for these reflected power expressions is Green's 1963 thesis [69, p. 31], which assumes port 3 of E is an antenna. Equation (2.35) agrees with Green except for the factor of $1/4$, so Green made the unstated definition that the reflected modulation is ASK.

For the bistatic case, the only changes are in the mismatch effects, and the use of $\Delta\tau_{21}$ instead of $\Delta\rho_1$:

$$\frac{P_{bs}}{P_{tx}} = \frac{1}{4}\left|\frac{(1-|\rho_{I1}|^2)(1-|\rho_{I2}|^2)}{|(1-\rho_{I2}\overline{\rho}_2)^2-(\rho_{I2}\Delta\rho_2)^2|^2}\right| |\Delta\tau_{21}|^2. \tag{2.36}$$

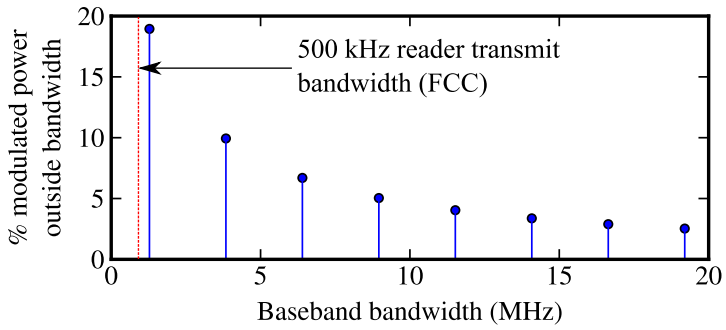

Figure 2.8: Cumulative distribution of harmonic power in a rectangular pulse train with 50% duty cycle switching at the 640 kHz maximum rate of EPC C1G2 tag backscatter.

This expression is particularly cumbersome because receiver matching effects depend on $\Delta\rho_2$, even though the modulation is transmit through $\Delta\tau_{21}$. The author can therefore empathize with the temptation here to use the damped multiple modulation reflections form,

$$\frac{P_{bs}}{P_{tx}} \approx \frac{1}{4}\frac{(1-|\rho_{I1}|^2)(1-|\rho_{I2}|^2)}{|(1-\rho_{I2}\overline{\rho}_2)^2|^2}|\Delta\tau_{21}|^2, \tag{2.37}$$

but for safety encourages goggles and hard hats.

Carrier Power

The Miller- or FM0-encoded carrier power that is reflected and reabsorbed by the interrogator is the same as BPSK leaked power. It is similar to (2.34). For the monostatic case at port 1, it is

$$\begin{aligned}\frac{P_{cw}}{P_{tx}} &= \left|\frac{1-|\rho_{I1}|^2}{(1-\rho_{I1}\overline{\rho}_1)^2}\right|^2 |\overline{\rho}_1|^2, \\ &= \frac{1}{4}|\tilde{\rho}_1(\rho_{L2}) + \tilde{\rho}_1(\rho_{L1})|^2,\end{aligned} \tag{2.38}$$

and for bistatic operation transmitting from port 1,

$$\frac{P_{cw}}{P_{tx}} = \frac{(1-|\rho_{I1})|^2}{|1-\rho_{I1}\overline{\rho}_1|^2}|\overline{\tau}_{21}|^2. \tag{2.39}$$

2.3.4 Frequency-Dependent Mismatch Effects

Is the frequency-independent power absorption model reasonable for UHF RFID? An example of the spectral power content of the broadest EPC C1G2 modulation is shown in Fig. 2.8. Fully 95% of the backscattered power spectrum falls within 10 MHz of the carrier (and proportionally even less bandwidth

at slower modulation rates). Mismatch effects outside this bandwidth can only distort 5% of the total signal power. This is itself unlikely, because it would require extreme mismatch at the sidebands. With EPC C1G2 860-960 MHz carriers, this needs less than 1.5% of "well-matched" bandwidth. This is narrow enough that, at least for EPC C1G2 backscatter, the frequency independence approximation may be quite accurate in many circumstances.

2.3.5 Power Envelope Detection and Self-Jamming Interference

Defining backscattered power as for power envelope detection has enticed several authors, including [79–82], as well as the obsolete 2006 revision of the test standard ISO 18047-6. In this approach, "backscattered power" received from the tag is defined proportional to $\left||V_2|^2 - |V_1|^2\right| = |\Delta|V|^2|$. Let's consider the practical results of this case by example.

Consider a simplistic monostatic case of these for some intuition about the signals presented to the interrogator. The tag antenna is matched to Z_0 ($E_{33} = 0$), loaded by $\rho_{L1} = 0$, and $\rho_{L2} = 1$. Propagation between them is free field (the far field absent any other objects). The interrogator and tag antennas with gain G_{rd} and G_{tag} have phase centers separated by r so that

$$S_{31} = S_{31} = \frac{\sqrt{G_{tag}G_{rd}}}{2k_0 r} e^{jk_0 r} e^{j(\Phi_{tag}+\Phi_{rd})}, \tag{2.40}$$

where $k_0 = 2\pi/\lambda_0$ is the wavenumber corresponding to free-space wavelength λ_0. The Φ terms are the phase response of the two antennas (in radians).

For a Z_0-matched antenna and detector system, (2.6) with (1.11) and (1.12) give us the change in voltage phasor, V_{bs}, as

$$\frac{\Delta V}{V_{tx}} = \frac{G_{tag}G_{rd}}{(2k_0 r)^2} e^{(j2k_0 r)} e^{j2(\Phi_{tag}+\Phi_{rd})}, \tag{2.41}$$

in terms of a transmit phasor V_{tx}. Assume now BPSK-defined modulation. According to this model, V_{leak} is:

$$\frac{V_{leak}}{V_{tx}} = \frac{\overline{V}}{V_{tx}} = E_{11} + \frac{1}{2}\frac{G_{tag}G_{rd}}{(2k_0 r)^2} e^{(j2k_0 r)} e^{j2(\Phi_{tag}+\Phi_{rd})}. \tag{2.42}$$

There are two components here, the "direct" leakage term, E_{11}, and the DC offset of the load modulation that is likely to be much smaller. The change in power envelope states for a reciever, excited by a

transmitted wave with voltage V_{tx}, is $|\Delta|V|^2| = |V_{tx}|^2||V_{leak} + \Delta V/2|^2 - |V_{leak} - \Delta V/2||^2$.

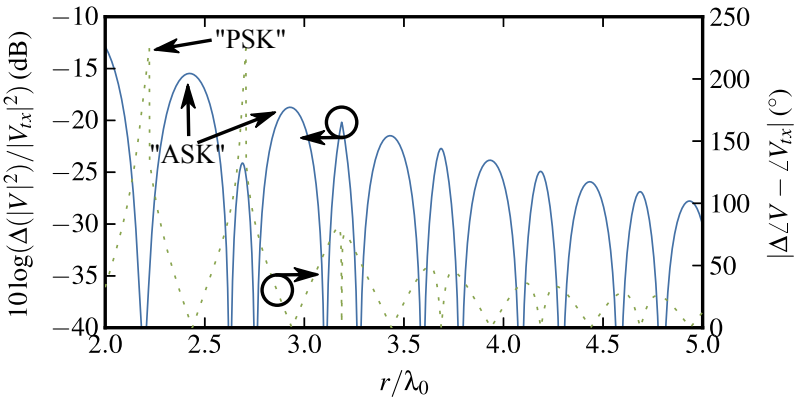

(a)

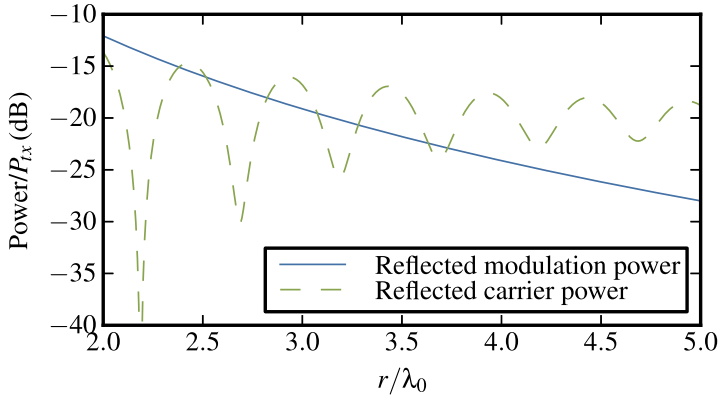

(b)

Figure 2.9: Reflection coefficient magnitudes (a) plotted as a power and phase envelope, and (b) with leaked interference removed by separating BPSK leakage and modulation components. $G_{tag} = 0\,\text{dBi}$, $G_{rd} = 6\,\text{dBi}$, $E_{11} = 0.1\angle 45°$, and $\Phi_{tag} = \Phi_{rd} = 0°$. The circled arrows indicate the axis that applies to the encircled trace.

Figure 2.9(a) shows magnitude and phase envelopes of V, swept with r with arbitrary but realistic fixed values. In the states marked "ASK", there is almost no change in power between the two backscatter states, making the communication effectively undetectable to a power envelope detector. This is why RFID backscatter detectors need in-phase and quadrature (IQ) demodulation for either reliable communication or repeatable measurements.

For comparison, power as defined in this work in Section 2.3.1 is plotted in Fig. 2.9(b). This shows the backscattered power falling as r^4, and reflected carrier power staying nearly constant, except for the slight effect of the ASK carrier signal offset.

2.3.6 Power Conservation at Network Interfaces

A valid model will ensure energy is conserved. In steady state, this is equivalent to conservation of power. This is also important in link analysis, which needs power quantities that can be directly compared.

Passive UHF RFID tags use ASK load modulation, because the "match" state can absorb and rectify the incident carrier as a power supply. It is well-known that the penalty in use of ASK (which is required for binary-modulated harvesting systems) instead of BPSK load modulation is a factor of 4 in power [77]. For ASK load modulation switched according to EPC C1G2 encoding schemes, an ideal rectifier could absorb half of the incident power. This leaves a quarter of the incident power. Where did it go?

The key to answering this question is to follow all of the power components that we have defined already: transmission loss, the backscattered modulation component, the leaked carrier, and power delivered into the tag load.

Z_0-matched Case

Consider a well-matched monostatic interrogator attached directly to a modulator ($E_{11} = E_{33} = 0, E_{31} = E_{13} = 1$). Equations (2.9), (2.25), and (2.25) combine to give

$$P_{bs} = \frac{|\Delta V|^2}{4Z_0} = P_{tx}\frac{|\Delta\rho_L|^2}{4}. \tag{2.43}$$

The actual carrier power as measured on a spectrum analyzer is

$$P_{cw} = \frac{|\overline{V}|^2}{Z_0} = P_{tx}|\overline{\rho}_L|^2, \tag{2.44}$$

where $\overline{\rho}_L$ is the average reflection coefficient of the tag loads. This is zero when the average ρ_L (and therefore the average baseband voltage V) is equal to zero. As such, it is not the same as "leaked power" for ASK.

It has been identified as distinct from "structural-mode" antenna scattering [78] (discussed in the Chapter 4).

Some power is also absorbed by the modulator loads, depending on mismatch and the duty cycle spent in each state. For ASK, this is by design. For $\rho_L = \{0, 1\}$ loads at 50% duty cycle, the loads absorb all of the power half of the time, or half of the incident power.

		ASK loads	BPSK loads
Load states	$\{\rho_{L1,L2}\}$	{0,1}	{-1,1}
Reflected ASK	P_{bs}	$P_{tx}/2$	$2P_{tx}$ (!)
Reflected carrier	P_{cw}	$P_{tx}/4$	0
Absorbed power	P_L	$P_{tx}/2$	0
Total (ASK definition)		$1.25P_{tx}$ (!)	$2P_{tx}$ (!)

(a) with ASK-defined modulation

		ASK loads	BPSK loads
Load states	$\{\rho_{L1,L2}\}$	{0,1}	{-1,1}
Reflected BPSK	P_{bs}	$P_{tx}/4$	P_{tx}
Reflected carrier	P_{cw}	$P_{tx}/4$	0
Absorbed power	P_L	$P_{tx}/2$	0
Total (BPSK definition)		P_{tx}	P_{tx}

(b) with BPSK-defined modulation

Table 2.1: Power flow for a Z_0-matched interrogator connected to a backscatter modulator

Now let the load modulation be realized as ideal ASK or BPSK load modulation. Corresponding power quantities are summarized in Table 2.1, for each of the ASK and BPSK backscattered power definitions.

The results for ASK modulation definition with BPSK loads are strange. For BPSK tag loads, it appears possible for the interrogator to receive twice as much modulation power as it transmit. This clearly violates conservation of energy. What happened? The ASK-defined modulation power assumes a carrier component equal to the modulation component, but there is no reflected continuous-wave (CW) power component — the average of ρ_L is 0. This could be remedied somewhat with *leaked power* definition by subtracting the "leaked" carrier component, but this needs a nonphysical negative leaked carrier power.

The BPSK definition, in contrast, results in power levels that conserve energy.

General Case of BPSK Passivity

In fact, RFID backscatter modulation power is conserved at any interface with the BPSK model.

Consider the sum of all power absorbed at an interface in a backscatter modulation system:

$$\sum P = P_{bs} + P_{cw} + P_{L1} + P_{L2}. \tag{2.45}$$

The two terms on the left are power reflected back to the generator and absorbed, and $P_{L1,L2}$ are the

power delivered into each modulation load. The power wave reflection coefficient at this interface switches between $\tilde{\rho}_{L1}$ and $\tilde{\rho}_{L2}$. From the theory developed in this chapter, the total of all absorbed power is

$$\begin{aligned}\sum P =& \frac{1}{4}|\tilde{\rho}_{L2} - \tilde{\rho}_{L1}|^2 P_{tx} + \frac{1}{4}|\tilde{\rho}_{L2} + \tilde{\rho}_{L1}|^2 P_{tx} + \frac{1}{2}(1 - |\tilde{\rho}_{L1}|^2)P_{tx}\frac{1}{2}(1 - |\tilde{\rho}_{L2}|^2)P_{tx}. \\ =& \frac{1}{4}[|\tilde{\rho}_{L2}|^2 + |\tilde{\rho}_{L1}|^2 - 2|\tilde{\rho}_{L2}\tilde{\rho}_{L1}|\cos(\angle\tilde{\rho}_{L2} - \angle\tilde{\rho}_{L1})]P_{tx} \\ &+ \frac{1}{4}[|\tilde{\rho}_{L2}|^2 + |\tilde{\rho}_{L1}|^2 + 2|\tilde{\rho}_{L2}\tilde{\rho}_{L1}|\cos(\angle\tilde{\rho}_{L2} - \angle\tilde{\rho}_{L1})]P_{tx} \\ &+ 1 - \frac{1}{2}[|\tilde{\rho}_{L1}|^2 + |\tilde{\rho}_{L1}|^2]P_{tx} \\ =& P_{tx}\end{aligned} \tag{2.46}$$

As expected, the sum of dissipated power equals the sum of power input into the system. This is fully general for any passive backscatter modulation load attached to a linear network.

2.4 Summary

Backscatter power is not explicitly derived in terms of measurable signals by standards or other technical technical literature. Passive UHF RFID encoding makes BPSK independent of the carrier, simplifying spectral analysis and ensuring that energy is conserved at all reference points for arbitrary passive tag modulation loads.

Digitally modulated backscatter can be analyzed as either ASK or BPSK plus an appropriate baseband DC offset. Defining the signal as BPSK, and not as ASK as is effectively chosen in current test standards [41], has several advantages that arise from orthogonality with carrier frequency. Defining FM0- or Miller-modulated backscatter as BPSK is spectrally separate from the carrier, and can be measured in the frequency domain. Finally, expressions for power conservation are straightforward with this definition because the modulation power does not incorporate energy that is redundant with the leaked carrier, which does not even exist for ideal PSK load modulation.

The important limiting assumptions of the signal power defined in this chapter and used in this thesis are as follows:

(1) Switching transients in V must decay rapidly enough to allow two clearly defined states. This

requires slow frequency and low dispersion in propagation and matching relative to the signal bandwidth.

(2) 50% duty cycle (as in the encoding of the EPC C1G2 and ISO 18000-6C RFID standards).

(3) The bandwidth of the baseband signal $\mathscr{F}[V_{bs}(t)](f)$ must be less than twice the carrier, $2\pi f_c$.

The remainder of this thesis assumes that these are true.

Material in this chapter originated in the following peer-reviewed publications by the author:

D.G. Kuester, D.R. Novotny, J.R. Guerrieri, Z. Popović, "Baseband Voltage and Power in Load-Modulated Digital Backscatter," *IEEE Antennas and Wireless Propagation Lett.*, accepted for publication.

Chapter 3

Passive Backscatter Link Power Characterization

Milou: «Tintin! Es-tu mort? Dis-moi oui ou non, mais reponds-moi! »
Snowy: "Tintin! Are you dead? Say yes or no but answer me!"

Hergé, *Tintin au pays des Soviets* (1930)

The fundamental goal of link modeling is to estimate signal and noise levels to forecast wireless communication quality. This can help application engineers identify and specify performance parameters, and weigh cost against performance in hardware selection or design.

This is not a new idea in either digital communication in general [83, p. 118] or passive RFID [84, 85]. A link model with receiver SNR or SIR performance information can lead to estimates of data error rates like bit error rate (BER) or frame error rate (FER) or their complimentary success rates. The coverage of communication, which is often discussed in wide area systems like cellular networks, is the proportion of a physical area or volume in which the communication error rate or success rate is acceptable.

Communication between readers and tags in all modern RFID systems is bi-directional and therefore employs two different links. Both links need low error rates for reliable communication. Passive UHF

	Forward link parameters	Return link parameters
Reader hardware:	Transmit power (up to 30 dBm)	Sensitivity (-85 dBm to -60 dBm)
Environment:	Reader to tag range (up to about 15 m) Reader antenna gain pattern (up to 6 dBi at full power) Reader antenna match losses (typically negligible) Polarization (typ. 0 dB loss to 3 dB loss)	
Tag hardware	Sensitivity (about -10 dBm to -20 dBm)	Differential RCS (typically at least 0.005 m^2)

Table 3.1: Typical link power parameters in free-space analysis

RFID is composed of a forward link (downlink) the reader-to-tag transmission, and return link (uplink), the tag-to-reader backscatter. In the idealized free field (far field propagation in free space), these links depend on the parameters are summarized in Table 3.1 [86], which themselves depend on frequency and sometimes power. It is often assumed that the forward link limits overall communication reliability, but we will show in Chapter 6 that this is not always true with modern commercial hardware.

Despite the large number of variables in these links, passive UHF RFID literature typically quotes link performance as a single "tag read range" number (sometimes as a function of frequency). The term is not standardized, but seems to suggest the maximum separation between reader and tag antennas at some acceptable error rate. A subset of the measurement details are sometimes given that may hint at when the metric applies. Usually, however, it is difficult to identify the radio environment where tag read range applies, and even more difficult to use it to predict behavior in other environments.

This chapter investigates link operation with network theory, with the goal of leveraging redundancy between losses in each link to better understand and predict the behavior of the return link. Tag BPSK radar cross section and sensitivity that characterize behavior conveniently in free space emerge as special cases of this analysis. The final result, however, is an alternative to radar cross section for bounding backscattered power in monostatic or "quasi-monostatic" return links with passive tags. This parameter gives a deterministic lower bound to backscattered power as a function of tag tuning in any environment.

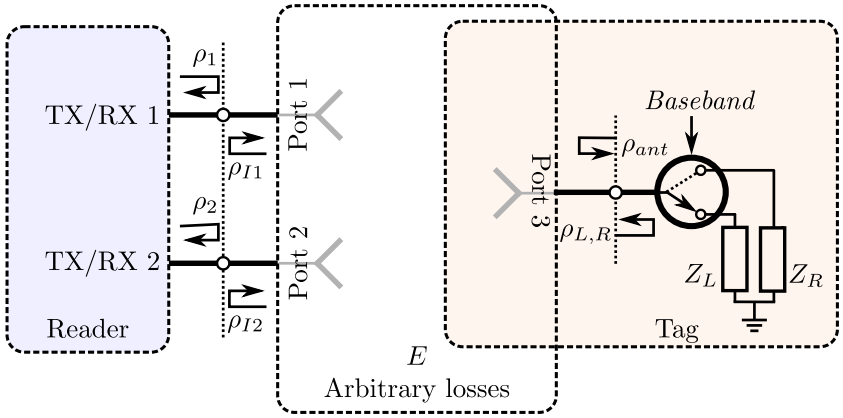

Figure 3.1: Linearized S-parameter model of reader and tag signaling. In return modulation, the tag chip switches between $\rho_{L,R}$ (impedances $Z_{L,R}$). The tag antenna, loaded slightly by the reader, presents ρ_3 (impedance Z_3) to the chip. Backscatter at ports 1 and 2 is produced by interaction between the tag antenna and the switching chip load.

3.1 Reader-Loaded Link Model

A network model of interaction between a reader and tag is illustrated in Fig. 3.1, following [43] and [46]. The S-parameter network E contains all transmission effects between reader ports and a tag chip, including cables, antennas, and propagation effects. Ports 1 and 2 of E are attached to the monostatic or bistatic reader. Port 3 is the interface between the tag's chip and antenna. The reader transmits into port 1 or 2; each is assumed not to load the other.

We adopt a change of variables compared to the previous chapter for the special case of passive tags: the power harvesting chip impedance state is $Z_{L1} \rightarrow Z_L$, and the reflective modulation chip impedance state is $Z_{L2} \rightarrow Z_R$. Realistic values are on the order of $Z_L \approx (15 - j150)\,\Omega$, $Z_R \approx (12.5 - j100)\,\Omega$ [87], and $Z_3 \approx Z_L^*$. Reader ports and antennas are usually designed to match $50\,\Omega$.

3.2 The Forward Link as a Microwave Network

3.2.1 Propagation Power and Loss

Available transmit power from the reader (P_{tx}) is related to S-parameter traveling waves incident into either port ($a_{1,2}$) with [56]

$$P_{tx} = \frac{|a_{1,2}|^2}{1 - |\rho_{I1,I2}|^2}. \tag{3.1}$$

Likewise, available power from the tag antenna, P_3, is related to the corresponding scattered pseudowave b_3 as

$$P_3 = \frac{|b_3|^2}{1 - |\rho_3|^2}, \tag{3.2}$$

where ρ_3 is E_{33} loaded through E by the reader. The exact expression for ρ_3 is long and uninformative, but $\rho_3 \approx E_{33}$ if the reader is well matched or E transmission coefficients are small. The proportion of available transmit power that is available out of the tag antenna is the available power gain [62, p. 539],

$$\frac{P_3}{P_{tx}} = \frac{1}{L_{tx}} = |E_{31,32}|^2 \frac{1 - |\rho_{I1,I2}|^2}{|1 - E_{11,22}\rho_{I1,I2}|^2(1 - |\rho_3|^2)}. \tag{3.3}$$

Its inverse, L_{tx}, is the transmission loss. Current systems can to turn on well-matched tags with up to about 45 dB of loss.

3.2.2 Tag Turn-on as a Nonlinear Operating Point

A well-matched state-of-the-art tag chip must absorb on the order of $P_{L0} = -15\,\text{dBm}$ to turn on. Ambient noise power is much smaller in typical environments, so turn-on is a threshold effect that depends on absolute P_L, not power relative to noise (SNR). As a result, there is a sharply-defined power available from the tag antenna, P_{30}, where the tag load is at the turn-on threshold. Any P_3 can be expressed relative to this as $P_3 = \bar{p}P_{30}$. Excess power $\bar{p}$ can be interpreted as "power level relative to turn-on." If it is expressed in dB, it can be read "dB above turn-on."

The BER distribution as a function of P_3 is closely approximated as a step function, which is *deterministic* with input power. Interference effects in this link are limited: would-be "interferers" may instead help to power the tag [40]. This is in sharp contrast with an ideal AWGN-limited channels, for which the BER distribution is the error function [84]. The AWGN *frame* failure rate requires the success of many bits in sequence, and is therefore poorer but still a random variable.

A sensitive reader can remotely detect whether a tag is on by detecting backscattered power, P_{bs}, at

some power level:

$$P_{bs} = 0, \text{for } P_{tx} < P_{tx0}, \tag{3.4}$$

where P_{tx0} is the minimum power to turn on. All terms on the right of (3.3) are linear, and thus independent of operating point, $P_3/P_{tx} = P_{30}/P_{tx0}$. Therefore,

$$\bar{p} = \frac{P_{tx}}{P_{tx0}} = \frac{P_3}{P_{30}}. \tag{3.5}$$

In other words, the operating point has the same meaning either at the reader ports or inside the tag.

This concept is exploited (though not explained) in ISO 18047-6 [41], prescribing σ_Δ measurements at $\bar{p} = 120\%$ (0.8 dB). Because $\bar{p}$ permits wireless insight into power levels inside the tag, it is the basis for linearity test and analysis in this thesis.

3.2.3 Power Delivery to the Tag Chip Load

A passive UHF RFID chip has the power harvesting load impedance Z_L except at 50% duty cycle during tag-to-reader modulation, to maximize time-averaged rectified power. It is the convention of this thesis that power delivery is defined for the chip in its power harvesting impedance Z_L, and not in reflective state Z_R.

Available power from the antenna (P_3) is related to power delivered to the tag chip (P_L) as

$$\begin{aligned} P_L =& P_3 \eta_L \\ =& \frac{P_{tx}}{L_{tx}} \eta_L. \end{aligned} \tag{3.6}$$

This defines $0 \leq \eta_L \leq 1$ as the match efficiency between the tag antenna and the tag chip.

At the turn-on operating point, we define the chip sensitivity P_{L0}:

$$P_{L0} = P_{30} \eta_{L0}. \tag{3.7}$$

Nonlinear Matching Effects

Physical tag loads are realized as nonlinear diodes or transistors, so their input impedances at the carrier frequency vary with input power (through $\bar{p}$) and the tag antenna impedance at harmonics of the carrier

nf_c ($n = 0, 1, 2, 3, ...$). Propagating this dependence into (1.21) gives an unwieldy result for η_L:

$$\begin{aligned}\eta_L(\bar{p}, Z_3(nf_c)) &= \frac{(1-|\rho_3|^2)(1-|\rho_L(\bar{p}, Z_3(nf_c))|^2)}{|1-\rho_3\rho_L(\bar{p}, Z_3(nf_c))|^2} \\ &= \frac{4\text{Re}\{Z_L(\bar{p}, Z_3(nf_c))\}\text{Re}\{Z_3\}}{|Z_L(\bar{p}, Z_3(nf_c)) + Z_3|^2}.\end{aligned} \tag{3.8}$$

If the Z_3 and Z_L are conjugate-matched at the fundamental, $\eta_L = 1$ and all power available at the antenna terminals is delivered from the antenna into the chip. Ohmic losses inside the antenna are included as part of the transmission network.

This efficiency is different from the RF-to-DC conversion efficiency in rectifier design. For example, a rectifier could be a good linearized conjugate match $Z_L = Z_3^*$, but any additional loss inside the rectifier will reduce η_L.

Parasitic Packaging Effects

Equation (3.8) is meant to predict power absorption performance from impedances that can be predicted in advance by measurement, simulation, or theory. Unfortunately, the bond between the tag chip and antenna introduces parasitic effects that are likely to contribute to differences between measurement test fixtures, simulations, and the final bonded tag [88, 89]. The convention in this work, illustrated in Fig. 3.2, is to incorporate these into the chip impedances Z_L and Z_R. This way, Z_3 can be thought of as "fixed." Both Z_L and Z_R already depend on Z_3 because of their nonlinearity, so incorporating the correction for parasitics simply changes this existing dependence.

Time Dependence

So far, Z_L and P_{L0} have been tacitly assumed to be time-invariant at "fixed" reader transmit power levels on the scale of many carrier frequencies. Sadly, this is not true. The time-dependence of these parameters is a large and complicated problem that could be its own thesis chapter, as in in [26, pp. 18-22]. Here, time dependence will be addressed qualitatively enough to understand link performance concerns.

One reason is that the reader transmit power is not really fixed. By definition, the ASK reader-to-tag modulation varies the transmit power of the reader. This variation toggles the power supply broadcast to the tags, which must have a small DC buffer capacitor to maintain supply during baseband "off" cycles.

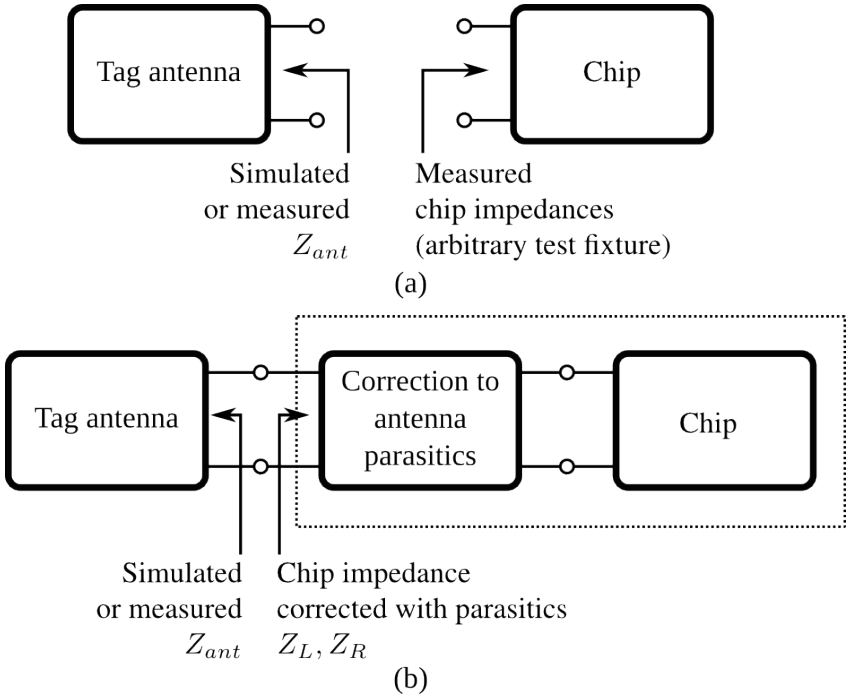

Figure 3.2: The network interface between a tag antenna and chip is not well-defined. Impedances from (a) simulations or measurements in a test fixture do not describe (b) additional circuit effects introduced by bonding the chip to the antenna. The convention in this work is to incorporate these additional effects into the chip impedances.

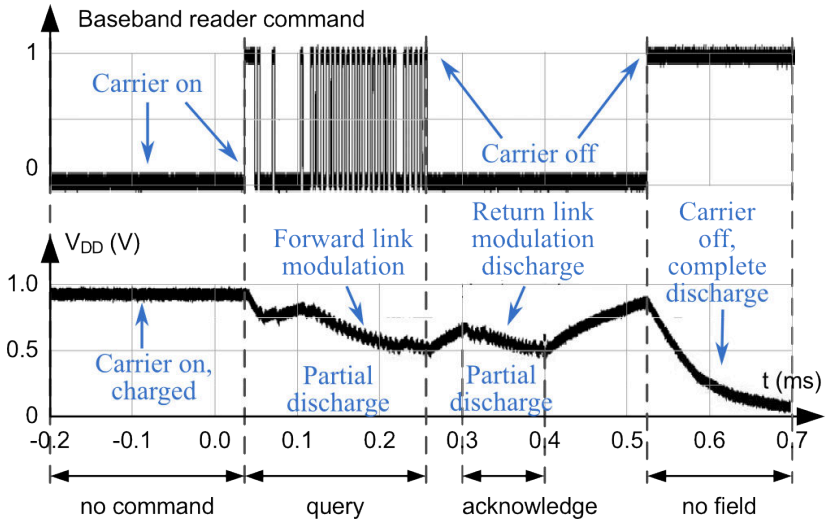

Figure 3.3: The DC supply voltage within an EPC C1G2/ISO 18000-6C tag during a communication round [90].

Solving this problem by increasing the buffer capacitance increases chip area and cost, and is also limited by the charging time permitted by the protocol. At best, this scheme "averages" DC supply across the order of 10 µs, resulting in DC supply voltage droop and less available DC power. This is illustrated as the first droop in Fig. 3.3, settling to about half of the CW supply voltage. If there is too much voltage droop, the tag chip turns off and fails to respond to the reader.

The act of shorting the chip's input impedance during return-link backscatter modulation also effectively switches the tag power supply on and off, even though the reader is transmitting fixed CW during this period. The chip's DC buffer capacitance helps again, but has similar problems as the forward link. This is visible as the shorter droop labeled "chip's reply" in Fig. 3.3.

The DC load presented by the tag's digital circuitry is also not constant. The rectifier is far from an ideal voltage source, and may droop when the load draws too much current. The tag must use power during both links: 1) decoding requests from the reader, 2) accessing its memory, 3) processing a reply, and perhaps performing extended functions like sensing. If the load exceeds the sourcing capability of the rectifier at any stage in communication, the tag might return an incomplete or invalid response that prevents valid communication. Memory write operations, for example, use more power and thus correspond with poorer sensitivity for all commercial passive chips, e.g., [91, 92].

Further, Z_L itself varies with the DC load. The detailed nature of this dependence is determined by the rectifier topology; the charge pumps used in RFID involve trade-offs between efficiency and isolation between the DC load and RF input impedances [93, p. 31]. Time-varying Z_L implies time-varying η_L as well, so an "optimal" power harvesting match during forward-link modulation can in principle be quite different if the loading is not carefully spread out. Fortunately, at least for some commercial chips, these effects have been observed to be slight [87].

If we are given only a fully integrated tag, these effects are extremely difficult to measure or quantify. They do help identify factors that may affect chip sensitivity P_{L0}:

(1) Signal encoding parameters in both links: 1) symbol rate, 2) timing, 3) modulation depth, etc. These factors have been shown to affect P_{L0} by less than 0.25 dB [94].

(2) Data content: a) singulation vs. memory read vs. memory write, b) how much data is sent, c) the

extent of processing required.

These data-dependent parameters are much more complicated to predict than those listed in (3.8), but must be measured for complete tests.

3.3 Return Link Loss and Efficiency

3.3.1 Modulation Efficiency

The main circuit performance parameter inside the tag characterizes the modulation power accepted by the tag antenna as a fraction of the incident carrier power available into the tag chip. This takes exactly the same form as (2.33), but is evaluated with $\rho_{I1} \to \rho_3, \rho_1(\rho_{L1}) \to \rho_L$, and $\rho_1(\rho_{L2}) \to \rho_R$:

$$\begin{aligned}
&\eta_{mod}(\bar{p}, Z_3(nf_c), \text{reader command}) \\
&\qquad = \left(\frac{1 - |\rho_3|^2}{|1 - \rho_3 \rho_L(\bar{p}, \rho_3(nf_c))||1 - \rho_3 \rho_R(\bar{p})|} \right)^2 |\rho_R(\bar{p}) - \rho_L(\bar{p}, Z_3(nf_c))|^2 \\
&\qquad = \left(\frac{\text{Re}(Z_3)}{|Z_3 + Z_R(\bar{p})||Z_3 + Z_L(\bar{p}, Z_3(nf_c))|} \right)^2 |Z_R(\bar{p}) - Z_L(\bar{p}, Z_3(nf_c))|^2 \\
&\qquad = \frac{1}{4} |\tilde{\rho}_R(\bar{p}) - \tilde{\rho}_L(\bar{p}, Z_3(nf_c))|^2.
\end{aligned} \tag{3.9}$$

To include this chapter's nonlinear compression effects, this expression depends on $\bar{p}$. The expression is identical for both monostatic and bistatic operation. For passive $\rho_{L,R}$, modulation efficiency is bounded by $0 \leq \eta_{mod} \leq (1 + \sqrt{1 - \eta_L})^2$.

The definition of "modulation efficiency" in (3.9) specifically relates backscattered BPSK modulation to the available incident carrier power. Use of BPSK has the specific advantages that were discussed in Chapter 2. Previous work that uses this type of term does not explicitly state the type of reflected modulation, but it can be inferred from the normalization factor. The normalization as $|\tilde{\rho}_R - \tilde{\rho}_L|^2/4$ given here corresponds with BPSK, as in [71, 95]. Normalization as $|\tilde{\rho}_R - \tilde{\rho}_L|^2/2$ is reflected ASK, which is used by [44]. Many others use $|\tilde{\rho}_R - \tilde{\rho}_L|^2$ [43]; these come from [69, p. 31] by way of [77].

The dependence on the antenna properties shows that this backscatter is produced not by the switching tag chip impedance, but by its interaction with the antenna as a circuit element. Just as in the forward link, the tag antenna is still assumed linear, even though the interactions between it and the tag chip are

not.

3.3.2 Link Power and Loss

Monostatic backscatter presented at a reader after passing through the environment are already given in terms of pseudowave scattering parameters (2.6). These scattering parameters are related to backscatter power absorbed by the reader in (2.33), tag modulation power efficiency defined in (3.9), and the transmission path loss is defined in (3.3). Combining all of these equations lets us decompose the monostatic link budget into efficiencies and link losses,

$$\frac{P_{bs}}{P_{tx}}\frac{\eta_{tx}}{\eta_{rx}} = \frac{\eta_{mod}(\bar{p})}{L_{tx}^2} \text{ (monostatic through port 1).} \tag{3.10}$$

The factor of η_{tx}/η_{rx} will be addressed in the next subsection.

The bistatic expression for this is derived much the same way, except substituting power expressions into (2.2):

$$\frac{P_{bs}}{P_{tx}}\frac{\eta_{tx}}{\eta_{rx}} = \frac{\eta_{mod}(\bar{p})}{L_{tx}L_{rx}} \text{ (bistatic through ports 1 and 2).} \tag{3.11}$$

The difference here are

(1) L_{tx}^2 is split into separate path losses that correspond to the bistatic transmit and receive paths between the reader and tag, and

(2) η_{tx} and η_{rx} now refer to ports 1 and 2 of the reader and environment, and their ratio becomes much more complicated.

3.3.3 Reader Mismatch Effects on Backscatter

Let us consider the term η_{tx}/η_{rx} that falls out of the link derivation but does not appear elsewhere in the literature. In the monostatic case, evaluating each match efficiency expression reduces to

$$\frac{\eta_{tx}}{\eta_{rx}} = \left(\frac{|(1-\rho_{I1}\overline{\rho}_1)^2 - (\rho_{I1}\Delta\rho_1)^2|^2}{|1-E_{11}\rho_{I1}|^4}\right)^2, \tag{3.12}$$

which is very ungainly, even though many terms in transmit match efficiency, $0 \leq \eta_{tx} \leq 1$, and receive efficiency, $0 \leq \eta_{rx} \leq 1$ have cancelled. The dependence on $\Delta\rho_1$ is particularly inconvenient because it is

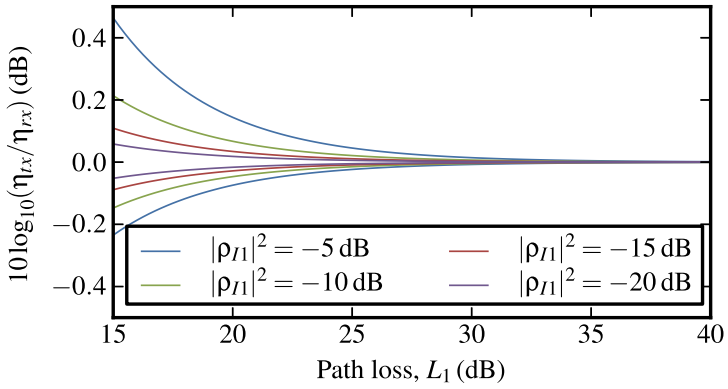

Figure 3.4: Absolute worst-case upper and lower bounds for η_{tx}/η_{rx} when $|E_{11}|^2 < -5$ dB for the values of $|\rho_{I1}|^2$ shown. Realistic "far-field" values of path loss are above approximately 15 dB.

unknown in practical operation. These are the matching terms in the forward and return link expressions that do not cancel. This is because the forward link available power model presents the environment *not* loaded by the tag; in contrast, the return link environment model presents the time-averaged reflection coefficient of the environment loaded by the tag, and effects of multiple reflections of the modulation wave.

Under certain conditions, like the approximation of (2.34), this term becomes negligible:

(1) when the reader is matched to Z_0 so that $|\rho_{I1}| = 0$, or

(2) when both a) the tag loads do not significantly load the reader antenna, so that $E_{11} \approx \overline{\rho}_1$, and b) $|\rho_{I1}\Delta\rho_1|^2 \ll |1 - \rho_{I1}\overline{\rho}_1|^2$, or

(3) both (1) and (2).

One way to achieve this and make η_{tx}/η_{rx} vanish is to define the reference impedance Z_0 to be the same as the (real-valued) input impedance of the reader, so that *by definition* $\rho_{I1} = 0$.

Figure 3.4 illustrates absolute maximum and minimum bounds for η_{tx}/η_{rx} for return loss in ρ_{I1} and E_{11} greater than 5 dB. These occur when all terms are entirely real-valued, adding exactly in phase or out of phase. Effects from ρ_1 are strongest when reflections from the modulator have a strong carrier frequency component, and effects of $\Delta\rho_1$ are strongest when reflections from the modulator have strong sideband components. The illustrated bounds assume the nonphysically bad case of the modulator

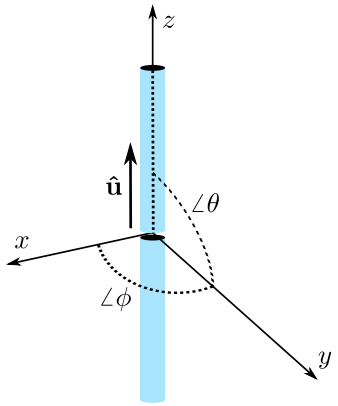

Figure 3.5: Definition of antenna pattern orientations θ and ϕ and polarization unit vector $\hat{\mathbf{u}}$, following [96, p. 33]. The example polarization is specific to linear-polarized antennas like the dipole shown.

reflecting all incident power as both carrier *and* modulation in order to guarantee conservative bounds.

3.4 Free Field Tag Performance Characterization

Standard free-space forward and return link metrics now derive trivially by substituting free space power loss for L via the Friis transmission equation. These exist elsewhere in the literature, but details in the preceding link and signal discussion connect with broader wireless communication concepts. These will help us identify the important parameters that affect backscattered power received by the reader within this free space case. These depend on the reader and tag antenna orientations illustrated in Figs. 3.5 and 3.6.

3.4.1 Power harvesting performance: sensitivity

With the terms defined so far, the Friis transmission equation for power loss in far field, free space ("free field") propagation is [96, p. 95]

$$\frac{P_3}{P_{tx}} = \frac{1}{L} = \left(\frac{\lambda}{4\pi r}\right)^2 G_3(\theta_{tx}, \phi_{tx}) G_{rx}(\theta_3, \phi_3) |\hat{\mathbf{u}}_3 \cdot \hat{\mathbf{u}}_{tx}|^2. \tag{3.13}$$

The separation between the reader and tag antennas is r and the wavelength in the propagating medium is $\lambda = c/f$. The reader and tag antennas have total gain G_{tx} and G_3, with corresponding unit polarization vectors $\hat{\mathbf{u}}_3$ and $\hat{\mathbf{u}}_{tx}$. The corresponding orientations of these antennas are (θ_{tx},ϕ_{tx},$\angle\hat{\mathbf{u}}_{tx}$) and

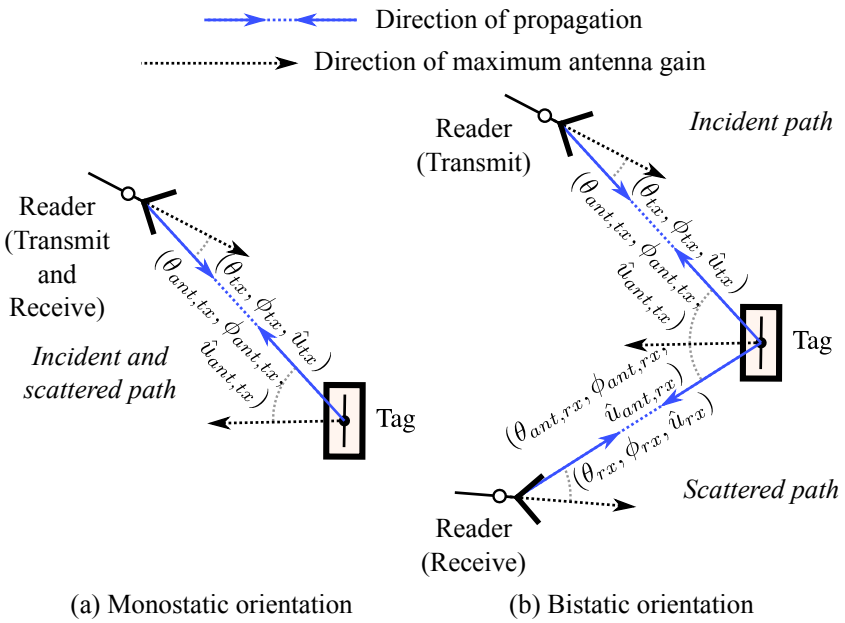

(a) Monostatic orientation (b) Bistatic orientation

Figure 3.6: Orientations of reader and tag antennas for (a) monostatic or (b) bistatic operation, illustrated on a two-dimensional projection. The θ, ϕ, and $\hat{\mathbf{u}}$ of each antenna are as defined in Fig. 3.5.

(θ_3,ϕ_3,$\angle\hat{\mathbf{u}}_3$).

Use of this expression in this form is problematic given the tight integration between the tag antenna and chip. We can work around this by combining P_3 and G_3 terms into the plane wave power density, W, [38, 39, 97]. Other authors have also related this to the electric field. The only operating characteristic we can identify externally is the plane wave impinging on the tag at its turn-on threshold, $W|_{\bar{p}=1} = W_0$:

$$W_0(f, \theta_3, \phi_3, \hat{\mathbf{u}}_3) = P_{30}(f, Z_3)\frac{4\pi}{\lambda^2 G_3(f, \theta_3, \phi_3)}. \tag{3.14}$$

This encapsulates only the parameters of the tag, except for the dependence on the incident wave polarization through $\hat{\mathbf{u}}_{tx}$. Like P_3, W_0 varies with the power consumption of the tag.

A well-matched reader-antenna system can excite this power density by transmitting P_{tx0}, such that

$$\frac{W_0}{P_{tx0}} = \frac{G_{rd}}{4\pi r^2}|\hat{\mathbf{u}}_3 \cdot \hat{\mathbf{u}}_{tx}|^2, \tag{3.15}$$

where G_{rd} is the reader antenna gain toward the tag, and r is the range between the reader transmit and tag antennas.

3.4.2 Backscatter Performance: BPSK Radar Cross-Section

Bistatic readers use two separate "transmission" paths with losses L_{tx} and L_{rx}, that correspond to the incident and scattered waves. These have different antenna separations, r_{tx} and r_{rx}, different reader antennas with gain $G_{tx}(\theta_{tx}, \phi_{tx})$ and $G_{rx}(\theta_{rx}, \phi_{rx})$, different incident and scattered tag orientations, $(\theta_{ant,tx}, \phi_{ant,tx})$ and $(\theta_{ant,rx}, \phi_{ant,rx})$, and corresponding unit polarization vectors for each. Substituting the Friis equation with these parameters into (3.11) gives

$$\begin{aligned}\frac{P_{bs}}{P_{tx}}\frac{\eta_{tx}}{\eta_{rx}} = \frac{\eta_{mod}(\bar{p})}{L^2} = \eta_{mod}(\bar{p})\left(\frac{\lambda}{4\pi r}\right)^4 & G_{tx}(\theta_{tx}, \phi_{tx})G_3(\theta_{ant,tx}, \phi_{ant,tx})|\hat{\mathbf{u}}_{ant,tx} \cdot \hat{\mathbf{u}}_{tx}|^2 \cdot \\ & \times G_{rx}(\theta_{rx}, \phi_{rx})G_3(\theta_{ant,rx}, \phi_{ant,rx})|\hat{\mathbf{u}}_{ant,rx} \cdot \hat{\mathbf{u}}_{rx}|^2\end{aligned} \tag{3.16}$$

The author assures concerned members of the public that this thesis will not make a habit out unwieldy equations like this.

Like P_3 and G_3 in the forward link, the η_{mod} and G_3 terms are not suited for direct measurement once a tag is integrated. Just as we encapsulated terms into W_0 in the forward link, we can collect these terms together into bistatic BPSK radar cross-section,

$$\begin{aligned}\sigma_\Delta(\bar{p}, \theta_{ant,tx}, \phi_{ant,tx}, &\theta_{ant,rx}, \phi_{ant,rx}, \hat{\mathbf{u}}_{ant,rx}, \hat{\mathbf{u}}_{ant,rx}) \\ &= \frac{\lambda^2}{4\pi} G_3(\theta_{ant,tx}, \phi_{ant,tx}) G_3(\theta_{ant,rx}, \phi_{ant,rx}) |\hat{\mathbf{u}}_{ant,rx} \cdot \hat{\mathbf{u}}_{rx}|^2 \eta_{mod}(\bar{p}),\end{aligned} \tag{3.17}$$

following the original notation of [69]. This includes the effects of polarization mismatch specified only in the scattered (i.e., receive path) direction according to the definition of [98, p. 31]. This differs by the factor of 4 through our definition of η_{mod} in (3.9) compared to the quantity known as "differential radar cross-section (RCS)" [42, 99], "ΔRCS" [41, 44], "RCS" [10, p. 322] [43], or "echo area," [69].

Substituting σ_Δ into (3.16) gives the bistatic radar equation,

$$\frac{P_{bs}}{P_{tx}} \frac{\eta_{tx}}{\eta_{rx}} = G_{tx}(\theta_{tx}, \phi_{tx}) G_{rx}(\theta_{rx}, \phi_{rx}) \sigma_\Delta(\theta_3, \phi_3) \frac{\lambda^2}{(4\pi)^3 r_{tx}^2 r_{rx}^2} |\hat{\mathbf{u}}_{ant,tx} \cdot \hat{\mathbf{u}}_{tx}|^2. \tag{3.18}$$

Like the convention of (3.15), this includes only the polarization loss of the incident plane wave, to leave the RCS definition according to IEEE standard terminology.

The monostatic case is somewhat simpler, because there is only one path. There is therefore only one relavant reader antenna orientation $(\theta_{tx}, \phi_{tx}, \hat{\mathbf{u}}_{tx}) = (\theta_{rx}, \phi_{rx}, \hat{\mathbf{u}}_{rx})$, and one tag antenna orientation, $(\theta_{ant,tx}, \phi_{ant,tx}, \hat{\mathbf{u}}_{ant,tx}) = (\theta_{ant,rx}, \phi_{ant,rx}, \hat{\mathbf{u}}_{ant,rx}) = (\theta_3, \phi_3, \hat{\mathbf{u}}_3)$. Inserting the Friis equation into into L in (3.10) gives:

$$\frac{P_{bs}}{P_{tx}} = \frac{\eta_{mod}}{L^2} = \eta_{mod} \left[\left(\frac{\lambda}{4\pi r} \right)^2 G_{tx}(\theta_{tx}, \phi_{tx}) G_3(\theta_3, \phi_3) |\hat{\mathbf{u}}_3 \cdot \hat{\mathbf{u}}_{tx}|^2 \right]^2. \tag{3.19}$$

Substituting (3.21) back into (3.19) gives the monostatic radar equation,

$$\frac{P_{bs}}{P_{tx}} \frac{\eta_{tx}}{\eta_{rx}} = \frac{G_{tx}^2(\theta_{tx}, \phi_{tx}) \lambda^2 \sigma_\Delta(\theta_3, \phi_3)}{(4\pi)^3 r^4} |\hat{\mathbf{u}}_3 \cdot \hat{\mathbf{u}}_{tx}|^2, \tag{3.20}$$

with the monostatic BPSK radar cross section:

$$\sigma_\Delta(\bar{p}, \theta_3, \phi_3, \hat{\mathbf{u}}_{tx}, \hat{\mathbf{u}}_3) = \frac{\lambda^2}{4\pi} G_3(\theta_3, \phi_3)^2 |\hat{\mathbf{u}}_3 \cdot \hat{\mathbf{u}}_{tx}|^2 \eta_{mod}(\bar{p}). \tag{3.21}$$

3.4.3 Backscatter Performance: Carrier Radar Cross-Section

A central theme of Chapter 2 was that useful BPSK modulation received by the reader is independent of the received carrier wave, except for effects on matching (neglecting desensitization effects). Reflections

Reflection source	Typical leaked power (normalized to P_{tx})	Network parameter	Radar parameter
Reader antenna mismatch (monostatic operation)	-25 dB to -15 dB	E	N/A
Reader antenna leakage (bistatic operation)	-40 dB to -15 dB	E	N/A
Tag antenna structure	$\propto 1/r^4$ by (3.20),(3.18)	E	σ_{cw}
Tag antenna loads	$\propto 1/r^4$	$\lvert\tilde{\rho}_R + \tilde{\rho}_L\rvert/4$	σ_{cw}

Table 3.2: Sources of carrier leakage for systems operating in free space

from the tag antenna at the carrier frequency are therefore second-order effects in realistic operation, and sometimes negligible. This view is also supported by prior literature (e.g., [70]). Unfortunately, confusion about the effects of antenna scattering at the carrier has filled the literature with questionable design and measurement practices.

Potential sources of carrier reflections are listed in Table 3.2 (for the free-space domain in which the radar equation is valid). Each source is listed with the corresponding parameter that encapsulates it in the network model or the radar model.

A key difference between the representation of these reflections in the model is listed as from the antenna structure reflection, sometimes called "structural-mode" antenna reflections. This is reflection from the tag antenna structure caused by currents excited on the antenna that do not interact with the tag chip. In the network model, this is included as part of the environment, because it is between the reader antenna and tag antenna reference planes. In the radar model, which regards the antennas as black boxes interacting based on geometric position, this effect must be included in the RCS of the target, to preserve the free space assumptions around it.

One approach to analysis of loaded antennas is proposed in Green's 1963 thesis. He defines a power-wave reflection coefficient, A, that is the equivalent antenna load that would result in structural-mode reflections in a given orientation. It is related to the structural mode component of RCS at the carrier frequency, σ_s, through:

$$\begin{aligned}\sigma_s(\bar{p}, \theta_{ant,tx}, \phi_{ant,tx}, &\theta_{ant,rx}, \phi_{ant,rx}, \hat{\mathbf{u}}_{ant,rx}, \hat{\mathbf{u}}_{ant,rx}) \\ &= \frac{\lambda^2}{4\pi} G_3(\theta_{ant,tx}, \phi_{ant,tx}) G_3(\theta_{ant,rx}, \phi_{ant,rx}) |\hat{\mathbf{u}}_{ant,rx} \cdot \hat{\mathbf{u}}_{rx}|^2 \\ &\quad \times |A(\theta_{ant,tx}, \phi_{ant,tx}, \theta_{ant,rx}, \phi_{ant,rx}, \cdot\hat{\mathbf{u}}_{rx})|^2.\end{aligned} \tag{3.22}$$

Expressing the full orientation and gain dependences here has made it nearly unreadable, but underscores

Antenna type	$\|A\|$
Pyramidal standard gain horn (E-plane)	0.2
$\lambda/2$ dipole	1
$\lambda/2$ dipole ($\lambda/2$ behind a $\lambda \times \lambda$ PEC plate)	5

Table 3.3: Examples of co-polarized boresight $|A|$ (based on [96, pp. 103-104])

the complexity underlying the simplified free space equations. This is equation (44) in [69, p. 40] expanded into the more general bistatic case and adapted to fit the notation of this thesis. Structural-mode reflections (via A) have orientation dependence separate from antenna mode reflections (via G_3), so A depends on orientation separately from G_3.

A few examples of antennas and corresponding co-polarized broadside $|A|$ are listed in Table 3.3. The horn has the weakest structural-mode scattering component, so for large antenna load mismatch, the antenna mode scattering is likely to dominate. The value $A \approx 1$ is taken as almost axiomatic for a $\lambda/2$ dipole (but it is not exact). If a perfectly conducting $\lambda \times \lambda$ plate is placed behind this dipole, then by image theory the dipole gain doubles, and so the antenna-mode RCS quadruples. The sheet itself is a reflector, with an RCS component $\sigma_s = 4\pi\lambda^2$ in phase with that of the dipole. Solving for $|A|$ gives the indicated value; if the area of the sheet is increased toward infinity, $|A|$ approaches infinity at the same rate.

If the antenna load is fixed (not switching) but mismatched, there are both structural- and antenna-mode reflections corresponding to the power wave reflection coefficient of the load, $\tilde{\rho}$. The corresponding total antenna RCS, σ, is

$$\begin{aligned}\sigma(\bar{p}, \theta_{ant,tx}, \phi_{ant,tx}, &\theta_{ant,rx}, \phi_{ant,rx}, \hat{\mathbf{u}}_{ant,rx}, \hat{\mathbf{u}}_{ant,rx}) \\ &= \frac{\lambda^2}{4\pi} G_3(\theta_{ant,tx}, \phi_{ant,tx}) G_3(\theta_{ant,rx}, \phi_{ant,rx}) |\hat{\mathbf{u}}_{ant,rx} \cdot \hat{\mathbf{u}}_{rx}|^2 \\ &\quad \times |A(\theta_{ant,tx}, \phi_{ant,tx}, \theta_{ant,rx}, \phi_{ant,rx}, \cdot\hat{\mathbf{u}}_{rx}) - \tilde{\rho}|^2.\end{aligned} \tag{3.23}$$

Since $|A|$ can become very large but $|\tilde{\rho}| \leq 1$, it is often true that the structural-mode reflection component is larger than the antenna-mode component. This is particularly significant when mechanical mounts, non-radiating feed structures, or large reflectors are taken into account. An antenna for which $A = \tilde{\rho}$ in a desired direction is called a "minimum scattering" antenna, for $\sigma = 0$. This is often taken to be

a reasonable approximation for dipole-type tag antennas. Thus, there are no reflections for an antenna with $A = 1$ and a conjugate-matched load.

The parameter is referenced to the same phase and magnitude as the chip loading the antenna. By adding the "effective" carrier reflection coefficient in the tag, the bistatic RCS corresponding to the *total* reflected power at the carrier, σ_{cw}, is

$$\begin{aligned}\sigma_{cw}(\bar{p}, \theta_{ant,tx}, \phi_{ant,tx}, &\theta_{ant,rx}, \phi_{ant,rx}, \hat{\mathbf{u}}_{ant,rx}, \hat{\mathbf{u}}_{ant,rx}) \\ &= \frac{\lambda^2}{4\pi} G_3(\theta_{ant,tx}, \phi_{ant,tx}) G_3(\theta_{ant,rx}, \phi_{ant,rx}) |\hat{\mathbf{u}}_{ant,rx} \cdot \hat{\mathbf{u}}_{rx}|^2 \\ &\quad \times \left| A(\theta_{ant,tx}, \phi_{ant,tx}, \theta_{ant,rx}, \phi_{ant,rx}, \cdot\hat{\mathbf{u}}_{rx}) + \frac{\tilde{\rho}_R + \tilde{\rho}_L}{2} \right|^2 .\end{aligned} \tag{3.24}$$

Still, despite the efforts invested in this discussion, application of σ_{cw} and the radar equation to passive UHF RFID is not useful in far-field operation. First, determining A other than by assumption is difficult and complicated. Second, in far-field operation where tag responses are weakest, the effect of tag scattering on matching is likely to be negligible, so the result is of little value. Third, propagation reflections in industrial indoor environments are likely to be much larger than the reflection from the antenna, making it even more negligible.

3.4.4 Backscatter Performance: Other tag RCS models in the literature

The "useful" backscatter is now shown exhaustively to be contained in BPSK modulated sidebands, and characterized and applied in free space through σ_{Δ}. The interfering but much less significant tag carrier frequency reflections are established in σ_{cw}. Importantly, the structural scattering component *exclusively* affects the carrier frequency power through σ_{cw}.

In recent years, unfortunately, confused applications of older work [69, 100] have become increasingly common. The definition of σ_{Δ} in this work agrees with others in the literature [43, 69, 71, 77, 101], except the factor of 4 η_{mod} caused by our definition of BPSK modulation power.

Some previous work defines tag response RCS parameters which do include A, thus including the interfering carrier frequency signal as a part of the characterized tag response. Several works propose

the following model for differential RCS [78, 79, 102–104]:

$$\begin{aligned}\text{“Differential RCS”} =& \frac{\lambda^2}{4\pi} G_3(\theta_{ant,tx}, \phi_{ant,tx}) G_3(\theta_{ant,rx}, \phi_{ant,rx}) |\hat{\mathbf{u}}_{ant,rx} \cdot \hat{\mathbf{u}}_{rx}|^2 \\ & \times |A(\theta_{ant,tx}, \phi_{ant,tx}, \theta_{ant,rx}, \phi_{ant,rx}, \cdot\hat{\mathbf{u}}_{rx}) + \tilde{\rho}|^2.\end{aligned} \tag{3.25}$$

This is the same as the total *carrier frequency* RCS at fixed frequency of (3.23)! Reflected power represented by this RCS does not contain any communicated data, so it is difficult to understand how it could will be useful in predicting link performance.

In other recent work, [105] arrives at the differential RCS of [77], but unfortunately conflates this with the assumption that it is only valid for minimum scattering tag antennas. This leads to further confusion and the assertion that more generally differential RCS in general varies with A according to (3.25).

The notation “$\Delta\sigma$” is sometimes used (as in [41, 106]) instead of Δ_σ (as in [69]), causing more confusion. An early version of ISO test standard [41] and many authors [80, 81, 107–110] misunderstand the intent of this as subtraction between two real-valued power quantities. This causes the power envelope interference problems discussed in Section 2.3.5, where tag responses are invisible for certain reader-to-tag antenna separations.

The “alternate models” in these works form the basis for design practices that seek to optimize tag design by careful selection of A. Unfortunately, as this section has demonstrated, there is no effect of A on σ_Δ. Reflections caused by large A have only the second-order effect of changing the self-interfering leaked carrier and some mismatch for the modulation at the reader, but only if the tag antenna is very large or very close to the reader antenna.

3.5 A Tag Backscatter Metric for Arbitrary Propagation Loss

The free field expressions for P_3 and P_{bs} are simple only in the sense that they can be expressed as simple products of loss terms. Unfortunately, these terms beget a *huge* number of degrees of freedom: 9 degrees for transmission and monostatic backscatter, and 16 for bistatic backscatter (mostly from the number of combinations of different antenna orientations). Adding realistic fading effects like shadowing and

multipath into P_{bs} becomes cripplingly complicated, which may explain the lack of literature on the subject.

When the tag is fully passive, $\bar{p}$ is clearly defined, and forward link tests can give W_0 rapidly if a calibrated and adjustable field or plane wave source is available. There is a great deal of redundant information in the free-space tag link behavior in the forward link through (3.15) compared to the return link by (3.20) or (3.18): reader and antenna gains and orientations and r are shared.

The general link loss models of (3.3), (3.10), and (3.11) suggest that this extends quite generally. Bolomey *et al* [43, 111] were the first to write about reciprocity between the forward link and return links in arbitrary linear environments. This concept is powerful because it predicts tag backscatter behavior beyond the free space domain of the radar equation.

This section extends these ideas to form a compact tag backscatter metric. This parameter, minus discussion of linearity, matching, and the accompanying link arithmetic, was proposed in [112, 113] for application to sensing with the tag. It is a central point of this thesis.

3.5.1 Bistatic Case

The arbitrary link loss formulations of power transmission and backscattering in equations (3.3) and (3.11) are composed of the separate path losses L_{tx} and L_{rx}. Evaluating these losses at the turn-on threshold P_{tx0}, which is valid because from our assumption the environment (through our original S-parameter network E) has linear power response, gives

$$\frac{1}{L_{tx}L_{rx}} = \left(\frac{P_{L0}}{P_{tx0}}\bigg|_{\text{tx port}} \frac{1}{\eta_{L0}} \right) \left(\frac{P_{L0}}{P_{tx0}}\bigg|_{\text{rx port}} \frac{1}{\eta_{L0}} \right) = \frac{P_{bs}}{P_{tx}} \frac{1}{\eta_{mod}} \frac{\eta_{tx}}{\eta_{rx}}. \tag{3.26}$$

Notice that unlike the power harvesting term in the middle that is evaluated at tag turn-on, the backscatter expression on the right is left to be evaluated at arbitrary P_{tx}. Expressing the receive path loss L_{tx} in terms of turn-on levels and tag chip sensitivity means this expression involves the tag turn-on power that a reader must transmit to turn on the tag chip from its *receive* port, $P_{tx0}|_{\text{rx port}}$. This does not correspond to the power level the reader is actually transmitting from this receive port; like the transmit port turn-on level, $P_{tx0}|_{\text{tx port}}$, this only describes what *would* be required to turn on the tag.

The tag chip sensitivity and the corresponding match efficiency at turn-on are independent of the

source of the power, so this simplifies to

$$\frac{1}{L_{tx}L_{rx}} = \frac{P_{L0}^2}{(P_{tx0}|_{\text{tx port}})(P_{tx0}|_{\text{rx port}})}\frac{1}{\eta_{L0}^2} = \frac{P_{bs}}{P_{tx}}\frac{1}{\eta_{mod}}\frac{\eta_{tx}}{\eta_{rx}}. \tag{3.27}$$

Rearranging P_{tx} terms and substituting $P_{tx} = \bar{p}P_{tx0}$ leaves a figure of merit, referred to in this work as B for "backscatter:"

$$\begin{aligned} B(f, \bar{p}, Z_3(nf), \text{ reader command}) &= P_{tx0}|_{\text{rx port}} P_{bs}\frac{\eta_{rx}}{\eta_{tx}} \\ &= \bar{p}\left(\frac{P_{L0}}{\eta_{L0}}\right)^2 \eta_{mod}. \end{aligned} \tag{3.28}$$

This is a central focus of this thesis. B is fixed *exclusively* by circuit parameters inside the tag, so it depends *exclusively* upon the same parameters as the tag circuit efficiencies $\eta_{mod}(\bar{p})$ and η_{L0}, mainly the four listed variables (at fixed temperature and pressure). Importantly, this means it is entirely independent of the propagation environment except through detuning of the tag antenna $Z_3(nf)$ (and potentially other non-electrical effects like temperature and pressure). Taking the tagged object as the dominant environmental effect on $Z_3(nf)$, B can be considered a parameter of a "tagged object."

3.5.2 Monostatic Case

Analysis with monostatic backscatter detection proceeds in similar fashion, but with only the shared transmit and receive signal path loss L. Just like the bistatic case, combining (3.3) at the tag turn-on power level and (3.11) gives:

$$\frac{1}{L^2} = \left(\frac{P_{L0}}{P_{tx0}}\frac{1}{\eta_{L0}}\right)^2 = \frac{P_{bs}}{P_{tx}}\frac{1}{\eta_{mod}}\frac{\eta_{tx}}{\eta_{rx}}. \tag{3.29}$$

This gives B as the exact same equation as (3.28), except that $P_{tx0}|_{\text{rx port}} = P_{tx0}|_{\text{tx port}}$.

3.5.3 Model Limitations from Underlying Assumptions

Recalling the underlying assumptions in the thesis so far, B by equation (3.28) is exact under the following conditions:

(1) Backscatter modulation received by the reader has well-defined digital states (weak distortion).

(2) Propagation loss between reader and tag antennas is linear and causal with respect to power.

(3) The tag backscatter modulation is encoded as described in Chapter 2.

(4) Tag turn-on is abrupt and repeatable for $P_{tx} \geq P_{tx0}$ (which has been verified to within 0.2 dB for many tags).

These assumptions are implicit in all analysis for the remainder of this thesis. These are a subset of the assumptions required to use the radar equation. Item (4) is particularly important, because it limits both σ_Δ and B to use with *fully passive* tags unless an alternate operating point can be defined besides $\bar{p}$.

3.6 Comparison of Tag Backscatter Metrics

The free space parameters are simple applications of well-understood microwave theory. This section poses them against B to shed some light on the much less well understood parameter.

It is important to understand that B and σ_Δ are drastically different metrics. Like σ_Δ, larger values of B suggest larger received P_{bs}. However, while σ_Δ characterizes a tag in complete isolation, B describes the tag under the condition that the environment allows turn-on. This is why B depends on P_{L0} and η_{L0} — they limit the maximum forward-link loss and therefore the maximum monostatic backscatter loss.

One interpretation of B is as a balance between forward and return links. Increasing transmission loss requires greater P_{tx0} Because the loss is reciprocal, P_{bs} falls. The theory culminating in equation (3.28) simply says that nature forces these trends in P_{tx0} and P_{bs} to be proportionally inverse. This is itself a very different concept than the proportional power loss when using σ_Δ with the radar equation.

Combining the forward and reverse link models of (3.14) and (3.17) with $W = \bar{p}W_0$ relates σ_Δ and W_0 to B,

$$B = P_{bs}P_{tx0}\eta_{tx}\eta_{rx} = \bar{p}\left(\frac{\lambda^2}{4\pi}\right)W_0^2\sigma_\Delta. \tag{3.30}$$

As expected, there is no dependence on reader or tag antenna position or orientation, which determine L in free space. Substituting (3.14) and (3.17) for W_0 and σ_Δ causes G terms to cancel so that the expression simplifies to (3.28).

Equation (3.30) allows any one of B, W_0, or σ_Δ to be computed from the other two. As a side benefit, a B computed from free-space measurements of W_0 and σ_Δ generalizes to more arbitrary environments.

The two backscatter metrics differ in measurability. Chapter 4 will discuss calibration including measurement of σ_Δ, but in short it requires either an anechoic test environment with a well-calibrated interrogation antenna, or tightly controlled field generation in an environment like a gigahertz TEM cell. Chapter 5 studies measurement of B, and finds that a testbed only requires a well-matched antenna and a well-calibrated signal generator and measurements.

3.7 Application to Bounding Monostatic Backscatter Power

The link balance imposed by B leads to its simplest and most powerful application to link analysis: the weakest backscattered power a monostatic reader can receive from a tag that is "on." Since B increases with $\bar{p}$ above turn-on, the minimum non-zero backscattered power occurs at $\bar{p} = 0$ dB. The corresponding minimum bound to backscattered power is

$$\min[P_{bs}]\ (\text{dBm}) = \ [B|_{\bar{p}=0\,\text{dB}}\ (\text{dBm})^2] - [P_{tx}\ (\text{dBm})]. \tag{3.31}$$

Here, "$(\text{dBm})^2$" is "dB relative to one square milliwatt,"

$$B\,(\text{dBm})^2 = 10\log_{10}\frac{B\,(\text{mW})^2}{1\,(\text{mW})^2}. \tag{3.32}$$

Use of this unit is nonstandard, but allows $\min[P_{bs}]$ to be determined from B data "by inspection" with the simple subtraction given by (3.31).

Because they are proportional, trends in B at turn-on are the same for $\min[P_{bs}]$ through (3.31). For example, detuning that reduces B reduces $\min[P_{bs}]$ by the same amount. Likewise, measurement uncertainty in B contributes the same uncertainty toward $\min[P_{bs}]$.

As a result, $\min[P_{bs}]$ of an assembled tag varies only with tag antenna tuning, frequency, and whether the tag reads or writes. A link margin may be subtracted from estimates of $\min[P_{bs}]$ when specifying reader sensitivity to account for detuning effects.

3.8 Summary

High-level analysis of the benefits and risks in use of RFID requires an understanding of what is possible within the bounds of physics, standards, and emission regulations. Fundamental power parameters and relationships defined in Chapter 2 enable informed discussion of device characterization and system behavior in free space, and recent movement toward more general analysis based on network theory. The alternative suggested in this chapter, B, is a more compact backscattered power characterization than radar cross-section for passive systems. With this metric, system designers can find a deterministic minimum bound to backscatter received from any passive tag under realistic fading conditions with a trivial computation.

The material in this chapter originated in the following peer-reviewed publications by the author:

D.G. Kuester, D.R. Novotny, J.R. Guerrieri, Z. Popović, "Simple Test and Modeling of RFID Tag Backscatter," *IEEE Trans. on Microwave Theory and Techn.*, vol. 60, no. 7, July 2012, pp. 2248-2258

D.G. Kuester, D.R. Novotny, J.R. Guerrieri, "Forward and Reverse Link Constraints in UHF RFID with Passive Tags," *Proc. 2010 IEEE Intl. Symp. on Electromagnetic Compatibility*, pp. 680-685.

Chapter 4

Binary-Modulated Backscatter Signal Detection and Power Calibration

Wenn du denkst, daß das Publikum sich langweilt,
dann spiele langsamer, nicht schneller.
If you think that the audience is bored, then play slower, not faster.

credited to Gustav Mahler (1860-1911)

Measurements of either σ_{Δ} or B require detection and calibration of backscattered BPSK. Except for measurements that use calibration targets similar to the 2006 version of ISO 18047-6, this requires accurate measurements of BPSK power. Signal analyzers do not provide uncertainty lower than about 1 dB.

Costs add to significant disincentives to perform these tests. There is a significant initial investment in instruments — a network analyzer with calibration standards, a signal analyzer, a stable and linear transmitter (and possibly an amplifier) — and an expensive anechoic environment that is likely to occupy at least 12-16 m^2 of floor space. Current test methods require significant time and attention from a human operator who is likely to expect to be paid wages. The instruments alone may easily cost six orders of magnitude more than the typical bulk price of an inexpensive tag.

This chapter focuses on measurement of backscattered BPSK power. This is achieved by generating over-the-air or circuit-based calibration backscatter signals. After some practical discussion of RFID tag backscatter measurement detection, the chapter gives analysis of the uncertainty of B measurements. These serve the broader goal of supporting accurate tests of tag backscatter via B or σ_{Δ}.

4.1 Reference Backscatter Power for Tag Calibration

Tests for σ_{Δ} in both the 2006 and 2011 versions of standard ISO 18047-6 require measurement of P_{bs}, but do not address calibrating measurements to make them traceable to fundamental RF power standards. The broader technical literature has not addressed this problem either. Further, measurement of the figure of merit B — addressed in Chapter 5 — also requires measurement of P_{bs}. Thus, the author felt it important to give effort to calibrate measurements of backscattered power.

Communication signal analyzers are capable of demodulating vector inputs with extremely low *relative fidelity* (very little error from nonlinear effects), but the absolute uncertainty of these measurements is greater than 1 dB. The relative measurement accuracy is quite good within the measurement dynamic range, so a reference backscatter signal with fixed and known P_{bs}/P_{tx} is adequate to calibrate DUT backscatter.

The theory developed in Chapters 2 and 3 suggests that a carefully characterized source of reference modulation with a known modulation efficiency η_{mod} and and link losses (through known $|S_{31}|$ and $|S_{23}|$) are sufficient to predict the backscattered reference power. This section introduces devices that can be characterized to serve this purpose, and how they can be validated as an accurate reference for calibrating tag backscatter.

4.1.1 Reference Backscatter at Coaxial Reader Ports

Interfaces in our coaxial test circuits are connectors that are well-defined network interfaces and are usually well matched to 50 Ω.

Inserting back into (4.1), monostatic BPSK modulation power absorbed by the interrogator at port 1

is

$$\frac{P_{bs}}{P_{tx}} = \left|\frac{\Delta\rho_1}{2}\right|^2 \left|\frac{1-|\rho_{I1}|^2}{(1-\rho_G\overline{\rho}_1)^2 - \left(\rho_{I1}\dfrac{\Delta\rho_1}{2}\right)^2}\right|^2 \tag{4.1}$$

for monostatic backscatter detection.

Thus, to first order, the backscattered power is proportional to $|\Delta\rho_1|^2$. Choosing calibration circuit parameters to simplify the preceding equations greatly simplifies the analysis: $Z_0 = 50\,\Omega$, $|S_{11}| < 0.1$, $|S_{22}| < 0.1$, $|S_{21}| < 0.1$, $S_{21} = S_{12}$, and passive ρ_L ($|\overline{\rho}_L| \leq 1, |\Delta\rho_L| \leq 2$). These result in loose but absolute bounds $|\overline{\rho}_1| < 0.12|$ and $|\Delta\rho_1| < 0.03$.

In this case, combining equations (4.1) and (2.6) simplify to:

$$\frac{P_{bs}}{P_{tx}} \approx |\Delta\rho_L|^2|S_{31}|^4 \left|\frac{1-|\rho_I|^2}{(1-S_{33}\overline{\rho}_L)^2(1-\rho_{I1}S_{11})^2}\right|^2. \tag{4.2}$$

If S_{11} and S_{22} are exceptionally small, or the reader is well matched so $\rho_G \approx 0$, the matching factor on the right may even disappear. Readers often use unusual low-cost RF connectors that cannot be attached directly test instruments, so ρ_G is difficult to measure repeatably and the term on the right should be viewed as an "error" term.

Under the same conditions, the bistatic backscatter simplifies similarly:

$$\frac{P_{bs}}{P_{tx}} \approx |\Delta\rho_L|^2|S_{31}|^2|S_{23}|^2 \left|\frac{1-|\rho_I|^2}{(1-S_{33}\overline{\rho}_L)^2(1-\rho_{I1}S_{11})^2(1-\rho_{I2}S_{22})^2}\right|^2. \tag{4.3}$$

4.1.2 Reference Backscatter Over the Air

This was the author's first approach, imitating tag operation presented to an interrogation antenna in the test zone. The resulting test is more complicated and therefore prone to operator error than generating it through a coupler as described in the next section. The author therefore does not recommend the over-the-air method, but it is offered here for completeness.

The modulator shown in Fig. 4.1 realizes the model in Fig. 3.1. The switch has a nominal 20 ns rise/fall time to within 10% of steady state, which is fast enough to emulate the maximum 640 kHz symbol rate by tags compliant with ISO/IEC 18000-6C. The modulator is placed in the test zone as illustrated by Fig. 4.2.

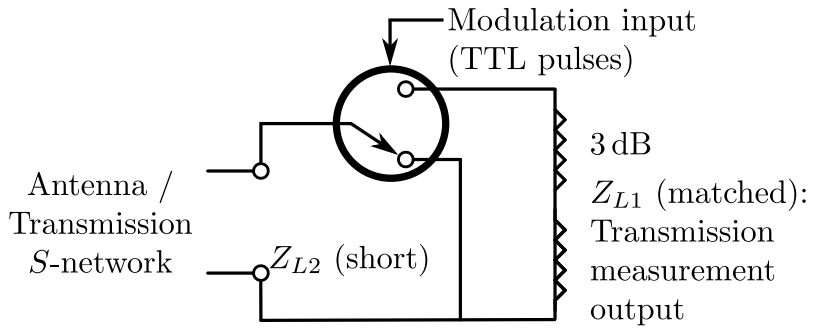

(a)

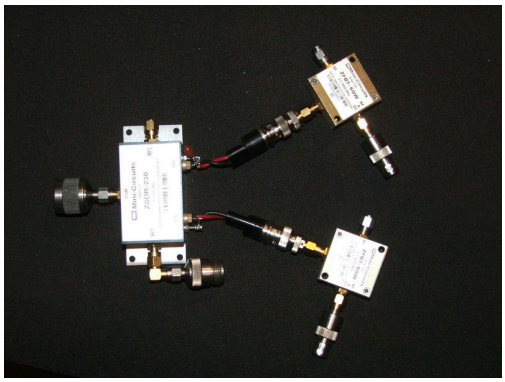

(b)

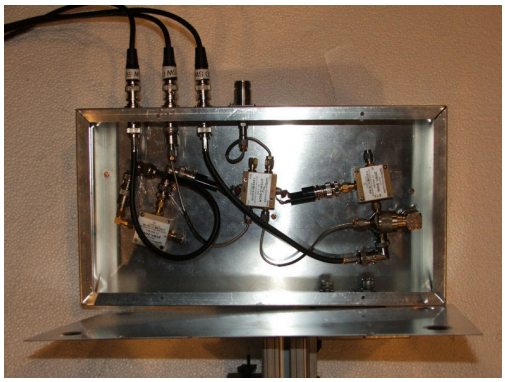

(c)

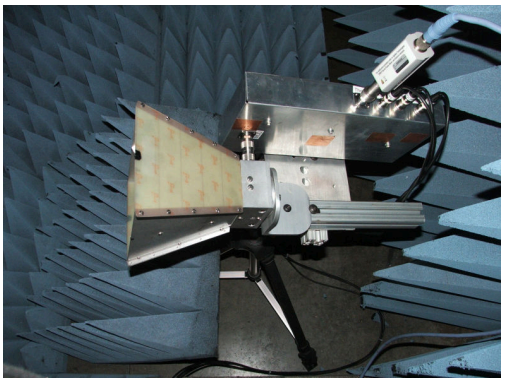

(d)

Figure 4.1: Simple reference modulation circuit shown as a simplified schematic (a), with direct realization (b), enclosure in a rugged shielded box (c), and integrated with a horn antenna (d). The load Z_{L1} is intended to connect with a matched $50\,\Omega$ instrument such as a power sensor or network analyzer, to measure power delivered to the backscatter reference and serve as a matched reflection state for modulation. The device is mounted in a 33 cm $\times$ 18 cm $\times$ 5 cm shielded box with ± 5 V DC biasing inputs, and bias tees to improve DC to RF isolation.

Table 4.1: Modulator components

Block	Component
Antenna	Roberts dipole tuned to 10 MHz
	Nominal gain ..... 2.2 dBi
	Minimum return loss[1] ..... 10 dB
Switch	Lab switch, 0-5 GHz
	Nominal 1 dB compression ..... 20 dBm
	Nominal insertion loss[1] ..... 1.7-2.5 dB
	Nominal switching time[2] ..... 20 ns
	Control interface ..... 5 V TTL
ASK Loads	Z_{L1}: Network analyzer or power meter (50 Ω)
	Z_{L2}: SMA short

[1] Across 860-960 MHz [2] To within 10% of steady state output

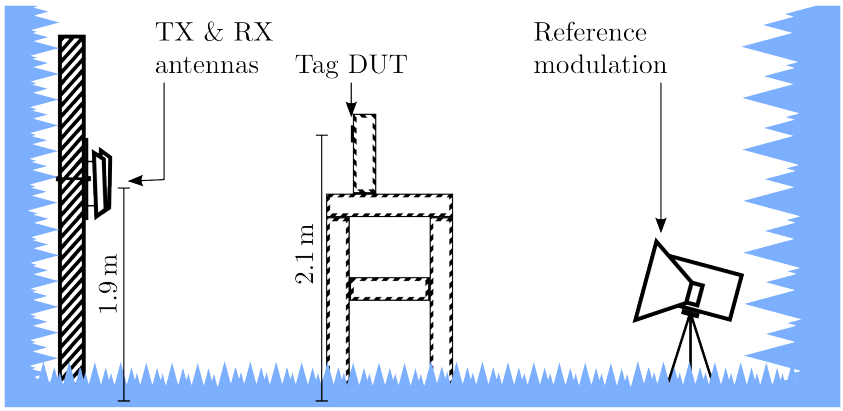

(a)

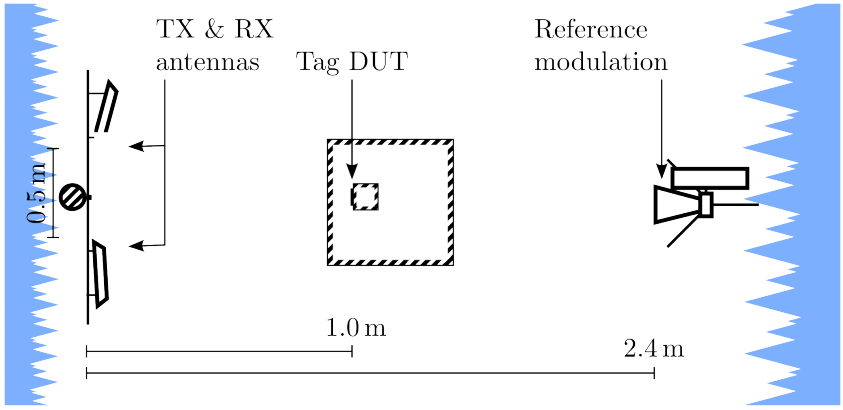

(b)

Figure 4.2: Layout of the testbed antennas, DUT tag, and reference backscatter in the test zone for over-the-air reference backscatter. Shapes with hashed edges represent styrofoam structures.

A standard gain horn with a measured gain of 6.69 dBi at 1 GHz is the reference backscattering antenna. It has return loss greater than 10 dB across 860-960 MHz, corresponding to $|S_{33}|$.

Instruments with 50 Ω input impedance serve both as a matched load modulation state (with $|\rho_{L2}| \approx 0$), and to allow measurements of interrogation signal link losses. A network analyzer makes a convenient matched load for characterizing the device, and a power meter is subsequently used to measure received interrogation power. An additional 3 dB pad between the switch output and the matched load attenuates reflections between the horn and the instrument. The other switch load is a short, for $|\rho_{L1}| \approx 1$, though the actual $|\rho_{L1}|$ is approximately 2 dB smaller because of switch insertion loss.

With $|\rho_{L2} - \rho_{L1}| \approx 1$, and the backscatter antenna approximately matched for small $|S_{33}|$, the anticipated η_{mod} is near 0 dB.

Measuring Modulation Efficiency

Modulation efficiency of a reference backscatter device must be measured accurately to be suitable for calibrations. Either of (2.2) and (2.6) with (3.9) allow a choice between two sets of parameters to relate measured monostatic backscatter with a network analyzer in each modulation state:

$$\begin{aligned} \eta_{mod} &= \left(\frac{1 - |\rho_3|^2}{|1 - \rho_3 \rho_{L1}||1 - \rho_3 \rho_{L2}|} \right)^2 |\rho_{L2} - \rho_{L1}|^2 \\ &= |\Delta\rho_1|^2 \frac{(1 - |\rho_3|^2)^2}{|S_{31}|^2 |S_{23}|^2}. \end{aligned} \tag{4.4}$$

Thus, we can determine η_{mod} by "wireless" measurements of $\Delta\rho_1^2$ and measurements of S, or more directly by reflection coefficient measurements of ρ_{L2}, ρ_{L1}, and ρ_3. In either case, the modulation state of the modulator is fixed with a DC voltage supply during measurement.

An advantage of calibrating η_{mod} from measurements of ρ_{L2}, ρ_{L1}, and S_{33} directly is that (to first order) measurement dynamic range is not reduced by moving the reference backscatter antenna in an anechoic test environment. Further, ρ_{L2} and ρ_{L1} can be measured with phase-stable cables near the network analyzer more accurately than with the long cables that are necessary to measure reflection coefficients of objects inside the test chamber.

Calibrating η_{mod} from $\Delta\tau$ and measurements of propagation losses S_{23} and S_{31} has different advantages. Transmission measurements of propagation losses can have smaller uncertainties than the

reflection measurements in the first approach, but any motion in the long cables may introduce additional phase errors. This calibration also needs fewer measurements, which may reduce the contribution of operator mistakes to measurement error.

Detailed quantitative comparison of uncertainties in these approaches will be left for future work. The following subsection will validate that either set of measurements can produce a valid characterization of η_{mod}.

Validation Tests

The model in equations (2.2) and (2.6) gives two expressions for η_{mod} in terms measurable network parameters, so η_{mod} can be validated by measuring the parameters for each with a network analyzer and comparing the results.

The validation tests were performed in monostatic use. The transmit and receive antenna is a commercial RFID patch with at least 10 dB return loss across 895-940 MHz. The change in reflection coefficient $\Delta\rho$ into the antenna was taken to be equivalent to $\Delta\tau$, with the simplification $S_{23} = S_{13}$. The anechoic environment reduces interference from outside signals, but the calibration for backscattered signal levels applies in other, more reflective environments too, if interference is below a tolerable level.

Results are shown in Fig. 4.4. Across the 860-960 MHz tag response bandwidth, the two measurements of η_{mod} agree within 0.1 dB. Below 860 MHz, detection antenna mismatch introduces additional noise in transmission measurements of S_{31} and $\Delta\rho$, because received signals are weaker.

Calibrating DUT Power

During tag measurements, it is impractical to measure transmission coefficients $|S_{31}|^2 = |S_{13}|^2$ and $|S_{23}|^2 = |S_{32}|^2$ with a network analyzer. Instead, we use power sensors to measure (1) transmitted interrogation power P_{tx} available to port 1 or 2 with a coupler, and (2) power received at the output of the modulator switch, $P_3^{(ref)}$. In this paper, transmit, received, and backscattered power from interrogation into port n are represented as $P_{tx,n}$, $P_{ant,n}$, and $P_{bs,n}$. Assuming the network analyzer and power

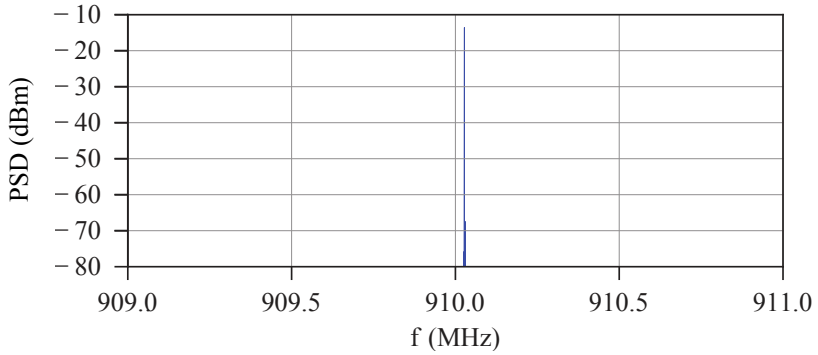

(a)

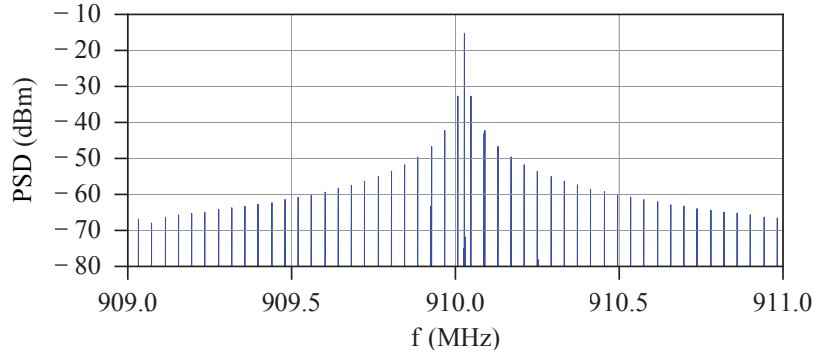

(b)

Figure 4.3: Spectrum analyzer traces of (a) unmodulated carrier leakage into the receive antenna, then (b) load-modulated at 20 kHz with the device in Fig. 4.1. In both cases, the signal generator transmitted the carrier at 12.1 dBm to the modulator antenna, placed boresight approximately 50 cm from a pair of transmit and receive antennas with 8 ± 1 dBi gain.

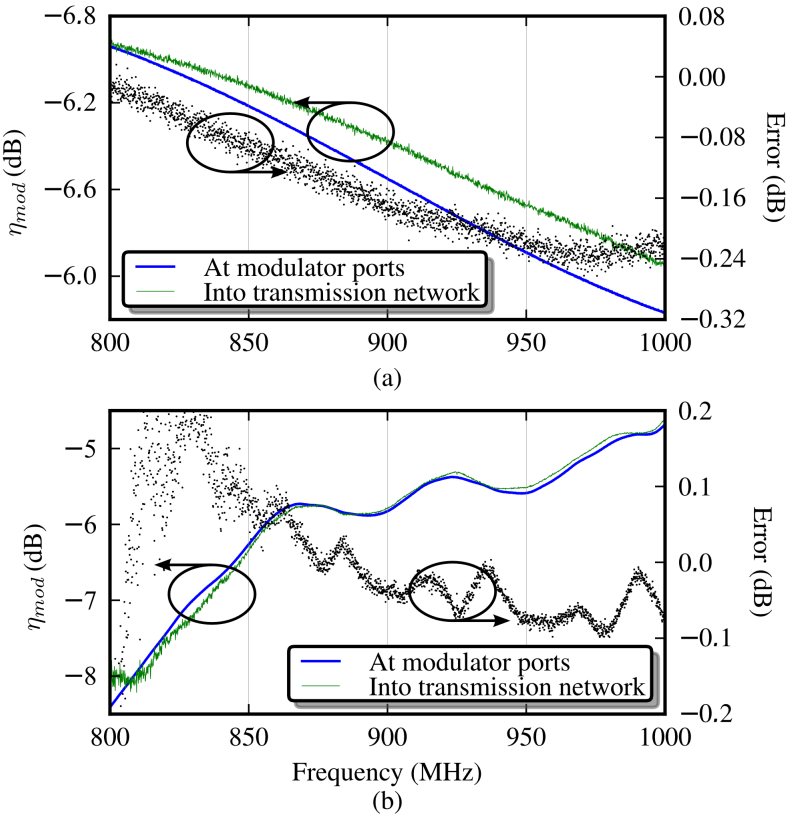

Figure 4.4: Validation of the reference backscatter with a network analyzer in a semi-anechoic test environment, computed with measurements of the network coefficients in (2.6). The curves agree to ± 0.1 dB over the 860-960 MHz tag response bandwidth.

sensors are similarly well-matched, power measurements and transmission losses are related with

$$|S_{31}|^2 = |S_{13}|^2 = \frac{P_{ant,1}^{(ref)}}{P_{tx,1}} \tag{4.5}$$

and

$$|S_{32}|^2 = |S_{23}|^2 = \frac{P_{ant,2}^{(ref)}}{P_{tx,2}}. \tag{4.6}$$

$P_3/P_{tx,1}$ and $P_3/P_{ant,2}$ are taken as $|S_{32}|^2$ and $|S_{31}|^2$. Both sensors are configured to measure average power during the period after the tag reply while the interrogation power is left on. This period was set to 1 ms, which is longer than that of typically deployed readers to reduce noise by averaging.

Loss in the switch reduces the measured power compared to the available $P_3^{(ref)}$ out of the backscattering antenna. To "back out" $P_3^{(ref)}$, the full two-port scattering parameters of the switch are used to de-embed the power available out of port 3 with transfer (T-) parameters.

Applying the Calibration

Assuming bandwidth of all backscattered signals are narrow about the interrogating carrier, and that cable and antenna mismatch and losses are linear with power, the fractional power lost will be the same for both a tag and reference backscatter:

$$\frac{P_{bs}^{(ref,meas)}}{P_{bs}^{(ref)}} = \frac{P_{bs}^{(tag,meas)}}{P_{bs}^{(tag)}}. \tag{4.7}$$

This can be rearranged to find "true" backscattered power received from the tag,

$$P_{bs}^{(tag)} = \frac{P_{bs}^{(tag,meas)}}{P_{bs}^{(ref,meas)}} P_{bs}^{(ref)}. \tag{4.8}$$

Equations (4.3), (4.5), and (4.6) can be substituted for $P_{bs}^{(ref)}$, so for interrogation through port 1,

$$P_{bs,1}^{(tag)} = \frac{P_{bs,1}^{(tag,meas)}}{P_{bs,1}^{(ref,meas)}} \frac{P_{ant,2}^{(ref)}}{P_{tx,2}} P_{ant,1}^{(ref)} |\eta_{mod}^{(ref)}|^2. \tag{4.9}$$

or through port 2,

$$P_{bs,2}^{(tag)} = \frac{P_{bs,2}^{(tag,meas)}}{P_{bs,2}^{(ref,meas)}} \frac{P_{ant,1}^{(ref)}}{P_{tx,1}} P_{ant,2}^{(ref)} |\eta_{mod}^{(ref)}|^2. \tag{4.10}$$

The power is calibrated at the input to the coupler. Effects of mismatch or cable losses between the receive antenna and the measurement instrument are removed in the calibration process.

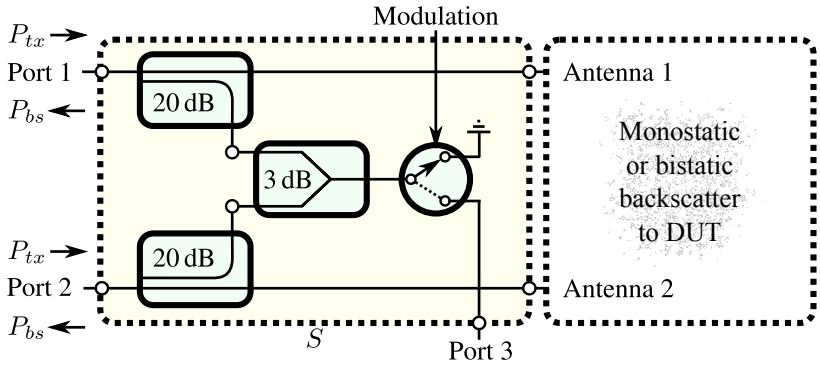

Figure 4.5: Calibration circuit for measuring P_{tx} and generating reference backscatter to calibrate monostatic or bistatic P_{bs} from a DUT in the propagation environment. Both P_{tx} and P_{bs} are referenced to the coupler input at either of ports 1 and 2. One-way loss through the coupler between port 1 or 2 and the antenna is less then 1 dB.

4.1.3 Reference Modulation Through a Coupler

Coupling power through a coaxial coupler instead of over the air with antennas turns out to give P_{bs} and P_{tx} much more simply than over the air. This way, we only need one power measurement: a single power sensor provides the same information given to us by two sensors in over-the-air tests.

A two-coupler test circuit, illustrated in Fig. 4.5, can measure transmit power P_{tx} available into either port 1 or 2, and reflects reference backscatter back to both ports 1 and 2 to support either monostatic or bistatic operation. Transmit power P_{tx} into either port is measured by directional coupler in the usual way. All ports of S and the power sensor are matched to greater than 30 dB return loss across 860-960 MHz, so mismatch effects can be ignored here with minimal loss. The coupling factors $C_1 = -20\log_{10}|S_{31}|$ and $C_2 = -20\log_{10}|S_{32}|$ are measured by network analyzer. The power meter reading P_{ref} then gives transmit power as

$$P_{tx}\ (\text{dBm}) = P_{ref}\ (\text{dBm}) + C_{1,2}, \tag{4.11}$$

inserting the relevant coupling factor for $C_{1,2}$. Measurement at device under test (DUT) turn-on gives P_{tx0}.

Reference backscatter is achieved by modulating the solid state switch in S with a pulse generator set to the DUT base link frequency (BLF). It modulates after each DUT response until the interrogator stops emitting a CW tone. Sidebands about a carrier input into port 1 or 2 are reflected back into both

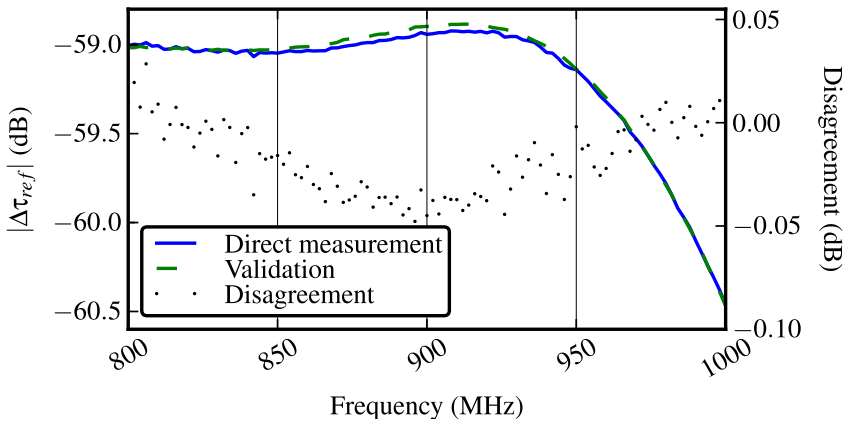

Figure 4.6: Network analyzer calibration measurement of the change in transmission coefficient $\Delta\tau_{21}$ between ports 1 and 2 of the reference load modulation device of Fig. 4.5. Antenna ports and port 3 are terminated by matched loads. The "validation" curve is computed from measurements of each term of (2.6), with separate incident and return transmission coefficients, and the "direct" measurement is simply vector subtraction of measured τ_{21} in each switch state.

input ports, enabling monostatic or bistatic use.

In selecting couplers for this application, the choice of $C_{1,2}$ affects only dynamic range; the balance between them is not important. High directivity is significant to minimize errors in P_{tx} (as in any coupled power measurement). These errors are within ± 0.06 dB, determined after sweeping phase shift on a $|\rho| = -10$ dB coupler load.

We perform bistatic calibration by measuring $\Delta\tau_{ref}$ between the coupler inputs with a network analyzer, at the reference plane in Fig. 4.5. The reference switching state is set with a DC voltage supply. We validate results by computing $\Delta\tau_{ref}$ from measured parameters on the right side of (2.6), shown in Fig. 4.6. Results agree to within 0.06 dB. We estimate the total uncertainty of $|\Delta\tau_{ref}|$ at 0.25 dB based on analysis of manufacturer specifications.

Reference backscattered power, including $\eta_{tx,rx}$, is

$$P_{bs,ref}\eta_{tx}\eta_{rx}\ (\text{dBm}) = [P_{tx}\ (\text{dBm})] + 10\log_{10}\frac{|\Delta\tau_{ref}|^2}{4} \tag{4.12}$$

with P_{tx} calibrated from (4.11).

Reference and DUT backscatter have narrow bandwidth about the same carrier, so linear, frequency-dependent losses are assumed to be the same for each. A calibration factor K encapsulating these effects

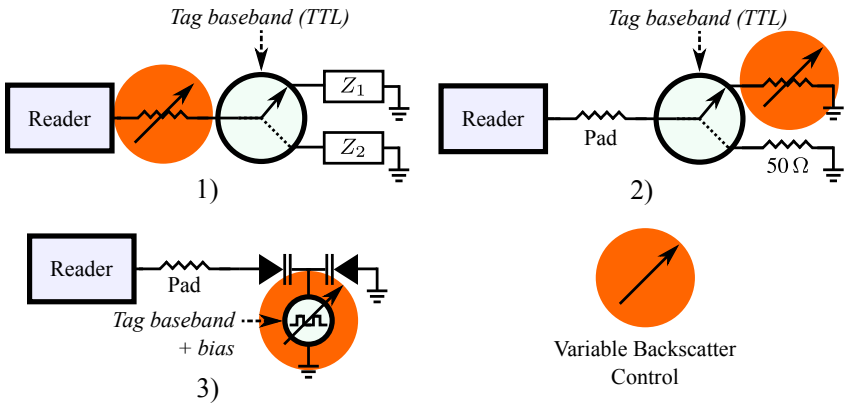

Figure 4.7: Potential test circuit topologies for adjusting reference backscatter signals. The control point for varying the backscatter is marked with the orange circle.

can be determined from ΔV_{ref},

$$K\,(\text{dB}) = 20\log_{10}|\Delta V_{ref}| - [P_{bs,ref}\eta_{tx}\eta_{rx}\,(\text{dBm})]. \tag{4.13}$$

Backscattered power from the DUT, P_{bs}, is then

$$P_{bs}\eta_{tx/rx} = 20\log_{10}|\Delta V_{dut}| + [K\,(\text{dB})]. \tag{4.14}$$

4.2 Reference Backscatter Power for Reader Tests

The same principles apply to backscatter power calibrations for reader tests as for tag tests. Reader receiver performance tests, however, require the ability to vary the reference backscatter power and still "know" P_{bs}.

4.2.1 Approaches to Varying Backscatter

We considered several approaches to controlling P_{bs} while maintaining a match to 50 Ω, illustrated in Fig. 4.7:

1) Tuning by Transmission Attenuation

For fixed P_{tx} and linear S, backscattered power can be tuned by adjusting either $|S_{31}|^2 = |S_{13}^2|$ or the switched load. For this work, the reference modulation device is fixed to $S_{22} = \rho_2$, so that a single $\Delta\rho_1$

calibration can be used independent of the generator loading. With well-matched lab components, this can be achieved to within 0.04 dB by maintaining either attenuation or coupling factor above 20 dB via S_{21}.

2) Tuning by Load Attenuation

An alternative is to load a switch with two identical shorted adjustable attenuators. Asymmetrically adjusting the attenuators then tunes $\rho_R - \rho_L$. In practice, however, this topology makes tuning difficult for small $\rho_R - \rho_L$ because of slight imbalance between the two signal paths through the switch and attenuators. We succeeded at only approximately 30 dB of monotonically decreasing $|\rho_R - \rho_L|$ tuning range with increasing difference in attenuation in this topology. This may be adequate for some applications, As a result, we chose not to use this topology, but it may be adequate in some applications.

3) Tuning by Variable Load Modulation

If ρ_R and ρ_L are achieved by adjusting bias on the same diode or transistor, P_{bs} can be tuned by adjusting the bias voltages of each state. In this topology, attenuation via S_{21} can be left constant, but should still be at least 20 dB to minimize loading effects onto the modulator by the reader.

This method can be realized in a compact circuit, but for FET devices $\rho_L(t)$ will be nonlinear with the modulation control voltage, and is only a "linear" reflection in the small signal input regime FET. This operating region can be maximized by maximizing the bias voltages.

4.2.2 Realized Circuit and Calibration Procedure

The test setup is illustrated by Fig. 4.8, employing the topology 1) of Fig. 4.7. In addition to the reader DUT, calibration circuit, and test instruments, there is a tag emulator which outputs baseband modulation responses to the DUT. Power out of the coupled arm of the directional coupler is split by a Wilkinson divider between the transmit power sensor and the tag emulator input. The coupler has more than 30 dB of return loss at each port, and the switch has more than 25 dB of return loss at each port.

The initial calibration is performed at the center frequency of the reader (i.e., 915 MHz in the US):

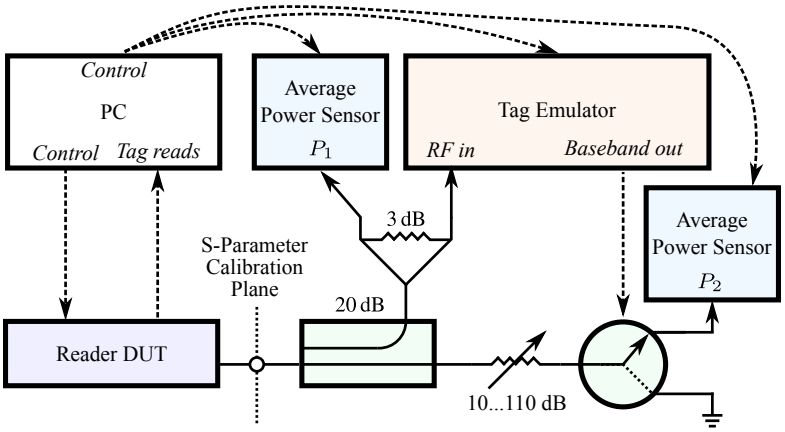

Figure 4.8: Test setup for measuring reader sensitivity, based on circuit 1) of Fig. 4.7. Adjusting the attenuator varies the backscattered power received by the reader from the tag emulator. Each device is coaxial and matched to 50 Ω with at least 20 dB of return loss.

(1) The attenuator in the testbed is set to its lowest value, 10 dB, to maximize measurement dynamic range.

(2) The power loss $K_{tx} = P_{tx}\,(\text{dBm}) - P_1\,(\text{dBm})$ is measured with a network analyzer across the reader transmit band.

(3) $|\Delta\rho_1^{(cal)}|^2$ is measured with a network analyzer at the center frequency of the reader.

(4) A matched signal generator is attached to port 1, and measurements are performed at each power sensor giving $P_1^{(cal)}$ and $P_2^{(cal)}$.

Transmit power available from the reader is then determined the usual way as $P_{tx}\,(\text{dBm}) = P_1\,(\text{dBm}) - K_{tx} - 10\log_{10}(1-|\rho_G|^2)$, where the coupling loss $C_1 > 0$ (in dB) is measured with a network analyzer between the coupler input and P_1 measurement plane.

This modulator has already been validated as linear with power in [71], so we assume it has some unknown efficiency η_{mod} that varies only with frequency. Further, the well-matched switch has some unknown attenuation loss, L in dB, such that

$$P_2\,(\text{dBm}) - P_{tx}\,(\text{dBm}) = 20\log_{10}|S_{31}| - L. \tag{4.15}$$

With (4.2), we can define a backscatter calibration factor,

$$\begin{aligned} K_{bs} &= 20\log_{10}|\Delta\rho_1^{(cal)}| + 2[P_1^{(cal)}\,(\text{dBm}) - P_2^{(cal)}\,(\text{dBm})] \\ &= 20\log_{10}|S_{31}^{(cal)}| + 2(K_{tx} + L), \end{aligned} \tag{4.16}$$

encapsulating the unknown terms.

During tests of a reader DUT with known reflection coefficient ρ_G, calibration terms K_{tx} and K_{bs} and measured P_1 and P_2 give P_{tx} and P_{bs} as

$$\begin{aligned} P_{tx} &= P_1\,(\text{dBm}) + K_{tx} \\ P_{bs} &= 2[P_2\,(\text{dBm}) - P_1\,(\text{dBm})] + K_{bs}, \end{aligned} \tag{4.17}$$

at any attenuator setting within the dynamic range of the $P_{1,2}$ measurements.

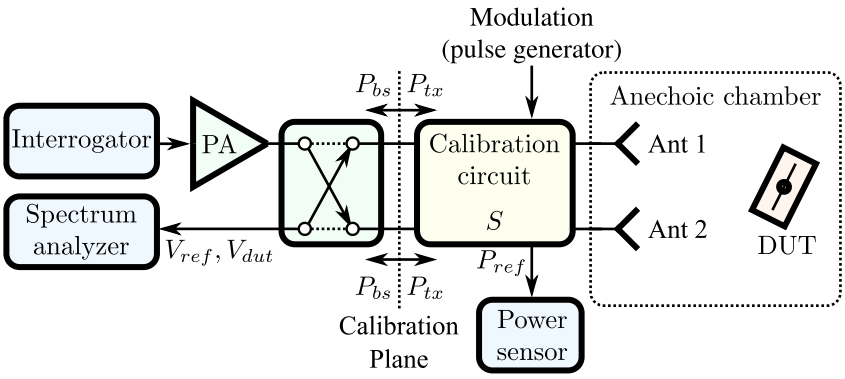

Figure 4.9: Test setup topology, with modulated power measurements of tag and reference scatter are referenced to the indicated calibration plane. The calibration circuit is illustrated in Fig. 4.5.

4.3 Testbed Design

The testbed is illustrated in Fig. 4.9. An interrogator transmits power and modulated query requests. Measurements use the circuit of Fig. 4.5 to calibrate results: coupled power measurements give P_{tx}, and reference modulation reflected to the input of the coupler calibrates P_{bs} from the DUT.

An antenna on the right, selected with the transfer switch shown left of the calibration plane, transmits interrogation to the DUT. A spectrum analyzer detects backscatter through the receive antenna. Repeating measurements in each transfer switch state gives two bistatic measurements of turn-on power P_{tx0} and P_{bs}, and therefore two results for B. The two values are averaged together to reduce random thermal noise and truncation errors.

The bistatic antenna topology maximizes carrier transmit/receive isolation. If the carrier at the spectrum analyzer is significantly stronger than the backscattered modulation, maintaining instrument linearity may require more attenuation, reducing backscatter measurement SNR and increasing noise uncertainty. Isolation between the two antennas is better than 45 dB across 860-960 MHz in the unloaded anechoic environment, and better than 30 dB when the chamber is loaded with a large metal plate.

The spectrum analyzer and interrogator each have return loss greater than 25 dB, and the calibration circuit loaded by the antennas has return loss greater than 15 dB, so mismatch errors (and the discrepancy introduced by switching between the inputs) are below 0.06 dB (1.5%).

A monostatic system could also be used, but would require an antenna with return loss greater than

Carrier	$860 - 960$ MHz
Interrogator-to-tag modulation	PR-ASK
Tag-to-interrogator modulation [2]	FM0
Tag-to-interrogator link rate (BLF) [2]	160 kHz
Interrogator-to-tag link rate	160 kHz (data 0)
	91 kHz (data 1)
Anticollision slots (Q) [2]	0 (no slots)
Delay after tag response† (T2) [2]	1 ms
Tari	6.25 µs

Table 4.2: Test Signal Parameters

30 dB over the test bandwidth or the additional complexity of a carrier cancellation circuit (e.g., [27, 28, 30]).

4.4 Measurement of Backscattered Power for Passive RFID

4.4.1 Detection and Signal Processing

A commercial RFID test instrument generates interrogation signals with signaling parameters as listed in Table 4.4.1. Each is approximately midway between the extrema permitted by [2].

Tag responses to query requests are measured during a 240 µs gate and reference backscatter during a 1 ms gate. Average transmit power P_{tx} is measured with the usual directional coupler procedure discussed in 4.1.3, gated as shown in Fig. 4.10(a) and calibrated . Turn-on and backscatter performance measured this way has been shown to be nearly independent of many modulation and coding parameters of the interrogation signal [94]. Reference backscatter is shut off during measurements of the tag response to avoid interference.

The spectrum analyzer records in-phase and quadrature traces $V_I(t)$ and $V_Q(t)$ of the received backscatter signal gated as in Fig. 4.10b. The recorded signal is digitized at discrete times $t = nT_0$ at baseband sampling rate T_0. The instrument records the digitally-sampled in-phase and quadrature baseband voltages. Transient ringing at digital pulse edges is minimized by setting the demodulation bandwidth is 10 MHz ($T_0 = 100$ ns), many times larger than the maximum 640 kHz base link frequency (BLF). Example gated backscatter signals are shown in Fig. 4.11, illustrating a 160 kHz DUT

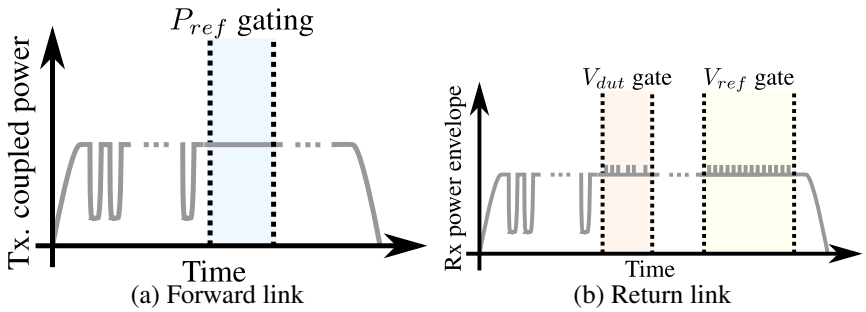

(a) Forward link (b) Return link

Figure 4.10: Illustration of gating applied to (a) coupled transmit power P_{ref}, and (b) DUT and reference backscatter baseband voltages V_{dut} and V_{ref}. Forward-link transmit modulation is shown coupled in (a), and leaked in (b) before measurements (performed during the shaded periods).

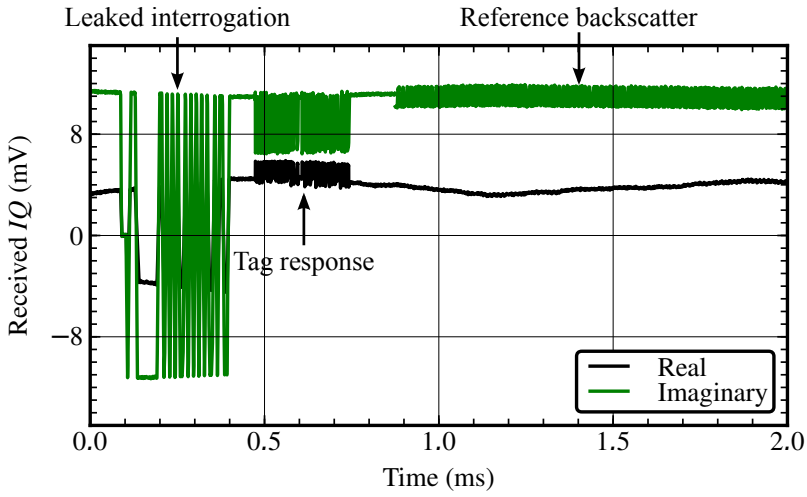

Figure 4.11: A demodulated trace from a transaction at 910 MHz with an ISO/IEC 18000-6C tag received by a spectrum analyzer. It shows leaked interrogation modulation from the forward link, the tag response from the reverse link, and reference backscatter from the calibration device introduced in this paper. In use, the reference backscatter is only turned on when it is being measured, to avoid interfering with the tag.

response to a query command.

Carrier phase noise at baseband was measured as large as 1.5° per symbol at 160 kHz, and as large as 13° per 240 µs signal trace. Baseband drift is negligible between neighboring symbols noticable on the scale of the full trace width.

Algorithmic determination of discrete signal state levels in pulsed or digital signals is known as clustering. The usual approach is identify histogram peaks in V_I and V_Q [114], which has the advantage of readily estimable uncertainty [115]. Unfortunately, the signal phase noise over the course of a frame can be larger than the I and Q components and was often larger than the backscattered signal, making the straightforward histogram analysis inapplicable.

The alternative clustering algorithm in the backscatter testbed is a one-dimensional application of the Canny edge detection filter [116]. First, a discrete Gaussian filter is applied to the digitally sampled V to remove noise without distorting pulse edges. The signal is approximately a sequence of rectangular pulses between two signal levels, so its derivative should give "spikes" close to a discrete (Kronecker) delta function at each transition. Thus, local amplitude maxima of the numerical derivative of the result are reported as pulse transitions. The center 80% of the span between the time-value of each pulse transition is recorded as a pulse state. Peaks greater than the signal standard deviation are recorded as digital switches. The mean difference between neighboring pulses is recorded as the change in real and imaginary components, ΔV_I and ΔV_Q.

Uncalibrated state changes in DUT and reference modulation are recorded as $|\Delta V_{dut}|$ and $|\Delta V_{ref}|$ as $\Delta V_I + j\Delta V_Q$. The corresponding DUT and reference power levels are $P_{bs,dut} = |\Delta V_{dut}|^2/(4Z_0)$ and $P_{bs,ref} = |\Delta V_{ref}|^2/(4Z_0)$ by equation (2.25). The calibrated DUT backscatter power, P_{bs}, is computed with equation (4.14) by the procedure in Section 4.1.3.

Figure 4.12 shows a power sweep of the uncalibrated power measurements $P_{bs,ref}$ and $P_{bs,dut}$, and the calibrated P_{bs}. The reference power $P_{bs,ref}$ is generated through the reference backscatter device of Fig. 4.5. The very nonlinear power from the DUT tag, $P_{bs,dut}$, shows the expected sharp turn-on threshold behavior as transmit power increases; below turn-on, the measured backscatter is equal to this measurement's noise floor below -90 dBm. Reference modulation power is very linear with transmit

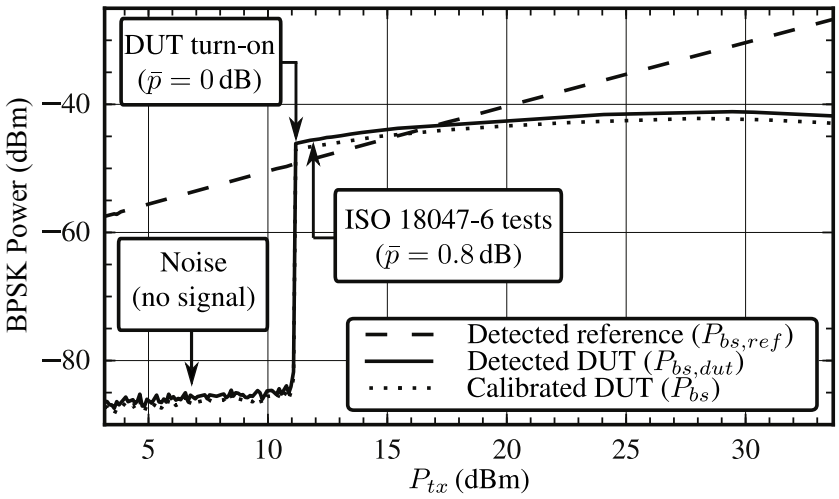

Figure 4.12: Measurements of backscattered power comparing detected DUT and reference backscatter power and the DUT power after calibration. The both the reference and DUT applied 160 kHz modulation to a 910 MHz carrier according to table 4.4.1.

Network analyzer calibration	± 0.25 dB
Power measurements	± 0.25 dB
IQ level measurements	± 0.05 dB
Noise and nonlinearity	± 0.1 dB
Expanded uncertainty	± 0.4 dB

Table 4.3: Estimated Backscattered Power Measurement Uncertainty Estimate ($-60\,\text{dBm} < P_{bs} < -20\,\text{dBm}$, $10\,\text{dBm} < P_{bs} < 30\,\text{dBm}$, $k = 2$)

power, so the calibration factor K is approximately constant with input power in this sweep. Calibrated DUT power, P_{bs}, is therefore offset from $P_{bs,dut}$ by a constant.

4.4.2 Combined Uncertainty

To gauge the effectiveness of the reference backscatter calibration, an uncertainty estimate for calibrated backscattered power measured with the testbed is presented in Table 4.4.2.

Reported values follow the methods for evaluating uncertainty discussed in 1.4, with each source listed here in concise form. Each uncertainty term is the fractional uncertainty and combined according to the law of propagation of uncertainty expressed in (1.23).

Testbed linearity is estimated from measurements of the reference backscatter as a function of power, shown in Fig. 4.13. This measurement was performed with a bistatic receiver setup. Results between the two traces agreed within ± 0.1 dB, which is then the estimate for linearity and noise uncertainty.

Uncertainty in the IQ measurement processing, caused by ringing or level clustering errors, quoted at ± 0.05 dB, is based on monte carlo simulation of digital signals switched at 640 kHz, bandlimited to 12 MHz, sampled at 10 MHz, and with SNR limited to the $P_{bs,dut} = -60$ dBm lower specification limit.

Manufacturers provide detailed guidelines for estimating the uncertainty of power measurements. The two are necessary for each P_{bs} calibration are conventional uses of power meters and sensors. The ± 0.25 dB error estimate results comes by adding the correlated errors arithmetically, plus the RMS sum of the uncorrelated error sources.

Uncertainty of a vector difference between two measured reflection coefficients to determine $\Delta\rho_1$ or $\Delta\rho_L$ is an interesting and nonstandard problem not addressed by in published literature or manufacturer guidelines. Two approaches to estimating this uncertainty, 1) Monte carlo simulation and 2) estimating

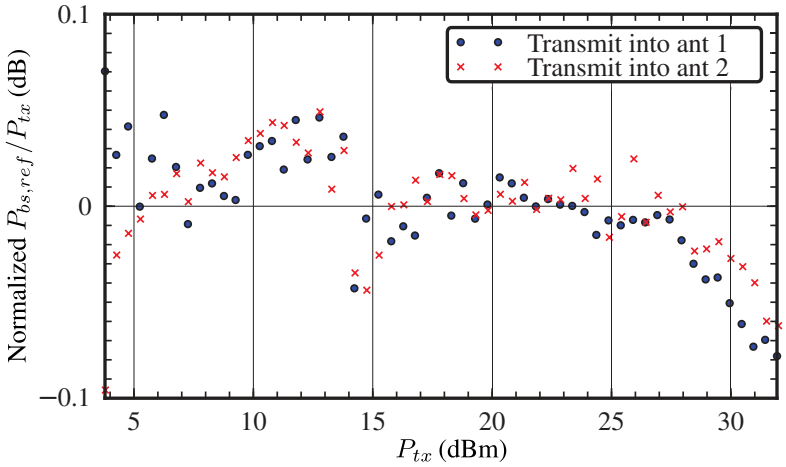

Figure 4.13: Reference backscatter linearity errors measured by sweeping transmit power and measuring the reference backscattered power. The backscatter reference load-modulated 910 MHz carrier reflections at 160 kHz with the circuit described in Fig. 4.1. Deviation from linearity below 32 dBm input power was less than 0.1 dB.

systemic errors that cancel in the two reflection coefficients, suggests uncertainty of about 0.25 dB. Interestingly, for a wide range of different reflection coefficients, the uncertainty of a measured $|\Delta\rho|$ is about the same as that of a transmission coefficient, with a factor of $\sqrt{2}$ extra noise.

Other sources of error are small enough to be omitted from Table 4.4.2. After power calibration against the reference backscatter, the relative error betweeen signal analyzer power measurements is below 0.08 dB and contribute negligibly to combined uncertainty. Empirical tests also found less than 0.1 dB error in reorienting the location of objects in the test zone.

4.5 Summary

The devices and test methods proposed here generate reference signals suitable for transceiver or transponder performance tests. For transponders, reference backscatter may be generated 1) through fixed-loss coaxial networks and 2) over-the-air through antennas. For reader testing, another coaxial calibration device can reflect adjustable modulation power into monostatic reader ports. Testbeds designed with these calibration techniques are overspecified compared to realistic commercial test requirements.

Material in this chapter originated in the following peer-reviewed publications by the author:

D.G. Kuester, D.R. Novotny, J.R. Guerrieri, Z. Popović, "Simple Test and Modeling of RFID Tag Backscatter," *IEEE Trans. on Microwave Theory and Techn.*, vol. 60, no. 7, July 2012, pp. 2248-2258.

D.G. Kuester, D.R. Novotny, J.R. Guerrieri, R.H. Direen, Z. Popović, "Reference Modulation for Calibrated Measurements of Tag Backscatter," *Proc. 2011 IEEE Intl. Conf. on RFID*, 12-14 Apr 2011.

D.G. Kuester, D.R. Novotny, J.R. Guerrieri, "Simple Test and Modeling of RFID Tag Backscatter," *IEEE Trans. on Microwave Theory and Techn.*, vol. 60, no. 7, July 2012, pp. 2248-2258.

Chapter 5

Measurement of Passive Backscatter Performance

Have no fear of perfection — you'll never reach it.

Salvador Dalí (1904-1989)

5.1 Introduction

Chapter 3 identified two characterizations of tag backscatter performance: the BPSK radar cross Section σ_{Δ}, which is essentially the existing metric, and the alternative figure of merit B at the core of this thesis. Performance and conformance test standards ISO/IEC 18046-3 and ISO/IEC ISO18047-6 already suggest some test methods for bistatic σ_{Δ} [38, 41]. Even though these standards are targeted at RFID, current tag datasheets do not give backscatter test data. It is clear the industry is not convinced that the these data are useful enough to justify the cost of testing.

What are the benefits of backscatter test data? Accurate σ_{Δ}, coupled with reader sensitivity and antenna performance data, gives an idea of the maximum detectable range of an RFID tag. Accurate B gives an idea of the worst-case backscatter power received by the reader and thus, with reader sensitivity performance data, give a lower bound for the SNR or SIR and thus communication error rate.

The analog identifier tag characteristic of [112, 113] is substantially similar to the special case $B|_{\bar{p}=1}$. These seminal papers were published during peer review of the author's metrology-focused [71]. The goal in these references is tag "self-sensing:" sensing changes to the tag surroundings via changes to $B|_{\bar{p}=1}$. Changes to $B|_{\bar{p}=1}$ were detected by measuring threshold transmit power from a commercial reader, P_{tx0}, and corresponding backscattered power, $P_{bs}|_{\bar{p}=1}$. The fact that a reader is not a calibrated measurement instrument is not a problem for these relative measurements: reader linearity and relative error were found by calibrating against initial results, so absolute accuracy of $B|_{\bar{p}=1}$ was not important. A technical challenge that has not yet been resolved in this approach to sensing is controlling thermal stability of the uncalibrated measurements of $B|_{\bar{p}=1}$.

In contrast, measurements of B in this thesis are meant for link modeling and determining $\min(P_{bs})$. The power levels are only meaningful if they can be compared directly, which requires measurements traceable to fundamental power and S-parameter standards. These two physical quantities, when measured with qualified power sensors or network analyzers, are traceable against standards from national metrology institutes like NIST. The previous chapter gave test methods for traceable power measurements of P_{bs} and P_{tx}.

This chapter investigates the use of calibrated power measurements to determine B and the BPSK RCS, σ_{Δ}. With an estimate of the uncertainty of these measurements, a coaxially connectorized RFID tag is constructed that validates both the model and theory of B. These results confirm that the theory predicts B (and thus $\min(P_{bs})$) to within the predicted ± 0.43 dB tag measurement testbed uncertainty in an anechoic environment.

5.2 Uncertainty: How Good is "Good Enough?"

The central goal of RF measurement in this thesis is to support analysis of signals power to estimate communication error rates as a reliability metric. Lower measurement uncertainty, and the corresponding expectation of improved measurement accuracy, can often be realized at the expense of added time, effort, and cost. Comparison of the measurement costs against the benefits of lower uncertainty requires some understanding of test uncertainty propagates to uncertainty in the link analysis.

Estimates of received backscattered power P_{bs} depend on measured tag performance via σ_Δ or B, so uncertainty in either of these affects the uncertainty of the predicted P_{bs}. If the uncertainty of P_{bs} is increased, then minimizing communication errors requires tighter specifications in the form of improving reader sensitivity, or possibly derating system performance in terms of tag operating range or communication error rate.

5.2.1 Measurements Uncertainty of σ_Δ vs. P_{bs}

We can begin with the general $P_{bs} \propto \sigma_\Delta / L^2$, since $\sigma_\Delta \propto \eta_{mod}$. As before, L is available power loss between the transmitter and load modulation, and η_{mod} is the proportion of incident power re-reflected by the load modulator as BPSK modulation.

Consider any two independent random variables X and Y. The variance of their product obeys the identity [117]

$$\text{Var}(XY) = [\text{E}(X)]^2\text{Var}(Y) + [\text{E}(Y)]^2\text{Var}(X) + \text{Var}(X)\text{Var}(Y), \tag{5.1}$$

and, because they are independent,

$$\text{E}(XY) = \text{E}(X)\text{E}(Y). \tag{5.2}$$

Thus

$$\frac{\text{Var}(XY)}{[E(XY)]^2} = \frac{\text{Var}(X)}{[\text{E}(X)]^2} + \frac{\text{Var}(Y)}{[E(Y)]^2} + \frac{\text{Var}(X)}{[\text{E}(X)]^2}\frac{\text{Var}(Y)}{[\text{E}(Y)]^2}. \tag{5.3}$$

The square root of each side of this equation relates the fractional variances of the product XY to the fractional uncertainties of X and Y.

Similarly, because σ_Δ and $1/L^2$ are independent and P_{bs} is proportional to their product, their relative variances are:

$$\begin{aligned} \text{Fractional variance of } P_{bs} &= \frac{\sqrt{\text{Var}(P_{bs})}}{[\text{E}(XY)]^2} \\ &= \sqrt{\overline{\text{Var}}(\sigma_\Delta) + \overline{\text{Var}}(1/L^2) + \overline{\text{Var}}(\sigma_\Delta)\overline{\text{Var}}(1/L^2)}. \end{aligned} \tag{5.4}$$

Here, $\overline{\text{Var}}(\cdot)$ is fractional variance (variance normalized to $[\text{E}(\cdot)]^2$). The distribution of our stochastic P_{bs} is therefore always more spread out than either the sum or the product of its parts.

The relative contribution of σ_Δ uncertainty onto the variance of P_{bs} is thus

$$\frac{\overline{\text{Var}}(P_{bs})}{\overline{\text{Var}}(1/L^2)} = \sqrt{1 + \frac{\overline{\text{Var}}(\sigma_\Delta)}{\overline{\text{Var}}(1/L^2)} + \overline{\text{Var}}(\sigma_\Delta)}. \tag{5.5}$$

In the limit of strong fading, the variance in $1/L^2$ is large, and the center term in the radix becomes negligible,

$$\sqrt{\frac{\overline{\text{Var}}(P_{bs})}{\overline{\text{Var}}(1/L^2)}} \approx \sqrt{1 + \overline{\text{Var}}(\sigma_\Delta)}. \tag{5.6}$$

Figure 5.1 illustrates implications of equations (5.4) and (5.6). Discussion so far has been general for any distribution of P_{bs} and σ_Δ. To connect variance with uncertainty discussed in Section **??**, the illustration assumes normally-distributed combined error in σ_Δ with coverage factor 2, and thus the value $\sqrt{\overline{\text{Var}}(\sigma_\Delta)}/2$. The representative range of fractional uncertainties is broad: 0.5 dB is better than any claimed in the literature, 2 dB is reasonable for the anechoic measurements of [45], and 6 dB is observed in a storage room in Section 5.4.

The curves of Fig. 5.1a show that when the standard deviation of backscattered power in the realistic environment is greater than the σ_Δ uncertainty, the contribution of uncertainty in σ_Δ to uncertainty in P_{bs} becomes approximately constant. The additional uncertainty in P_{bs} in this limit is plotted in Fig. 5.1b. In this limit, the uncertainty added to our stochastic P_{bs} is always less than the uncertainty of σ_Δ.

The definition of what is a "good enough" uncertainty result in measured σ_Δ therefore requires a choice about an acceptable increase in uncertainty in P_{bs}. Two good rules of thumb come from Fig. 5.1b in strong multipath environments: first, measurement uncertainty below 4 dB affects the uncertainty of P_{bs} by less than 1 dB; second, measurement uncertainty below 2 dB affects the uncertainty of P_{bs} by less than 0.2 dB. The latter is a reasonable expectation with existing test methods outlined in the next Section [45, 46], making the contribution of σ_Δ to predictions of realistic monostatic P_{bs} quite small.

5.2.2 Measurements Uncertainty of B vs. min(P_{bs})

Analysis of uncertainty of $\min(P_{bs})$ with B is much simpler, because the only concerns are:

(1) measurement uncertainty in B (addressed in the next chapter with design of the measurement testbed); and

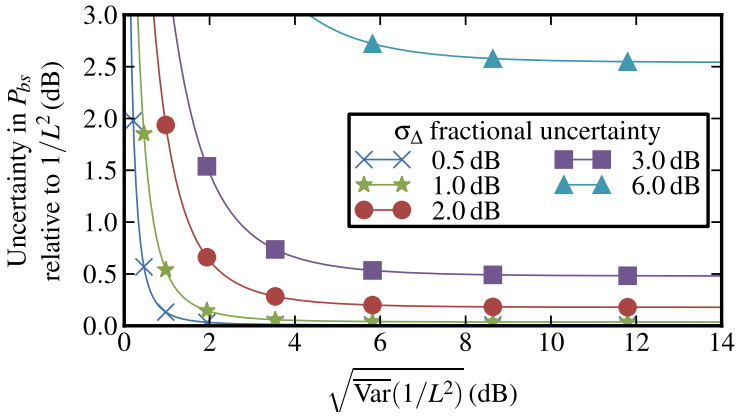

(a)

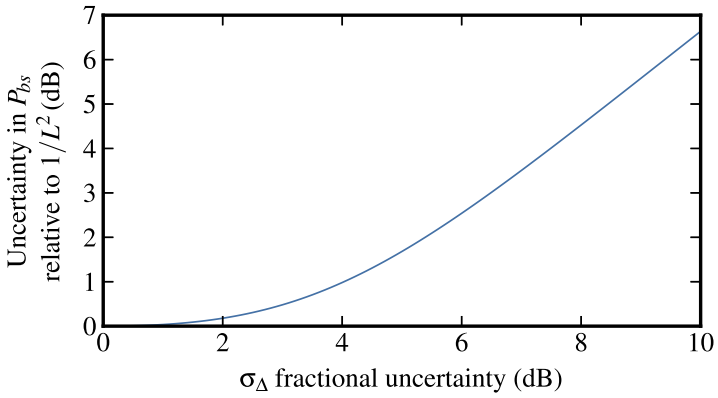

(b)

Figure 5.1: Fractional uncertainty added in stochastic models of P_{bs} ($\sqrt{\overline{\text{Var}}(P_{bs})/\overline{\text{Var}}(1/L^2)}$ by measurement uncertainties in σ_Δ via (a) various representative σ_Δ uncertainties swept with $1/L^2$ standard deviation in equation (5.4), and (b) for strong multipath, $\overline{\text{Var}}(1/L^2) \gg \overline{\text{Var}}(\sigma_\Delta)$, by equation (5.6).

(2) uncertainty in P_{tx}, which is small and negligible.

The uncertainty of $\min(P_{bs})$ from test data is therefore approximately the same as the uncertainty of B. If B is measured accurately and detuning of B can be controlled, then an estimate of the $\min(P_{bs})$ bound is also very accurate.

5.3 Prior Art: Anechoic RCS Measurements in ISO 18047-6

The only prior work the author has identified about digitally modulated backscatter communication metrology is applied to UHF RFID, and is encapsulated inside ISO 18047-6 [41].

5.3.1 Procedure: ISO 18047-6 (2006 version)

The 2006 version of UHF RFID test standard ISO 18047-6 [41] (now obsolete) was the state of the art when this work began. It contains test recommendations for σ_Δ that calibrate receive tag signals against carrier scattering measurements off of a thin $\lambda/2$ rod. This rod is the CW "calibration target." This test approach is similar to many RCS measurements for which the DUT is a passive structure that reflects only CW.

Tests that emulate this behavior are shown in Fig. 5.2. The shorted dipole mimics the thin rod used for tests. Two discrete states are presented to the measurement receiver by manually inserting and removing the entire reflecting structure. This approach also allows study of transmission behavior to the dipole. The standard prescribes a bistatic testbed antenna configuration, though monostatic σ_Δ is measureable with the same kind of test. The method is simple, though it is revised here slightly to correct the problematic use of power envelope detection described in Section **??**.

Chapter 2 shows that detection of digitally modulated backscatter requires an IQ detector. The corresponding phase component is included by network analyzer measurement of the change in complex S-parameters looking into the "reader" antenna; $|\Delta\rho_1|/4^2$ or $|\Delta\tau_{21}/4|^2$ approximates P_{bs}/P_{tx} given the well-matched network analyzer. Since the change in ρ_1 is realized by adding and removing the entire scattering structure, we are thus modulating both the antenna mode reflections (by adding and insert-

ing the load) *and* the structure of the antenna. In the free field, we therefore expect that P_{bs}/P_{tx} is proportional to the total CW RCS, σ (not the load-modulated BPSK RCS σ_Δ of (3.22) via the radar equation.

First, a network analyzer measures $|\Delta\tau_{21}^{(ref)}|^2$ (or $|\Delta\rho_1^{(ref)}|^2$ in monostatic setups), from measured states corresponding to transmission between the bistatic testbed antennas 1) loaded by the calibration target, then 2) unloaded. It is calibrated with an electronic calibration unit to a reference plane defined at the patch antenna's coaxial input port. This is the calibration reference target with some known cross-Section σ. For the thin $\lambda/2$ rod, various results give σ within the range $0.6\lambda^2$ to $0.9\lambda^2$ [**Green1962**, 118, 119]; the 2006 version of ISO 18047-6 prescribes a single value to use as σ. A correction factor, "K," is taken to encompass the unknown terms of the radar equation:

$$|\Delta\tau_{21}^{(ref)}|^2 = K\sigma, \tag{5.7}$$

where

$$K = \frac{G_{tx}^2(\theta_{tx},\phi_{tx})\lambda^2}{(4\pi)^3 r^4}|\hat{\mathbf{u}}_3 \cdot \hat{\mathbf{u}}_{tx}|^2. \tag{5.8}$$

Note that there is no η_{rx}/η_{tx} factor in K, because it cancels with the network analyzer defined as $\rho_{I1} = 0$, and further the transmit and receive antennas are implicitly assumed to be well matched to an unspecified extent.

The test zone is now empty, because the reference target was removed in the measurement of $|\Delta\tau_{21}|^2$. To measure the DUT, we place it centered exactly where the reference target was located, replacing the network analyzer with an IQ receiver (such as a signal analyzer). Measuring the BPSK power received from the tag, P_{bs}, and assuming K is unchanged from (5.8), we get the BPSK radar cross Section of the DUT:

$$\begin{aligned}\sigma_\Delta &= \sigma\frac{P_{bs}}{P_{tx}}|\Delta\tau_{21}^{(ref)}|^2 \\ &= \sigma^{(ref)}(\theta_3,\phi_3)\frac{1}{K}\end{aligned} \tag{5.9}$$

The main errors here are not obvious from these simple equations. First, the calibration target is detected with a network analyzer (calibrated to an unspecified reference plane), but DUT backscatter is received by a completely different instrument like an oscilloscope or signal analyzer. Before the writing

Scatterer	Measured $\lvert\Delta\tau_{21}\rvert^2$
Thin $\lambda/2$-long rod RCS target	-40 dB
Engineer in the chamber door	-49 dB
Pen left in chamber ($r = 1$ m)	-45 dB
Small RFID tag left in chamber ($r = 1$ m)	-49 dB
Accidentally rotate reference antenna $\pm 15^\circ$	-41 dB

Table 5.1: Measured $\lvert\Delta\tau_{21}\rvert^2$ for some unintended events in the test zone

of this thesis, there was no prescribed method for calibrating detection of P_{bs}. Second, K is only constant in each measurement if the entire test setup is undisturbed each of the 3 times the operator enters and exits the chamber. Any displacement of walkway absorber, antenna positions or orientations, or receiver cables changes K and adds error to the measurement of σ_Δ. Some examples of measured changes in $\lvert\Delta\tau_{21}\rvert^2$ seen in the NIST RFID test chamber are listed in Table 5.1, shown for comparison with the measured value of the calibration target.

5.3.2 Procedure: ISO 18047-6 (2011 version)

The 2011 update to ISO18047-6 adopts changes from [44] in measurements of σ_Δ. It is almost opposite of the 2006 version: instead of calibration against a known scattering target, each term in the radar equation is computed or measured separately.

In terms of (3.18):

$$\sigma_\Delta(\theta_3, \phi_3) = \frac{P_{bs}}{P_{tx}} \frac{\eta_{tx}}{\eta_{rx}} \left[G_{tx}(\theta_{tx}, \phi_{tx}) G_{rx}(\theta_{rx}, \phi_{rx}) \frac{\lambda^2}{(4\pi)^3 r_{tx}^2 r_{rx}^2} |\hat{\mathbf{u}}_{ant,tx} \cdot \hat{\mathbf{u}}_{tx}|^2 \right]^{-1}. \tag{5.10}$$

It is reasonable to assume here that the testbed can be built with a well-matched receiver and transmitter and antennas, so we neglect mismatch. This leaves P_{bs}, P_{tx}, G, reader antenna gains, and the polarization terms to be measured.

5.4 Multiple Reflection Errors in RCS Calibrations

In moving toward environment-independent tests from the standardized RCS test methods described in the previous Section, a logical next step is to consider the effects of the environment on these tests. Careful control over the test environment can minimize measurement errors from antenna detuning and

ambient electromagnetic interference, and help to maintain adequate measurement dynamic range. In contrast, errors from multiple reflections in an "anechoic" test environment are challenging to quantify and costly to mitigate.

Reflections in the environment contribute differently to the uncertainty of the DUT σ_Δ measurement, depending on whether the 2006 or 2011 type of measurement is performed. In the "direct" σ_Δ test of Section 5.3.2, any relative error in propagation loss compared to $1/r^4$ adds the same relative error to the measured σ_Δ. A subtler problem posed by multiple reflections in calibrations against CW RCS targets (as in Section 5.3.1) is that structural-mode scattering from the calibration reference target perturbs standing waves in the test area, while there is no structural-mode modulation in signals from the tag DUT. Otherwise, as long as the gain patterns of the DUT are similar to a $\lambda/2$ dipole, we could naïvely expect that multiple reflections would have the same effects on both the calibration reference target and the DUT.

This Section considers these multiple reflection effects on σ_Δ tests by comparing measurements taken in a semi-anechoic environment and repeated in a more reflective storage room. The measurements are illustrated by Fig. 5.2. First, $1/|E_{31}|^4 \approx L^2$ between the patch and dipole is measured as the antenna-mode backscatter loss, with S-parameters calibrated as shown in Fig. 5.2a. This emulates losses experienced by a load-modulated passive tag. The reflection coefficient at one of the "reader" patch antennas is measured in each of the two states of the calibration target simulated in Fig. 5.2b: the test environment (1) with, then (2) without the shorted dipole and matched feed. The magnitude of the difference between the two values is reported as $|\Delta\rho_1|^2$, proportional to backscatter power introduced by the target RCS and its interaction with the environment. The noise floor of $|\Delta\rho_1|^2$ measurements was lower than -75 dB across 700-1100 MHz.

The patch and dipole antennas are oriented to boresight with a laser square and co-polarized with a level in each E_{31} and $|\Delta\rho_1|$ measurement. The range r between the two antennas, shown dotted in Fig. 5.2, is measured by laser range finder in each experiment.

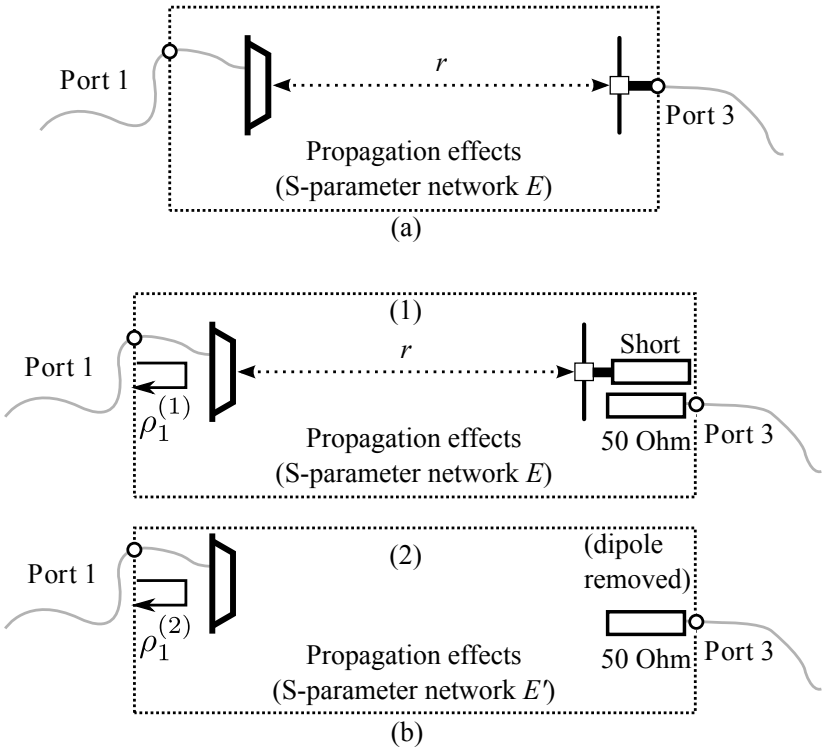

Figure 5.2: Scattering measurement setup. In the forward link configuration (a), a full two-port measurement was performed with the network analyzer, calibrated to the S-parameter reference planes shown; measurements of $|E_{31}|^2$ are taken to describe link losses. In the reverse link measurement (b), measurements of the 1-port reflection coefficients $\rho_1^{(1)}$ and $\rho_1^{(2)}$ give difference $|\Delta\rho_1|^2$. This emulates ISO/IEC 18047-6 tests and gives transmission loss via $L \approx 1/|E_{31}|^2$.

	$\lvert E_{31}\rvert^4$		$\lvert\Delta\rho_1\rvert^2$		Apparent phase-center offset
	Std. Dev.	Worst	Std. Dev.	Worst	
CP patch	0.10 dB	0.48 dB	0.22 dB	1.1 dB	0.008 - 0.049 m
LP patch	0.14 dB	0.46 dB	0.45 dB	1.5 dB	0.042 - 0.059 m

Table 5.2: Regression information from Fig. 5.4 within 895-935MHz

5.4.1 Measurements in an Anechoic Environment

The author constructed a cubic semi-anechoic chamber with 2.4 m walls on each side with an open top leading to another anechoic surface at the lab ceiling 7.6 m above. It is pictured in Fig. 5.3. The centerpiece of this aesthetically optimal carpentry exercise is a foam table, which supports lightweight calibration or DUT targets. Absorber cones are 30 cm long, except opposite the interrogation antennas, which are 60 cm long to maximize absorption in the main beam of the testbed antennas.

In front of one wall is a mount for one or two interrogation antennas to support monostatic or bistatic operation. Two commercially-available patch antennas with peak gain 8.5 dBi and return loss greater than 25 dB 902-928 MHz are on hand: one was linear polarized (LP), and the other circular polarized (CP).

A straightforward approach to estimating multiple reflection errors in the test zone is to measure the square of transmission, $|E_{31}|^4$, and backscatter, $|\Delta\rho_1|^2/4$, swept with interrogator-to-target antenna separation r. Both should follow $1/r^4$ closely; regression error relative to this trend will suggest the uncertainty due to reflections and misalignments in the test zone. These results give an idea for typical errors in testing DUTs that have broad gain patterns.

Semi-anechoic room measurements are shown in Fig. 5.4 with a regression $-10\log_{10}(r^4)$. Statistics are computed in linear units before conversion to dB. The residuals listed in Table 5.2 give an idea for the multiple reflection errors in the test zone in this anechoic environment. The scattering measurements in the anechoic environment do decay as $1/r^4$, with a conservative rough uncertainty of around ± 1 dB to ± 2 dB. These are limited by a combination of the [im]precision of the hand-measured antenna positioning and orientation and standing waves caused by reflections in the test zone. Because $1/L^2$ is much smaller than P_{bs}/P_{tx}, the relative error between antenna-mode scattering and the CW RCS calibration target here also gives uncertainty of around ± 1 dB to ± 2 dB. If a scattering target with modulated loads

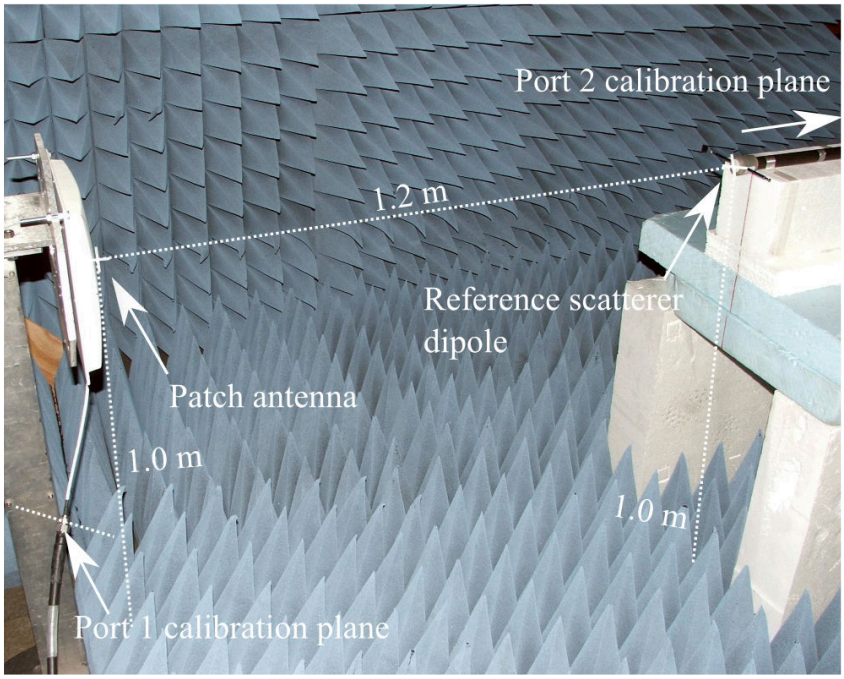

Figure 5.3: The measurement setup in the semi-anechoic chamber. The LP reader antenna is shown attached to the mounting structure on the left, and the target dipole is on the right.

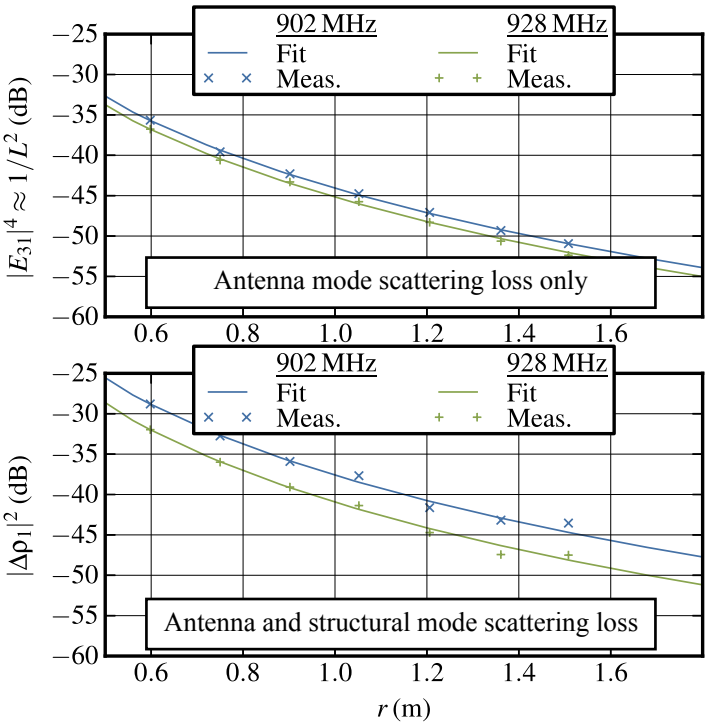

(a)

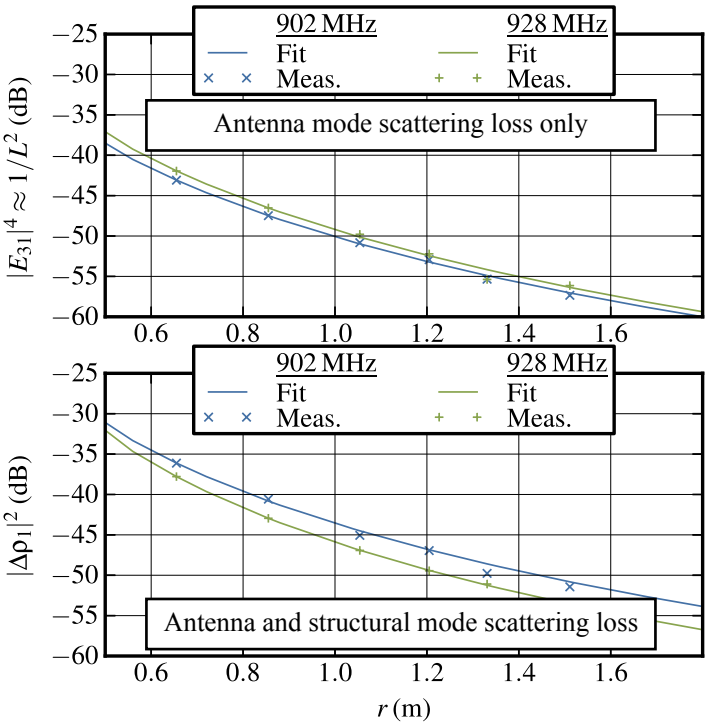

(b)

Figure 5.4: Measurements of antenna-mode scattering $(1/L^2)$ and mixed antenna- and structural-mode scattering $|\Delta\rho_1|^4$ and scattering measurements against range with (a) the 8 dBi LP patch and (b) the 8 dBi CP patch antennas. The curves are fitted to free field r dependence. Regression information across 895-935 MHz are in Table 5.2.

	ISO 18047-6 (2006): Calibration against CW RCS standard	ISO 18047-6 (2011): No calibration (only radar equation)
Semi-anechoic chamber	1.5 dB	0.5 dB
Storage room	6 dB	6 dB

Table 5.3: Estimates of worst-case standing wave error relative to ideal free space

were available as a calibration reference, positioning and reflection errors would be less than ± 1 dB, following $|E_{31}|^4$, even with the transmission measurement cable.

Assuming these results are representative of the dominant error in the measurements, both of these test procedures fit the goal of less than 2 dB uncertainty that we determined in Section 5.2.

5.4.2 Storage Room Results

ISO 18047-6 measurements in a large non-anechoic room with the penalty of increased measurement uncertainty are one approach to reducing σ_Δ test costs. These more reflective environments are already often used for the simple "read range" tests reported by many manufacturers.

Measuring structural mode components in a more reflective environment via $|\Delta\rho_1|^2$ and comparing against the anechoic room results can give some insight here. The storage room pictured in Fig. 5.5 presents many potential sources of scattering to the reader antenna. The author performed measurements here under the same procedure as in the semi-anechoic environment. Line-of-sight was maintained between the antennas in all tests.

Results are plotted in Figs. 5.6 and 5.7 swept with range, with the reader antenna position kept fixed. To make the effects of multiple reflection clear, results from the storage room environment are normalized to semi-anechoic chamber data. Transmission and backscatter losses vary by up to about 10 dB compared to the anechoic environment. Standing waves between the target and the floor also give about 1 dB of ripple in the CP patch data.

These data result in the σ_Δ test uncertainty estimates in the two environments compared in Table 5.4.2. Both are assumed dominated by propagation and misalignment errors measured here. The uncertainty in the storage room is about 6 dB with both the CW RCS calibration method (from $|\Delta\rho_1|^2/4/L^2$) and by direct use of the radar equation (by directly examining $1/L^2$).

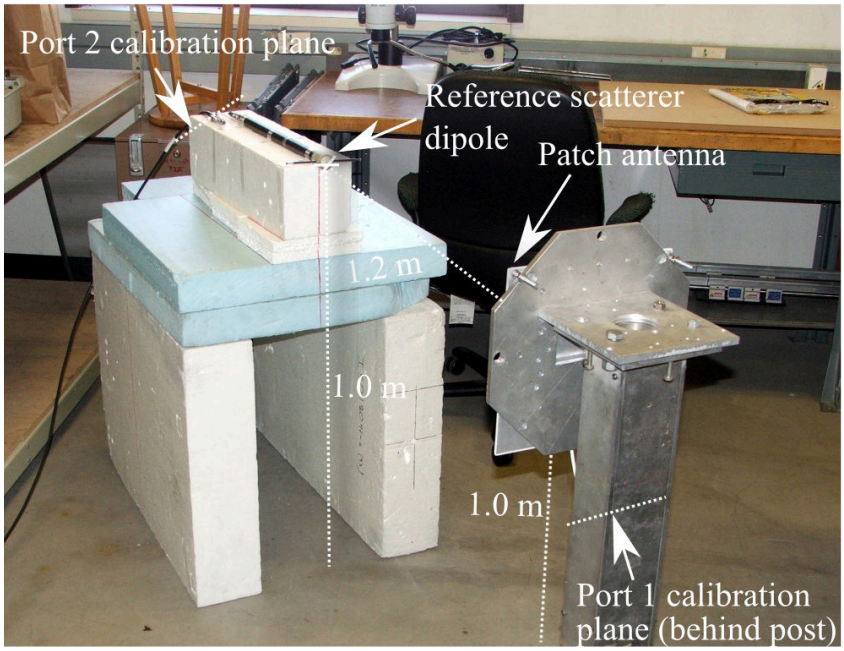

Figure 5.5: A reverberant environment. The ceiling, walls, and floor are steel-reinforced concrete. There is a large outdoor-facing window above the frame of the photograph, a large workbench and wall in the rear, shelving containing with test equipment on the right and left.

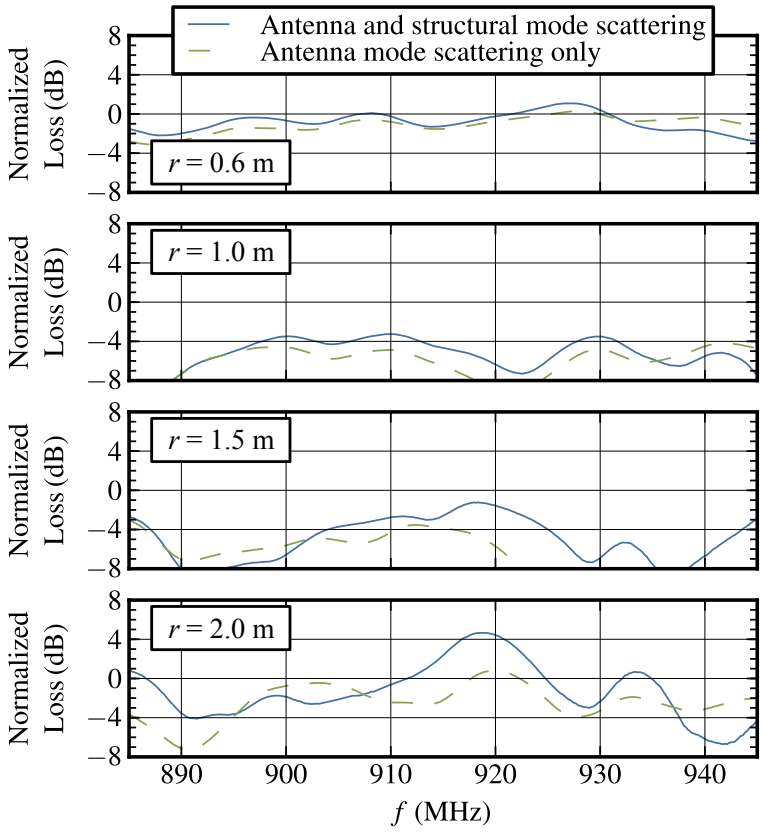

Figure 5.6: LP transciever antenna backscatter loss, measured in the environment pictured in Fig. 5.5. Normalization is against the anechoic results of Fig. 5.4, at each separation distance r. "Antenna and structural mode" scattering is $|\Delta\rho_1|^2$ found by adding and removing the shorted dipole RCS standard; "antenna-mode only" scattering is $|E_{31}|^4 \approx 1/L^2$.

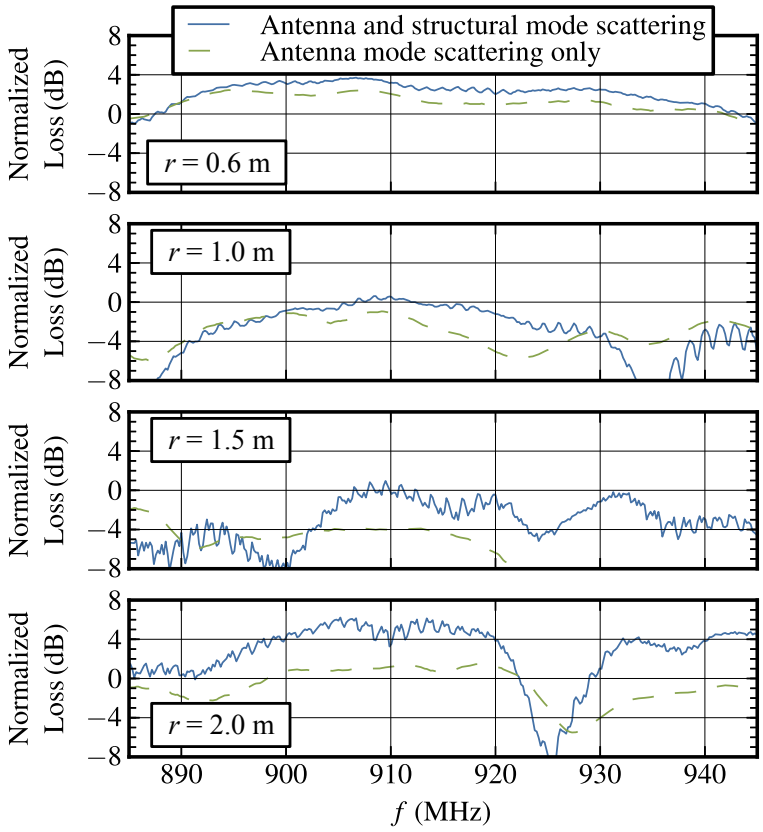

Figure 5.7: CP transciever antenna backscatter loss, measured in the environment pictured in Fig. 5.5. Normalization is against the anechoic results of Fig. 5.4, at each separation distance r. "Antenna and structural mode" scattering is $|\Delta\rho_1|^2$ found by adding and removing the shorted dipole RCS standard; "antenna-mode only" scattering is $|E_{31}|^4 \approx 1/L^2$.

Figure 5.1b suggests that even under the best case of very strong fading, we expect to add about 3 dB to stochastic estimates of P_{bs}. This may be significant relative to a backscatter link margin, and represents uncertainty in coverage range of about 40%.

Thus, the radar cross Section test methods discussed here yield "good enough" uncertainty in reflective indoor environments typical of engineering labs. Environmental effects with the new test method proposed in [120] have not yet been investigated; its use of a load-modulated calibration standard may reduce uncertainty in σ_Δ calibrations in non-anechoic environments.

5.5 Measurement of B

Calibrated measurements of P_{tx} and P_{bs} give B in decibels defined here as

$$\begin{aligned} B\ (\text{dBm})^2 &= P_{tx0}\ (\text{dBm}) + P_{bs}\eta_{tx}\eta_{rx}\ (\text{dBm}) \\ &= 10\log_{10}\left[P_{tx0}\,(\text{mW}) \times\ P_{bs}\eta_{tx}\eta_{rx}\,(\text{mW})\right]. \end{aligned} \tag{5.11}$$

The nonstandard decibel unit here, $(\text{dBm})^2$, is as defined in (3.31).

The goal of the measurement described in this Section is the ideal B in an anechoic environment. Thus, the effect of reflectors on the tag antenna impedance (detuning) is considered a measurement error. In measurements performed in a realistic environment, tag detuning could be part of the measurement instead of the error.

Since measurement and uncertainty of P_{bs} is discussed in Section **??** and measurement of the carrier transmit power is broadly understood, we primarily consider combined uncertainty effects on B.

5.5.1 Nonlinearity Sweeps

The calibration procedures given for tag backscatter measurements in Chapter 4 all assume that detection and reference backscatter are all ideally linear with respect to power. Thus, any nonlinearity in the measurement testbed is a source of error that needs to be considered in the uncertainty analysis process. The signal analyzer specifies the error at a few hundredths of a decibel (about 1% linear), and the power sensor specifies 0.1 dB (about 2.5% error). The solid state switch for reference backscatter has negligible nonlinearity error from compression below 29 dBm.

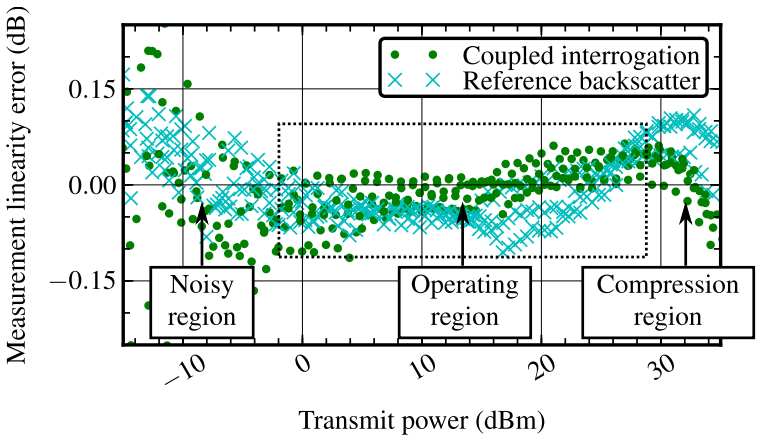

Figure 5.8: Dynamic range tests of transmit and reference backscatter power, combining 860, 910, and 960 MHz results. Transmitting -2 dBm to +29 dBm, linearity and noise errors are less than 0.1 dB. Backscatter noise is not zero-mean because the normalization is skewed by high-power compression.

Coupled interrogation power and reference backscatter power are swept with transmit power in Fig. 5.8 to validate that the combined system meets specification. Results are re-normalized against transmit power. The result is a plot combining thermal noise and nonlinearity errors of each measurement. Within the specified -2 dBm to 29 dBm transmit power range, these errors are within ± 0.1 dB. The standard deviation of either the power sensor measurement and the backscatter power measurement is 0.04 dB if transmit power is within the specified -2 dBm to +29 dBm operating range. Several power measurements in the calibration process cancel, and the uncertainty in B from noise and nonlinearity is thus about the same as the RMS sum of the backscatter and power measurement uncertainties at 0.05 dB.

5.5.2 Tag Turn-on Power Level Errors

One source of error is truncation (round-off) in controlling the testbed transmit power level. The resolution is 0.1 dB. The error in P_{tx0} and therefore reference backscatter power is therefore uniformly distributed between 0 and +0.1 dB, with a bias of +0.05 dB (errors in dB behave approximately linearly here because they are so small). In post-processing, P_{tx0} and $P_{bs,ref}$ are therefore increased by +0.05 dB to remove the bias, so the maximum error is ± 0.05 dB and the standard deviation is ± 0.015 dBm.

5.5.3 Tag Detuning Sweeps

Measurements of a commercial tag are swept with distance from the testbed antenna mount in Fig. 5.9. The test environment is the anechoic chamber. Measurements are performed at about $\lambda/4$ increments across 2λ at 900 MHz, ensuring better than Nyquist sampling and a transmit power swept from 0 dBm to 25 dBm. The result is a plot of standard deviation (caused by combined noise, nonlinearity, and tag antenna detuning errors) and mean at each frequency.

Standard deviation at each point is as large as about 0.1 dB. Variance at each frequency is a combination of unknown thermal noise, tag detuning by non-ideal reflectors in the anechoic environment, nonlinearity errors, and uniformly-distributed noise in truncating P_{tx} to 0.1 dB (standard deviation 0.015 dB). The errors included in 5.5.1 suggests that thermal noise nonlinearity errors have combined standard deviation of 0.05 dB. These error sources and (1.23) give the remaining error source, tag antenna detuning,

Table 5.4: Testbed specifications, 860-960 MHz

Antennas	8 dBi LP patches
Antenna isolation	
Empty chamber load	> 45 dB
Detuning plate 1 m away	> 30 dB
P_{tx0} resolution	0.1 dB
Transmit power	-2 to $+29$ dBm
Mismatch errors	< 0.06 dB
IQ noise	-135 dBm/Hz
Tag backscatter sensitivity	-67 dBm
(50% detection rate)	

as having standard deviation of 0.08 dB.

Since the standard deviation caused by tag detuning is about 0.08 dB, the final expanded uncertainty estimate for tag antenna detuning errors is 0.16 dB. A more accurate estimate might might come from assuming a U-shaped distribution of the detuning error instead of a normal distribution, which would be appropriate because it is caused primarily by mismatch [65][66].

Theory in Chapter 3 predicted that B should be more stable in reflective environments than σ_{Δ}. Comparing tag antenna detuning in measurements of B, with 0.07 dB standard deviation, against the 0.45 dB standard deviation in σ_{Δ} measurements (from the results in 5.4) validates this premise. Each measurement uses the same linearly-polarized (LP) patch antenna in the testbed in the same environment, yet the errors from test zone reflections are about six times smaller for B as σ_{Δ}.

5.5.4 Combined Uncertainty

Table 5.4 lists performance parameters of the testbed illustrated in Fig. 4.9. Because P_{bs} is proportional to B, uncertainty in a tag's figure of merit contributes the same uncertainty to backscattered power estimates in link analysis.

The range of measurable B in the testbed depends largely on DUT placement in the test zone. Placing the tag co-polarized and in the main beam of the testbed antennas helps ensure turn-on and that backscatter is far above the -67 dBm testbed sensitivity. If $P_{tx0} < -2$ dBm, the tag must be moved farther from the testbed antennas to maintain specified measurement linearity. Tags tested by the author fall within $-35\,(\text{dBm})^2 < B < -15\,(\text{dBm})^2$, all measurable near the main beam of the 8 dBi patch antennas at 1 m.

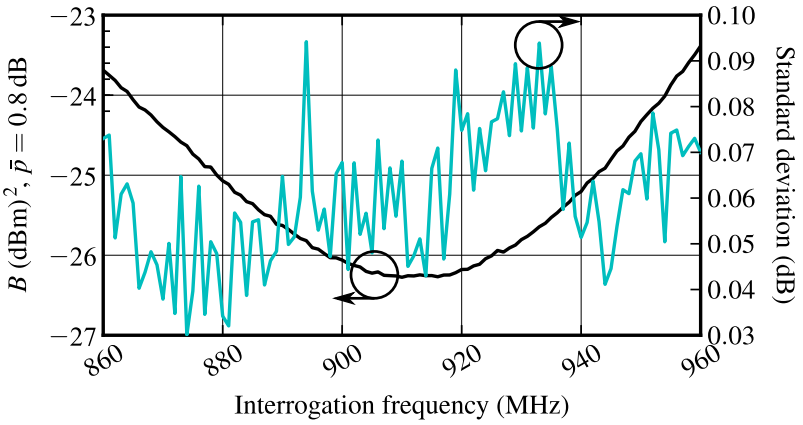

Figure 5.9: Mean and standard deviation of B measured at 8 positions in the test zone, from 60 cm to 120 cm (approx. 2λ to 4λ) away from testbed antennas in 7.5 cm (approx. $\lambda/4$) steps. At worst, standard deviation is below 0.1 dB, which we believe is dominated by noise.

Future tags with smaller P_{L0} will tend toward smaller B.

These results contribute to the estimate of combined uncertainty of B listed in Table 5.5.4. The remaining uncertainty estimates are based on uncertainty analysis documentation provided by the manufacturer of the power sensor and network analyzer, and with network analyzer verification impedance standards. The final combined uncertainty of ± 0.43 dB ($\pm 11\%$) is computed from their quadrature sum according to (1.23).

5.6 Validation of B Theory and Measurements

A tag built from a connectorized antenna and chip is shown in Fig. 5.10. It enables separate antenna and chip impedance measurements to validate the testbed accuracy and the theory regarding B without the complexity of probe and bonding parasitics. A commercially available tag chip package, marketed as compliant with [2], is soldered directly onto an SMA connector. Its input impedance is transformed to near 50 Ω within 860-960 MHz by single-stub matching. The antenna is a commercially available dipole tuned to 910 MHz with an integrated 2:1 balun.

On-tag circuit parameter measurements for B are not typically practical, but are helpful here to validate our model and testbed. Other work has addressed the problem of measuring the power harvesting impedance state [121, 122] with a network analyzer at a calibrated power level. Our network analyzer

Error source	*Expanded Uncertainty Estimate*
Reference modulation calibration	± 0.25 dB
Power measurements	± 0.25 dB
Multipath	± 0.16 dB
Coupler calibration	± 0.15 dB
Testbed nonlinearity and thermal noise	± 0.1 dB
Combined expanded uncertainty of B	± 0.43 dB ($\pm 10\%$)

Table 5.5: Expanded uncertainty estimates for reported B

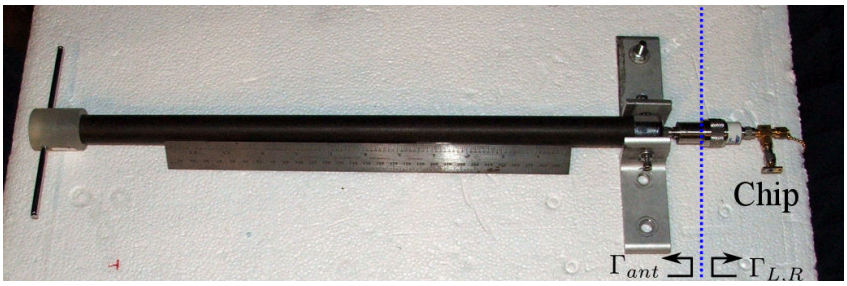

Figure 5.10: Connectorized "validation tag," stub-matched to 50 Ω. Measurements are calibrated at the dashed line. The 15 cm dipole has an integrated wideband 2:1 balun and $|\rho_R| < -10$ dB across 860-960 MHz.

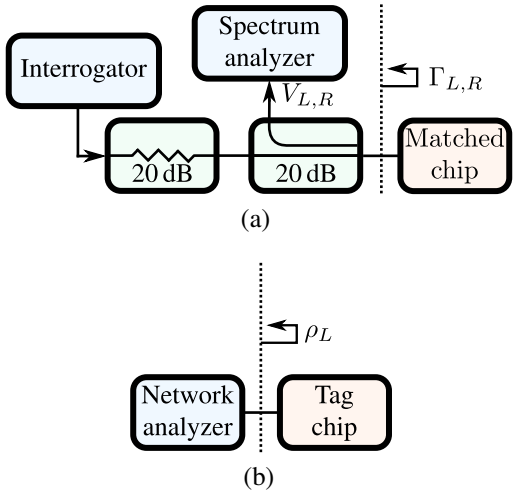

Figure 5.11: Measurement configuration for (a) ρ_R, which is calibrated against (b) ρ_L. Power at network interfaces (dotted lines) are calibrated at P_{tx0} by power sensor.

cannot excite or measure the time-varying reflective state ρ_R, so we constructed a custom reflectometer like [87, 123] calibrated against the power harvesting state.

First, the turn-on power into the chip network is determined by adjusting the power out of the interrogator in Fig. 5.11(a), and measuring power at the given interface with a peak power sensor as described in Section **??**. Measurements of ρ_{L0} and ρ_L, are performed at a fixed $\bar{p}$, fed with the $50\,\Omega$ network analyzer as a generator. The sensitivity of the chip network is then computed from a power sensor measurement at the coupler output P_{meas} with $P_{L0} = P_{meas}/(1 - |\rho_{L0}|^2)$, assuming that the coupler and reader are matched $50\,\Omega$ sources. P_{L0} was within 0.2 dB of -13 dBm across the band.

With ρ_{L0} known, reflections in each chip impedance state coupled into the spectrum analyzer can be compared to determine ρ_R. If the coupler and instruments are well matched, and the coupler has infinite directivity, the two reflection coefficients would be equal to the ratio of the complex IQ measurements V_R/V_L at a given forward-wave voltage V_{tx},

$$\frac{\rho_R}{\rho_L} = \frac{V_R/V_{tx}}{V_L/V_{tx}} = \frac{V_R}{V_L}. \tag{5.12}$$

We also used the thorough directional coupler analysis in [124] to account for coupler directivity and mismatch uncertainty at the chip interface:

$$\rho_R = \frac{d(V_R/V_L - 1) + (V_R/V_L)\rho_L}{1 - \rho_L\rho_c(V_R/V_L - 1)}, \tag{5.13}$$

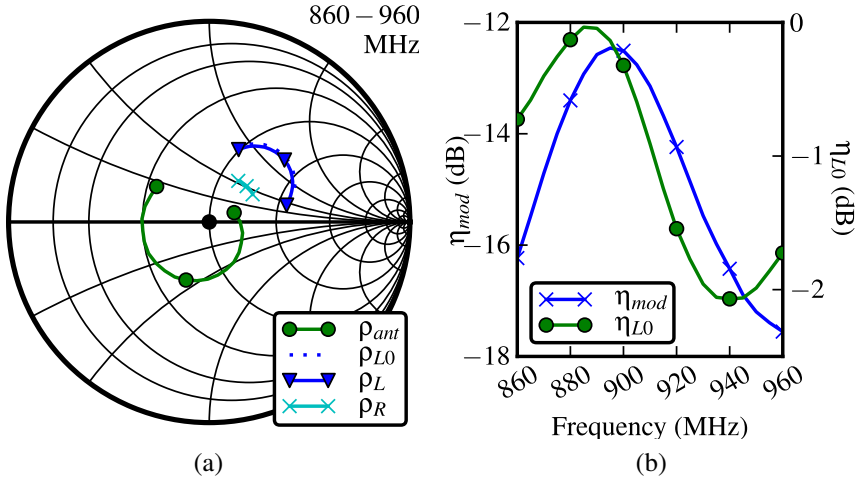

Figure 5.12: Measured efficiency of the tag pictured in Fig. 5.10, at turn-on and at $\bar{p} = 0.8\,\text{dB}$. Measured data shown in the 50Ω smith chart in (a) were used to compute matching and modulation efficiencies η_{L0} and η_{mod} in (b).

where d is the complex parameter determined from S-parameters such that the coupler directivity is $D = -20\log_{10}|d|$, and ρ_c is the reflection coefficient of the coupler at the network interface with the connectorized chip network. Measurements d and ρ_c calibrate the final ρ_R.

Computing $\eta_{mod}(\bar{p} = 0.8\,\text{dB})$ and η_{L0} from equations (3.6) and (3.9) with the circuit measurements gives the performance summarized in Fig. 5.12.

B predicted by (3.28) from these measurements are compared against testbed measurements in Fig. 5.13. Fig. 5.13(a) shows a frequency sweep with the validation tag on a polystyrene table ($\epsilon_r \approx 1$). Fig. 5.13(b) compares predicted B of the validation tag at three frequencies detuned by a $70\,\text{cm} \times 70\,\text{cm}$ aluminum plate. Circuit efficiencies were recalculated with measurements of the antenna reflection coefficient at each height. In all cases, the predicted B agree to within $\pm 0.35\,\text{dB}$, which is within the $\pm 0.5\,\text{dB}$ testbed uncertainty.

5.7 Summary

This chapter has compared the accuracy of radar cross Section and backscatter figure of merit measurements, and propagation to estimates of received backscatter power. The received power estimate is always at least slightly greater than the uncertainty of the tag backscatter metric used to estimate it. Un-

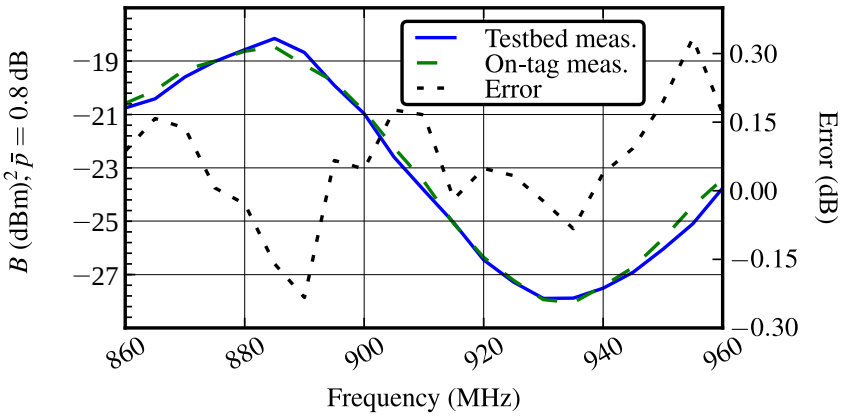

(a)

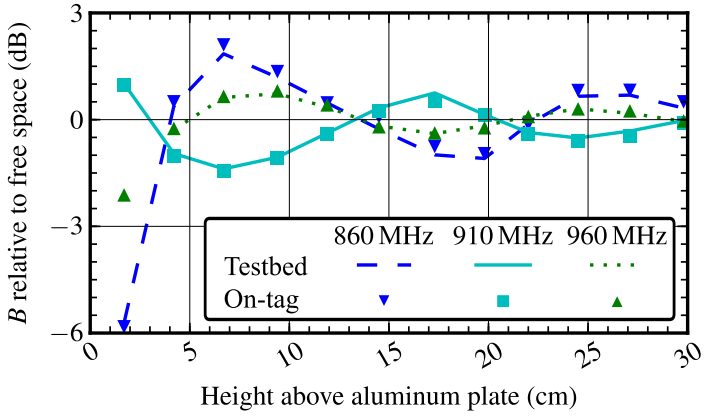

(b)

Figure 5.13: Validation of (3.28) by measurements of B. The setup detailed in Section **??** gives "testbed" B. "On-tag" B are from parameters in Fig. 5.12. Measurements in (a) an anechoic chamber normalize (b) detuning by an aluminum plate. All curves agree within the 0.5 dB testbed uncertainty.

certainties for radar cross Section measurements contribute negligibly to uncertainties in received power, as long as multipath is weak. In contrast, uncertainty of a minimum backscatter power bound estimate is the same as the measurement uncertainty of B. Thus, estimates of minimum backscatter power with measured B are always more accurate than estimates of backscattered power with σ_{Δ}.

D.G. Kuester, D.R. Novotny, J.R. Guerrieri, Z. Popović, "Simple Test and Modeling of RFID Tag Backscatter," *IEEE Trans. on Microwave Theory and Techn.*, vol. 60, no. 7, July 2012, pp. 2248-2258.

D.G. Kuester, D.R. Novotny, J.R. Guerrieri, "Simulated Link Relationship Measurements for Load-modulated RFID," *Proc. 2010 Antenna Measurement Techniques Association Symp.*.

Chapter 6

Test and Analysis for Reliable Passive UHF RFID Communication

You have my permission to play great.

Dr. William J. Stanley

6.1 Introduction

The previous chapters have proposed that B has strong advantages in simplifying theory and measurement of backscatter from passive UHF RFID tags. These advantages are meaningless, however, unless B can provide some useful insight into the behavior of a communication system. This chapter discusses how B applies to the simplest and most common type of UHF RFID, monostatic passive systems in the far field.

Even after 8 years of standardized operation, little guidance has been published on test or modeling of return links, but reliable systems have still been deployed. Moving forward, however, as readers and tags improve, system dynamics are moving reliability constraints away from the power harvesting performance and toward the return link.

The important effect of backscatter power on users is its effect on overall communication reliability.

Tag inventory rates are more readily observable and measurable than signal levels, and have a more direct impact on a system's practical utility. Thus, we need to be able to both 1) predict backscatter power seen by a reader, but also 2) translate backscatter power into information about inventory rates that are visible to users.

Predicting signal power in each link requires data about the communication devices and the radio environment. Devices can be measured and tested in a laboratory. Most systems are deployed indoors in industrial or commercial environments. These rooms have arbitrarily sized and positioned objects that act as radio wave scatterers and absorbers, causing signal attenuation (fading) that can prevent communication. Attenuation of transmit signal amplitude with strong scattering sources is modeled as a Rayleigh- or Rice-distributed random variable that has large variance.

The traditional approach to estimating wireless communication errors and throughput rates requires random fading channel loss estimates. Stochastic modeling of the backscatter return link is poorly understood. Indoor propagation of backscatter communication has only been studied in a few papers. Theoretical study has been performed primarily to support backscatter communication at 5.8 GHz [125, 126] rather than the more common 900 MHz. Monostatic UHF backscatter channel data were measured in [127], but strangely fit to a Rayleigh random variable (not Rayleigh squared) like a transmission link. Empirical propagation data are scant and difficult to compare. Other fading measurements and simulations do not separate the two links [34, 128–130], distorting the resulting fading. None of these have yet studied the performance of return links given the condition that the power harvesting link works correctly.

This chapter brings B into passive RFID system analysis to provide guidance on improving communication reliability through robust return links. The minimum backscatter power is shown to relate to a minimum expected inventory speed, depending on reader performance. Measurements of performance of 20 commercial RFID tags and 5 commercial RFID readers give an quantitative idea of realistic device performance. The minimum power predicted by B is then combined with device performance to demonstrate prediction of minimum inventory rate in a low-interference environment. The final result is a system design procedure to guarantee reliable inventory speed.

6.2 Reliability in an AWGN-limited Channel

A mathematically rigorous definition of reliability is beyond the scope of this thesis, but some discussion of general concepts in the context passive backscatter communication here will inform reader and system test strategy.

6.2.1 Remote Measurability

Consider a single communication frame consisting of one forward-link bit sequence and one return-link bit sequence. The probability that the tag chip is turned on by the reader is $P(\text{tag on})$; the tag is assumed to decode the reader data correctly as long as it is turned on. The probability of correctly decoding all of the return-link bit sequence is $P(\text{decode}) = 1 - \text{FER}$, where FER is the FER.

Ultimately, successful communication between the reader and tag requires that both 1) the tag is turned on and 2) the reader correctly decodes the protocol-compliant response from the tag. In terms of the link success probabilities,

$$P(\text{successful communication frame}) = P(\text{decode} \cap \text{tag on}) = P(\text{decode} \mid \text{tag on})P(\text{tag on}). \quad (6.1)$$

The conditional probability $P(\text{decode} \mid \text{tag on})$ is the probability that the reader correctly decodes the entire frame, given that the tag is on. Bayes's theorem relates this to the probability that the tag is on given that a frame is correctly decoded by the reader,

$$P(\text{decode} \mid \text{tag on}) = P(\text{tag on} \mid \text{decode})\frac{P(\text{decode})}{P(\text{tag on})}. \quad (6.2)$$

The probability that a reader could erroneously report a protocol-compliant bit sequence with a passing cyclic redundancy check (CRC) code is small (order of 10^{-2} for 5-bit codes or 10^{-5} for 16-bit codes), so $P(\text{tag on} \mid \text{decode}) \approx 1$; if the reader decodes a CRC-passing bit sequence, we can say with confidence that the tag is on.

Combining equations (6.1) and (6.2) leaves

$$P(\text{successful communication frame}) = P(\text{decode}) = 1 - \text{FER}. \quad (6.3)$$

Thus, analysis of backscatter communication error rates at the reader is sufficient to state overall performance of communication between a reader and a passive tag, since the latter is itself part of backscatter error prediction.

6.2.2 Error Rates and Inventory Rates

If a reader scans a pallet containing hundreds of tagged items, the goal of an inventory (query) operation is to detect all of the tags (scanning the entire volume of the pallet) as quickly as possible. Missed tag reads cause incomplete inventory data, or require slower manual scans that require human effort. Thus the most important inventory performance metrics are inventory rate and coverage volume or area. Ideally, the rate is as fast as possible, and the coverage volume inside the pallet approaches 100%.

Backscatter models become useful when the return (tag to reader) link limits system performance. The return link component of system performance depends critically on information about tag performance, propagation effects, and reader performance.

Assuming the channels (our shielded coaxial test circuits) are limited by AWGN, the BER of received BPSK backscatter is well known to be

$$\text{BER} = \frac{1}{2}\text{erfc}\sqrt{\frac{E_b}{N_0}}, \tag{6.4}$$

where erfc is the complementary error function. For low SNR ($E_b/N_0 \to 0$), each detected bit is 0 or 1 with equal propability, so BER approaches an error rate of 0.5. In terms of measured power for a reader operating at a uniform ambient temperature T_0,

$$\text{BER} = \frac{1}{2}\text{erfc}\sqrt{\frac{P_{bs}}{f_m}\frac{1}{k_B T_0(\text{NF}-1)}}, \tag{6.5}$$

with the Boltzmann constant $k_B \approx 1.38 \times 10^{-23}$ J/K, unitless receiver noise figure NF, and reference temperature T_0. Use of the AWGN approximation is only valid if the interfering carrier can be ignored, either by post-processing (in which case the receiver NF may be large) or by a carrier cancellation circuit (which also incurs some noise penalty).

In tests of fully assembled readers, we do not know BER, but can still estimate the relative noise figure between different readers and for different RF reader parameters. Define the reader's sensitivity

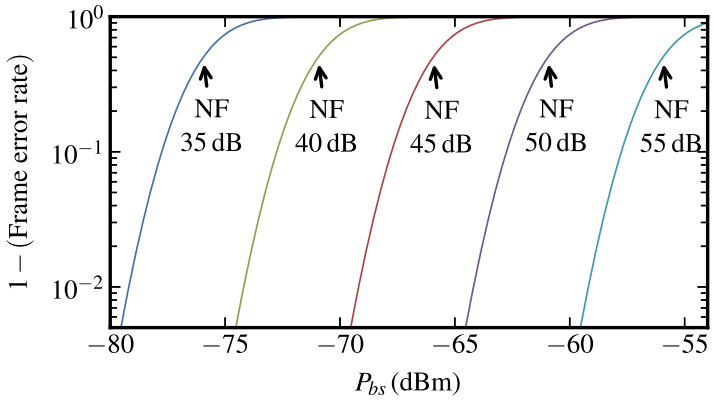

Figure 6.1: Frame error rates for various noise figure values, for a sequence of $N_b = 100$ bits.

P_{bs0} as the point at which some fixed BER is achieved. Assume as well that a given BER causes the same proportion of failed inventory frames, independent of RF modulation parameters. We can therefore compare noise figures from two measured P_{bs0} and known f_m:

$$\frac{\text{NF}^{(2)} - 1}{\text{NF}^{(1)} - 1} \approx \frac{\text{NF}^{(2)}}{\text{NF}^{(1)}} = \frac{P_{bs0}^{(2)}}{P_{bs0}^{(1)}} \frac{f_m^{(1)}}{f_m^{(2)}}. \tag{6.6}$$

This approximation is accurate only for large noise figures.

The FER, or probability that a bit sequence of length N_b has any bit errors, is

$$\text{FER}(N_b) = 1 - (1 - \text{BER})^{N_b}. \tag{6.7}$$

Some example curves comparing various values of NF for $N_b = 100$ (about the length of a 96-bit tag ID) are shown in Fig. 6.1. Each frame is transmitted with a CRC code so the reader can verify it received the correct data (and possibly correct it). In multi-frame return links with an average FER of $\overline{\text{FER}}$, the average return-link symbol rate, in symbols per second, is

$$\begin{aligned} \text{Symbol rate} = & f_m \times (\text{Backscatter channel occupancy}) \\ & \times (1 - \overline{\text{FER}}). \end{aligned} \tag{6.8}$$

Backscatter channel occupancy, average fraction of total time the tag spends backscattering, is between 0 and 1. This occupancy can be quite small; for small numbers of tags, a fixed reader's carrier power duty cycle is often about 25%, and a large fraction of this 25% may be used by the forward link and tag charge-up delays. Note that the symbol rate includes protocol overhead — data transmitted or received as part of the protocol that is not useful to the user.

All reader-to-tag transactions require some number of prerequisite frames N_f to perform anti-collision, to ensure that the reader only "talks to" and receives responses from one tag among many. Standard passive systems use "random-slotted collision arbitrartion," for which N_f is a random variable. If readers must transmit an average number of frames $\overline{N}_f$ to perform an operation, each having an average number of bits $\overline{N}_b$, then the average inventory rate, in inventories per second, is

$$\text{Inventory rate} = \frac{\overline{N}_f}{\overline{N}_b} \times (\text{Symbol rate}). \tag{6.9}$$

Its inverse, the average inventory time, is simply $1/(\text{Inventory rate})$.

Each of $\overline{N}_f$, $\overline{N}_b$, $\overline{\text{FER}}$, vary with noise and interference at the reader receiver, the number of tags, and relative backscatter power between the tags. Readers usually use proprietary anticollision algorithms, however, so these dependences are difficult to simulate in third-party tests. In this work, we therefore focus on direct measurement of inventory rate.

The development of equations (6.5-6.9) give all of inventory rate, symbol rate, $(1 - \text{FER})$, and $(1 - \text{BER})$ as proportional to each other, thus

$$\text{inventory rate} \propto 1 - \frac{1}{2}\text{erfc}\sqrt{\frac{P_{bs}}{f_m}\frac{1}{k_B T_0(\text{NF}-1)}}. \tag{6.10}$$

For very strong P_{bs}, the erfc term goes to zero; thus, we can define relative inventory rate as

$$\text{Normalized inventory rate} = \frac{\text{inventory rate}}{\text{maximum inventory rate}} = 1 - \frac{1}{2}\text{erfc}\sqrt{\frac{P_{bs}}{f_m}\frac{1}{k_B T_0(\text{NF}-1)}}. \tag{6.11}$$

The normalized inventory rate decreases monotonically with decreasing P_{bs} (assuming there is no counterproductive adaptive behavior by the reader). Commercial readers do not report BER, so it is convenient to define reader sensitivity in terms of the normalized rate. We somewhat arbitrarily choose a normalized rate of 50% as the minimum bound:

$$0.5 = 1 - \frac{1}{2}\text{erfc}\sqrt{\frac{P_{bs0}}{f_m}\frac{1}{k_B T_0(\text{NF}-1)}}. \tag{6.12}$$

The monotonicity of inventory rate with P_{bs} also predicts the existence of a minimum rate $\min(\text{normalized inventory rate})$ at the predicted minimum backscattered power $\min[P_{bs}]$:

$$\min(\text{Normalized inventory rate}) = 1 - \frac{1}{2}\text{erfc}\sqrt{\frac{\min[P_{bs}]}{f_m}\frac{1}{k_B T_0(\text{NF}-1)}}. \tag{6.13}$$

If inventory performance at the receiver sensitivity power level of the reader is defined as adequately reliable for a certain application, a simple comparison of $\min[P_{bs}]$ (from transmit power and tag performance) against P_{bs0} (from reader performance) predicts communication reliability:

$$\begin{aligned} &\min[P_{bs}] > P_{bs0} : \text{Adequate reliability is guaranteed in an AWGN channel} \\ &\min[P_{bs}] < P_{bs0} : \text{Adequate reliability is not guaranteed in an AWGN channel} \end{aligned} \tag{6.14}$$

This is also subject to the same limitations as the estimate of $\min[P_{bs}]$, namely that channel losses are linear, and that the tag is passive.

Thus, even though communication logic and protocol parameters in the reader determine the precise inventory rate, the normalized inventory rate provides a simple way to relate software-reported performance of a reader to physically measurable power levels.

6.3 Reader Tests

The previous section demonstrated that overall communication reliability is measurable with a reader if it provides information about tag detection rates.

Benchtop lab tests were performed at ambient 20° C $\pm$ 1° C. Each reader was configured to transmit at full power for 1 hour in order to reach thermal equilibrium. Results should therefore suggest reader performance in a realistic deployment during extended use.

The 5 example DUTs are commercial off-the-shelf readers that are certified as compliant with either or both of EPC Class-1 Generation-2 and ISO 18000-6C. None of them include detailed manufacturer-specified RF performance test data, except maximum transmit power of at least 30 dBm. Each DUT was configured to transmit between 29.5 dBm and 30.0 dBm peak power, verified by coupled measurement with a power sensor.

All RF signals are transmitted coaxially to shield from interference. Communication between a PC and each reader was performed over a crossover 100 Mb/s ethernet link with the low-level reader protocol (LLRP), a standardized TCP/IP networking protocol for control and monitoring of fixed UHF RFID readers. This allowed all tests to be performed with the same commands. Each offered different fixed combinations of C1G2 signal parameters.

DUT	Data rate (kbps)	BLF/data rate spacing	Tari (us)	Sensitivity (dBm)
1	160	1	12.5	-70.8
	256	4	25	-77.3
	256	8	25	-80.1
	640	1	7.14	-69.3
2	40	1	6.25	-78.2
	170.6	8	20	-80.8
	256	8	25	-80.1
	274	4	20	-78.2
3	31.25	8	25	-73.5
	37.5	8	25	-67.6
	40	1	25	-67.2
	62.5	4	25	-71.8
	75	4	25	-66.5
	75	4	25	-73.5
	80	2	12.5	-74.2
	125	2	25	-67.3
	400	1	6.25	-67.4
4	250	$\{1,2,4,8\}f_m$	12.5	-70.2
	640	f_m	6.25	-64.8
5	(auto)	(auto)	(auto)	-65.0

Table 6.1: Measured reader sensitivity for 5 commercial fixed readers at 33 dBm with various operating modes

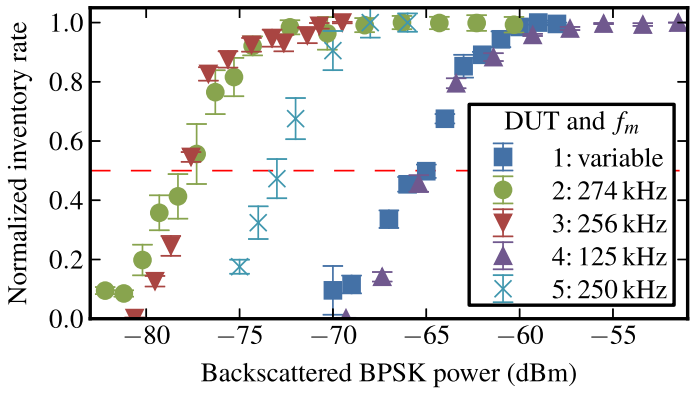

Figure 6.2: Measured inventory speed swept with P_{bs} at each reader's mode nearest $f_m = 250$ kbps. In all cases, the normalized inventory speed fell from 90% to 10% over a backcsattered power range of 7 dB to 10 dB.

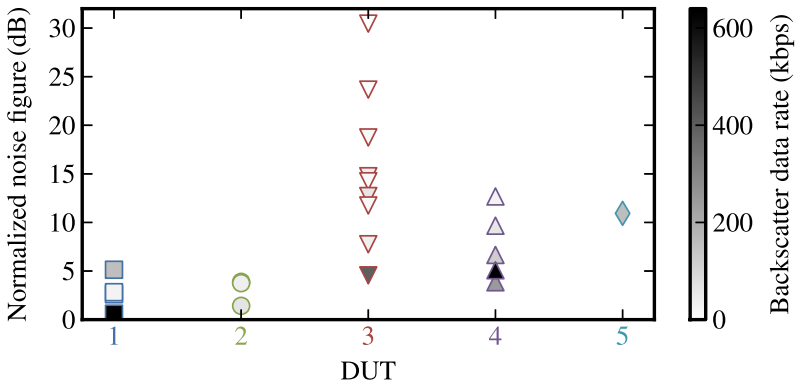

Figure 6.3: Noise figure performance of tested RF modes of each reader, shown with base link frequency (i.e., the encoded signal switching rate, or first sideband separation from the carrier). Readers' noise figures tended to be best at high BLF, except reader 2.

Raw data are listed in Table 6.3. The resulting sensitivity levels are in the range -80 dBm to -65 dBm. These were computed by sweeping the reference backscatter from low to high and determining the 50% normalized inventory speed. Example curves swept with P_{bs} are given by 6.2. The rate of decay suggests that definitions of P_{bs0} for between 90% and 10% can cause 7 dB to 10 dB difference in the measured sensitivity. Thus, compared to the specified 50% normalized inventory rate, redefining sensitivity at 90% or 10% could change P_{bs0} by 3.5 dB to 5 dB relative to values given in Table 6.3.

Data are shown as relative noise figures in Fig. 6.3 by applying (6.6) to each reader in Table 6.3. If baseband digital filtering in each operating mode have been optimized, the noise figure should stay about the same. Readers 4 and 5 each have noise figures that vary by at least 10 dB; the others vary by less than 5 dB. All except one of these readers exhibits the best noise figure at its highest data rates.

Discussion of reader testing so far has focused on AWGN-limited channels, but in environments with more than one RFID system, tag interference is a significant concern, multiple tags backscattering simultaneously may interfere with each other. Figure 6.4 shows normalized inventory rate swept with SIR, where interference is BPSK FM0 `FFFF....`. The interfering backscatter is at the same data rate as the correct -40 dBm BPSK tag response. Most readers operated normally for SIR greater than 5 to 10 dB. Thus, the low-interference channel assumption of this chapter appears be meaningful for most readers for interference at least 10 dB weaker than the backscatter signal.

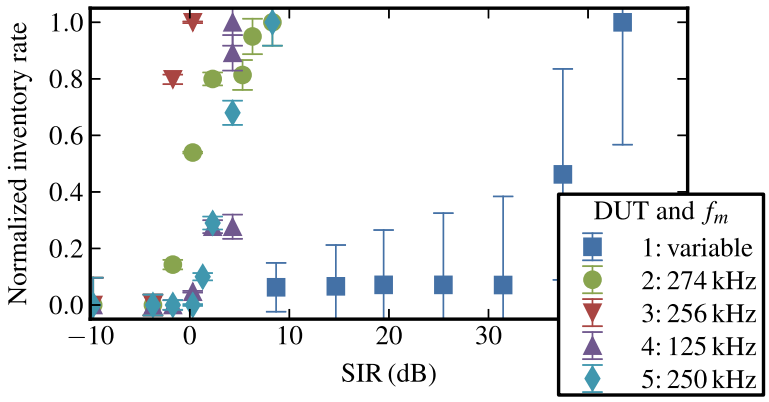

Figure 6.4: Measurements of reader rejection of BPSK interference (e.g., from other tags). Modulation power is swept for the interference, which is BPSK FM0 `FFFF...` repeated at the tag backscatter data rate. The signal is fixed at -40 dBm responding at the backscatter data rate determined by the reader. Reader 1 exhibits problems even at very high SIR.

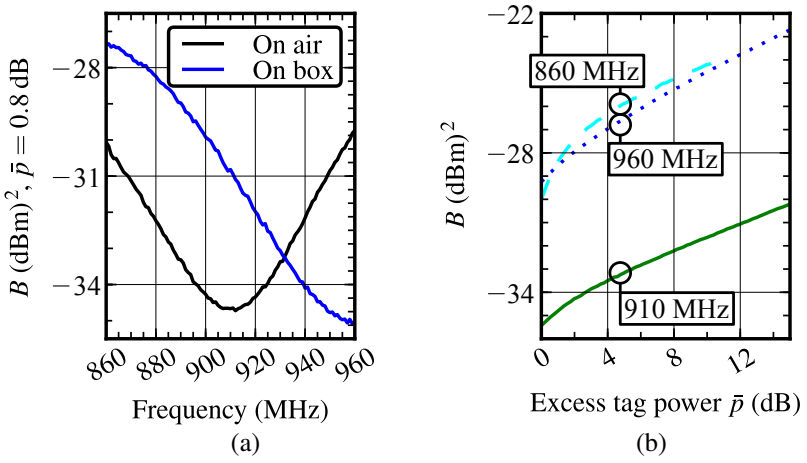

Figure 6.5: Measurements of B for a commercial passive tag sample measured in an anechoic environment swept with (a) frequency (placed on polystyrene foam and a wooden box) and (b) power (on polystyrene).

6.4 Tag Tests

6.4.1 Tests under Detuning Conditions

Measurements of B of a commercial tag performed in an anechoic chamber are shown in Fig. 6.5 swept with frequency and linearity. This tag is the subject of tests for the remainder of this section.

Operation in practice will include fading effects. Previous experiments into an equivalent parameter [113] already suggest only slight variations. However, these measurements use P_{tx} and P_{bs} from a commercial reader's transmit power setting and received signal strength indicator (RSSI), for which we expect large errors (a few dB) from receiver nonlinearity and thermal drift. Therefore, with a focus on communication testing in reflective environments instead of sensing, and with the repeatable and linear testbed demonstrated by Fig. 5.9, we empirically investigate the extent of this detuning error.

Consider the effects of fading manifest in backscatter loss normalized to free space behavior. The theory developed in Chapter 3 predicts that B should only depend on the antenna impedance, Z_3, not loss. In contrast, the backscatter loss measurement depends on *both*. Therefore, B should be less sensitive to fading effects than the backscatter loss. Figure 6.6 compares these near an aluminum plate in an anechoic chamber. Fading normalization is against measurements at the same tag position and operating point $\bar{p}$ but without the aluminum plate. B converges to within 1 dB (25%) of its free space value beyond 15 cm

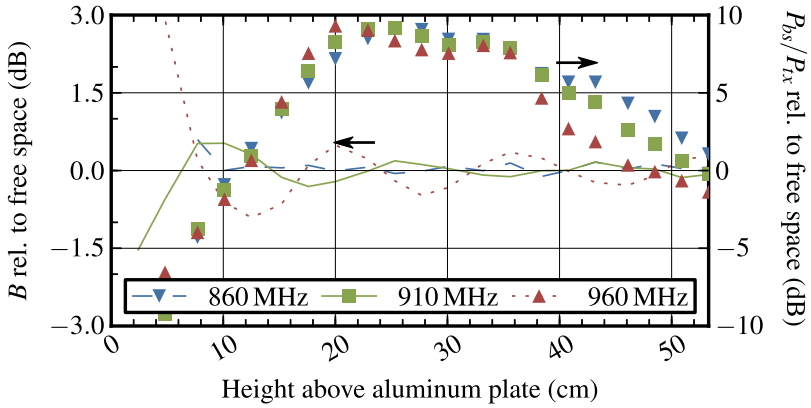

Figure 6.6: Comparison of the stability of B against backscatter power loss P_{bs}/P_{tx} for the passive tag of Fig. 6.5 above an aluminum plate.

	Anechoic chamber	Storage room
RCS (σ_Δ)	1.5 dB	$\tilde{1}$5 dB
Figure of merit (B)	0.1 dB	$\tilde{1}$ dB

Table 6.2: Worst-case contribution of multipath and detuning to σ_Δ and B uncertainty

above the plate. In contrast, fading is still 10 dB at 30 cm above the plate.

As a "realistic" example of this stability, tests were performed in a cluttered storage room. Ten positions were chosen for testing on top of metal scatterers strewn across a shelf, shown along with the tagged objects in Fig. 6.7. The tag is attached atop each object in Fig. 6.7(c), 15 cm above shelf clutter. Results are given in Fig. 6.8. At this range, as in the anechoic chamber near the aluminum plate, B is stable to within 1 dB of its free space value.

6.4.2 Minimum Power Bounds from Measurements

We now have enough test data to bound monostatic backscatter from the tag. Inserting results from Figs. 6.5 into (3.31) gives contours for the bounds in Fig. 6.9.

Figures 6.8 and 6.6 give us an idea for the stability of $\min[P_{bs}]$. If foreign objects are kept separated by at least 15 cm from the tag, the minimum may be stable to within 1 dB of the indicated value. For a more conservative "worst-case" estimate, a "detuning margin" greater than 0.8 dB can be subtracted from the contour in Fig. 6.9. More specific tests for stability of $\min[P_{bs}]$ can be tailored by application.

Uncertainty estimates discussed in this chapter are compared in Table 6.2. Since transmit power can be measured accurately, uncertainty in the minimum backscatter power from the backscatter figure of merit is unconditionally the same as that of the figure of merit. When careful measurements are performed as discussed in Chapter 4, B is much more stable than σ_Δ in either environment. Uncertainty associated with the minimum backscatter power bound from B is also unconditionally smaller than an backscatter power estimate based on σ_Δ.

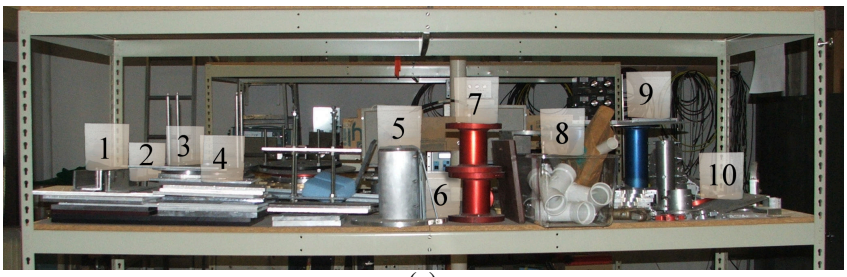

(a)

(b)

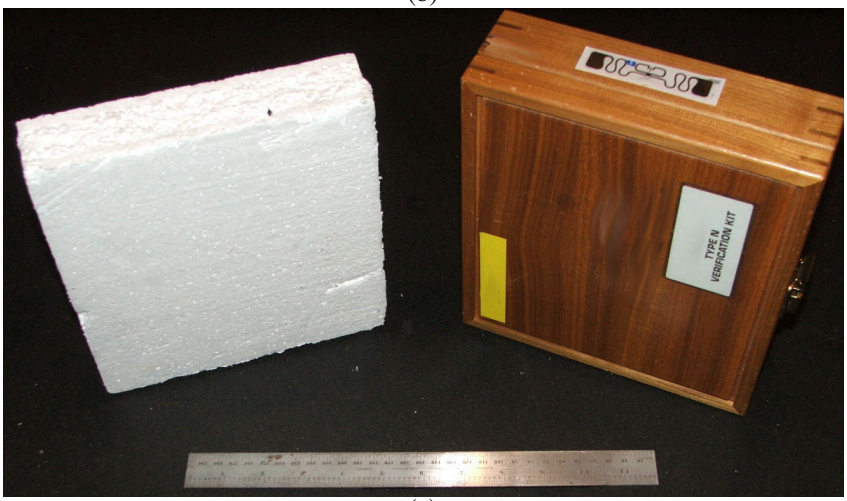

(c)

Figure 6.7: A shelf covered in metallic antenna mounting equipment to test detuning shown (a) from behind, with the 10 test positions for the tagged object and (b) from the side. Tests were performed on two tagged objects shown in (c): a polystyrene block (left), and a wooden test equipment box (right).

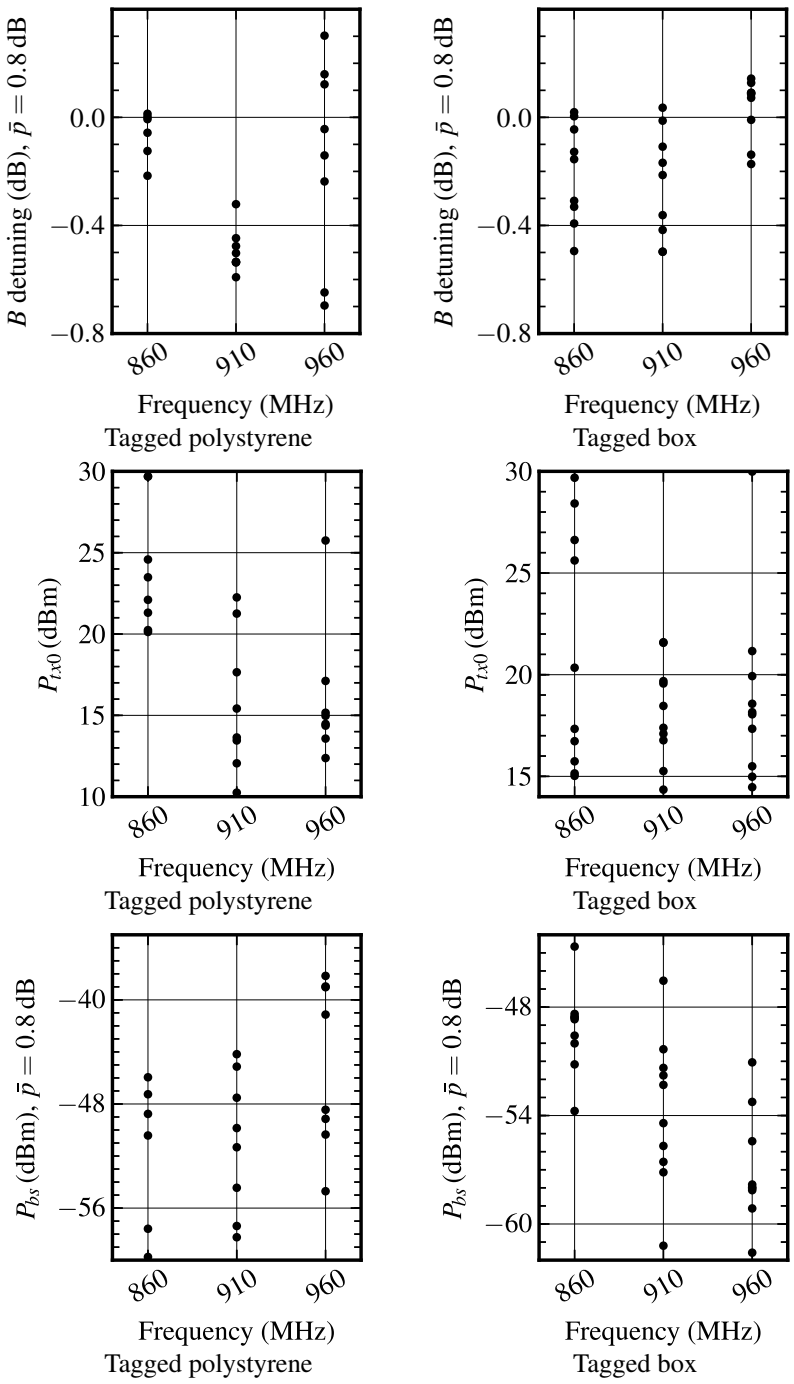

Figure 6.8: Measured (a) detuning effects in the storage room of Fig. 6.7, with the tag placed on polystyrene foam and wood, normalized to measurements in a semi-anechoic chamber. Measurements of (b) tag turn-on power and (c) backscattered power in the same positions are plotted to demonstrate the enhanced stability of (a).

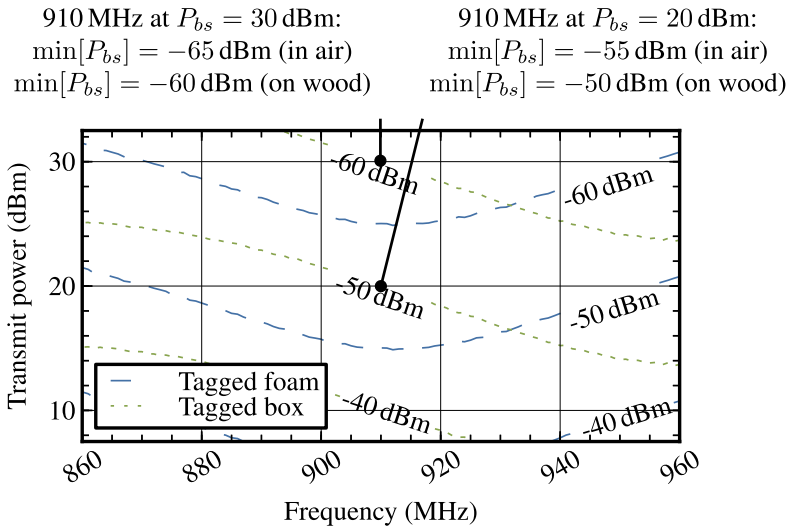

Figure 6.9: Frequency dependence of minimum backscattered power from the tag sample into a monostatic reader in any environment, highlighting two example points. Estimates use measured B from Fig. 6.5 with 2.5 dB margin to account for measurement uncertainty and tag impedance detuning effects by the environment.

Table 6.3: Tag sample distribution

Tag	Inlay Make	Inlay size (cm^2)	Chip	Age (years)
1	1	11	A	3
2*	2	12	B	6
3‡	3	6.8	A	1
4*‡	3	2.0	A	2
5	3	63	C	5
6	4	12	A	3
7	5	29		4
8	6	88		3
9†	4	10	A	3
10	7	12		4
11	8	48	D	4
12	3	19	A	5
13*	9	46		5
14	9	6.0		5
15*†	9	37		5
16	6	92		5
17	3	23	E	0
18	3	11	F	1
19	3	12	A	1
20	3	53	E	1

* No response up to 33 dBm transmit power
† Distorted backscatter waveform
‡ Tuned for operation on plastic or glass

6.4.3 Performance Trends

Samples of twenty different passive EPC Class 1 Gen 2 inlays were selected arbitrarily for testing. They represent 9 different inlay manufacturers, and at least 6 different tag chip products from 3 different chip manufacturers. The tags' ages vary from 0 to 6 years. The distribution of these parameters, as well as the printed antenna surface area of each inlay, are outlined in Table 6.3. The trade names of the manufacturers and products are not disclosed, because of restrictions in the author's institution. The tests may not have been performed with each tag tuned precisely on an optimal dielectric for a fair comparison.

The tags are grouped into three broad categories related to their size and antenna properties. "Small" tags (with area less than $10\,\mathrm{cm}^2$) are based on dipoles, but with large bends to raise the input impedance for better chip matching. Many of these tags were also designed for operation on dielectric materials; these tags were mounted on plexiglass. "Medium" sized tags ($10\,\mathrm{cm}^2$ to $25\,\mathrm{cm}^2$) are similar to half-wavelength dipoles, but with smaller bends that match to the tag chip while maintaining a more linear polarization. Most "large" (more than $25\,\mathrm{cm}^2$) tag antennas were effectively two "medium" antennas oriented orthogonally for dual polarization. During tests, tag antennas were oriented as nearly co-polarized with the testbed's transmit and receive antennas as possible.

Tags were interrogated with the protocol parameters listed in Table 4.4.1. The tag backscatter measurement is meaningful only with enough power to turn on, so measurements at each frequency are reported only at or above the minimum turn-on power for the tag. In linearity tests, power levels are reported as relative to this power level, in part to fit different results on the same axes.

Several of the tags were marked in Table 6.3 as exhibiting "no response" or "distorted backscatter," anywhere across 860-960 MHz in the position pictured in Fig. 5.3 up to 33 dBm transmitter power. Additional tests of tags 2 and 15 closer to the testbed antenna still result in no response. Tags 4 and 13, however, did respond to the stronger field closer to the antenna; a different dielectric may have resulted in a better chip-antenna match in the tag and a measureable response at 1 m. The response from Tag 9 was inconsistent and did not exhibit clear discrete scattering states. On close examination of the tag (and other samples of the same model) the authors observed brown discoloration at the chip-to-antenna bond, and believe it may have degraded.

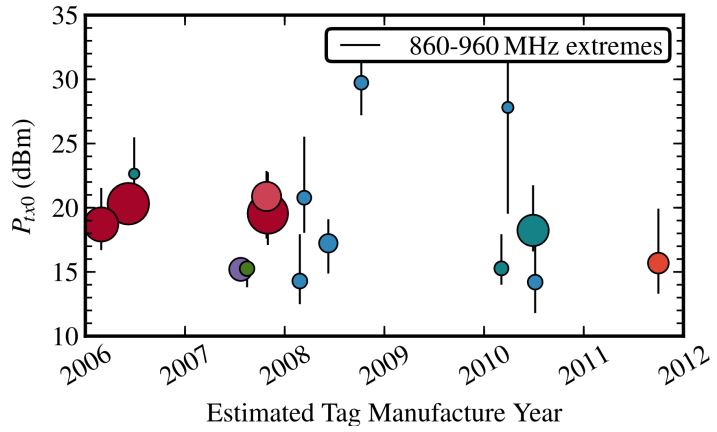

Figure 6.10: Minimum transmit power to turn on various tags, P_{tx0}, each at fixed 1.3 m from the 8 dBi LP patch antenna. The size of each circle is proportional to the size of the tag. The black line at each point shows the range of measured B across 860-960 MHz. Each color represents a different manufacturer.

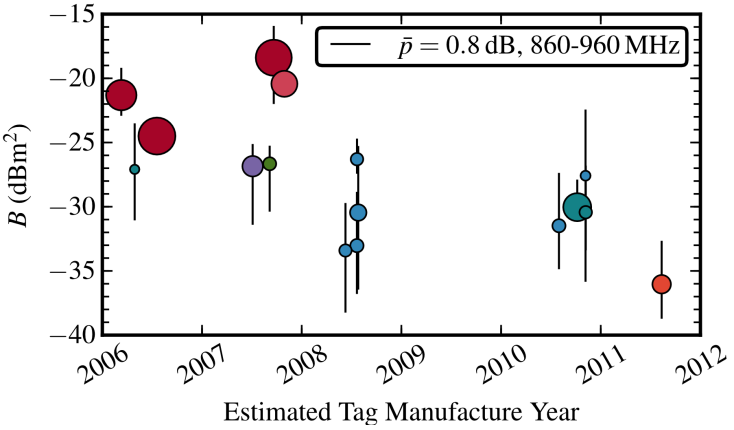

Figure 6.11: Measurements of B for 20 sample tags, measured in an anechoic chamber plotted against estimated year of manufacture. The size of each circle is proportional to the size of the tag. The black line at each point shows the range of measured B across 860-960 MHz. Each color represents a different manufacturer.

Measurements of B from these tests, plotted in Fig. 6.11 against estimated year of manufacture, give some context on expected B. Because tag chips' P_{L0} has fallen, B is falling too — roughly 10 dB in 5 years. At $P_{tx} = 30$ dBm, the newest tag would return a minimum $\min[P_{bs}] = -68$ dBm (including the 2.5 dB detuning margin). According to Fig. 6.2, Reader 2 would detect this tag at a mere 3% of its maximum rate. If future tags continue the trend of Fig. 6.11, the return link will soon become the dominant constraint upon passive RFID communication.

6.5 System Reliability and Design

Figure 6.12 shows an algorithmic approach to system design for ensuring reliable communication in AWGN environments. When reliability problems arise, three methods are given for guaranteeing inventory speed reliability with the deterministic $\min[P_{bs}]$ bound: 1) improving reader sensitivity, P_{bs0}, 2) improving tag modulation efficiency, η_{mod}, or 3) reducing transmit power, P_{tx}. The third option may only be viable when there is excess link margin available in the power harvesting link. If all of these fail, then diversity schemes (antenna diversity, frequency diversity, etc.) may be used to improve the odds of successful inventory, though these methods do not realize firm deterministic bounds.

6.5.1 Link Analysis Example and Validation

A simple test was run to validate the performance bounds. Readers 2 and 4 transmitted $P_{tx} = 33$ dBm into the well-matched LP patch antenna, operating in modes with sensitivities $P_{bs0} = -80.1$ dBm and $P_{bs0} = -64.8$ dBm. At turn-on near 910 MHz, the tag characterized in Fig. 6.5 has $B \approx -34$ dBm^2, so at 33 dBm transmit power the minimum backscatter power bound is $\min[P_{bs}] = -34$ dBm$^2 - 33$ dBm $= -67$ dBm. According to the curves in Fig. 6.2, at -67 dBm, reader 2 should operate at near 100% of its maximum inventory rate; reader 4 may slow to as little as 15% of maximum.

Readers 2 and 4 were tested with the tag at various reader-antenna separations r at 1 m above a concrete floor. As expected, reader 2 maintained full inventory speed, except near maximum range, where intermittently the tag did not turn on at all (a forward link failure); the return link has maintained full operation. Reader 4, as expected, does not maintain fully reliable communiation. The forward link

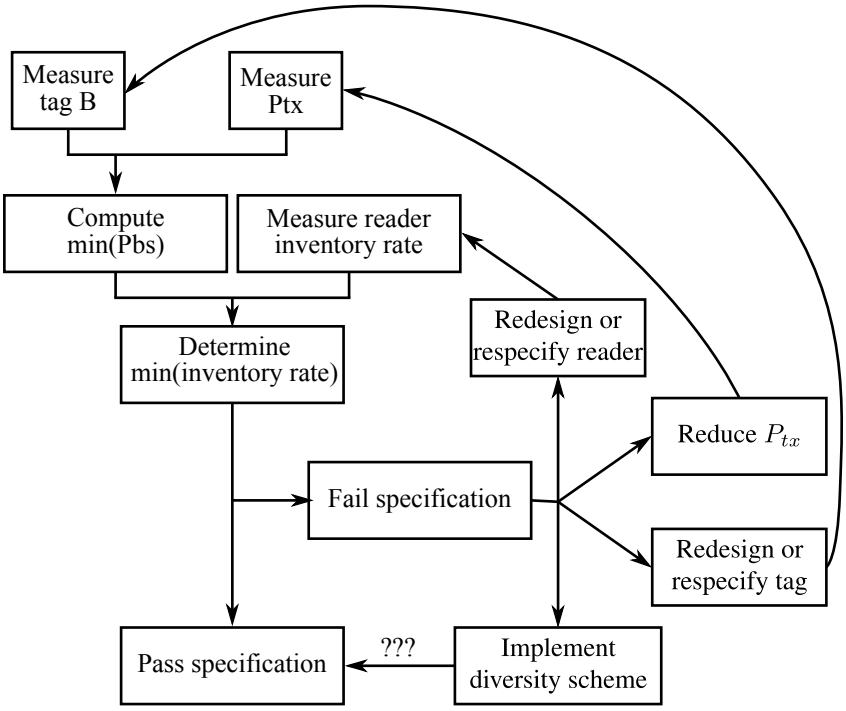

Figure 6.12: Workflow to optimize system design for reliable backscatter communication in low-interference channels. If tag and reader circuit performance optimization and transmit power reduction are inadequate, then stochastic diversity schemes can be a fallback option to improve reliability.

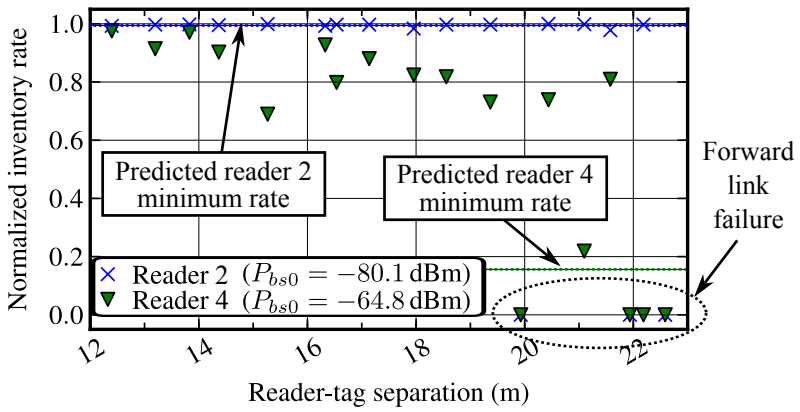

Figure 6.13: Inventory rates reported in communication with two of the readers in Table. 6.3, measured in a warehouse environment. Rates are averaged across all channels that contain detected tag responses.

failed for reader 4 at the same distances as with reader 2.

At present, based on the sensitivity of readers as listed in Table 6.3 and the sample of tag performance in Fig. 6.11, it is clear that return link reliability can be guaranteed in AWGN environments by either careful reader design or selection. In these cases missed reads are likely a result of the tag absorbing too little power.

If the trend illustrated in Fig. 6.11 continues, tag B and therefore $\min[P_{bs}]$ will continue to fall, and return link reliability will become a more significant problem. Taken to an extreme, if $\min[P_{bs}]$ falls below reader sensitivities, then backscatter communication will limit communication performance in *most* RFID systems.

6.6 Summary

With validated theory and measurement ability, we can now analyze system behavior of off-the-shelf commercial readers and tags. Use of the minimum backscattered tag power bound predicted in Chapter 3, coupled with information about the sensitivity and interference rejection of the reader, allows system designers to determine whether channel diversity schemes are necessary. Calibrated measurements of 20 different commercial tags suggest long-term trends of increasing communication range but lower inventory rate between fixed readers and passive tags. Finally, the application to RFID culminates with a system design approach for ensuring reliable backscatter communication.

The tag measurements have also been published as part of the following peer-reviewed publications:

D.G. Kuester, D.R. Novotny, J.R. Guerrieri, Z. Popović, "Simple Test and Modeling of RFID Tag Backscatter," *IEEE Trans. on Microwave Theory and Techn.*, vol. 60, no. 7, July 2012, pp. 2248-2258

D.G. Kuester, D.R. Novotny, J.R. Guerrieri, Z. Popović, "Testing Performance Trends of Passive UHF RFID Tags," *Proc. 2011 IEEE Intl. Conf. on RFID Tech. and Applications* pp. 401-409.

Chapter 7

Conclusion

> 'Twas this vain Idolizing of Authors, which gave birth to that silly vanity of *impertinent citations*; and inducing Authority in things neither requiring, nor deserving it.
>
> Joseph Glanvill, *Vanity of Dogmatizing* (1661)

This thesis solves the problem of inexpensive performance test and characterization of passive backscatter communication. The approach examines link behavior in realistic environments, measurable performance metrics to characterize this behavior, and testbed design for accurate test and measurement of these parameters. The ultimate goal is to improve system design practices and support test standard development.

The principal result is a new theory of backscatter signaling based on linear microwave network theory that is suitable for metrology, test engineering, and link analysis. The parameter is simple and clearly defined for measurement and link analysis suitable in any linear propagation environment including free space, line-of-sight, and deep fading. The theory is built on a clearly defined and justified BPSK definition for arbitrary binary-modulated backscatter power. A measurable figure of merit is developed that gives an absolute lower bound on the modulation power in backscatter received by monostatic transceivers from passive transponders.

The concepts are applied to passive monostatic UHF RFID operating in the far-field, which is the most common use of passive backscatter. Measurements of commercial RFID readers and tags validate the theory and confirm the utility of the figure of merit defined by this thesis. This becomes the basis for a simple new method for specifying RFID device performance to maximize communication speed by optimizing the backscatter link. The approach developed here is expected to gain importance as passive RFID communication range increases, where the backscatter link becomes weaker.

7.1 Thesis Contributions

Definitions for backscattered power and other signal characteristics were refined in the context of the received backscatter signal at the reader. To the best of the author's knowledge, this has not been done in the past in a detailed way. Usually, authors just state a normalization factor, without justification, leading to varying definitions across the literature. The contributions related to this topic are described in Chapter 2 and accepted for publication in IEEE Antennas and Wireless Propagation letters:

(1) D.G. Kuester, D.R. Novotny, J.R. Guerrieri, Z. Popović, "Baseband Voltage and Power in Load-Modulated Digital Backscatter," *IEEE Antennas and Wireless Propagation Lett.*, accepted for publication.

The author considered worst-case analysis of backscatter from passive radio frequency identification (RFID) tags. The basis is the figure of merit B to relate link power at reader ports to tag circuit parameters. A minimum bound for received monostatic backscatter can be determined by inspection from measured B. The bound is general for narrow-band signals in any causal linear propagation. For an assembled tag, this minimum varies only with reader transmit power, tag antenna tuning, and chip power sensitivity of different commands. To validate this model, the author proposes a backscatter calibration device to enable measurement with estimated uncertainty ± 0.5 dB. We also demonstrate how the minimum bound informs reader sensitivity specification to help ensure reliable inventory performance. The contributions related to this topic are described in Chapters 3-6, published in the IEEE Trans. on MTT:

(2) D.G. Kuester, D.R. Novotny, J.R. Guerrieri, Z.B. Popović, "Simple Test and Modeling of RFID

Tag Backscatter," *IEEE Trans. on Microwave Theory and Techn.*, vol. 60, no. 7, July 2012, pp. 2248-2258.

Power calibration is an important part of overall RFID system calibration. This kind of calibration was developed for digitally modulated backscatter for the first time in this thesis. Contributions on this topic are detailed in Chapters 4 and 5. The effect of multipath on digital backscatter communication calibrations performed over the air in multipath environments was also considered for the first time. The work was published in recent conference proceedings from the IEEE EMC, IEEE RFID, and IEEE RFID-TA:

(3) D.G. Kuester, D.R. Novotny, J.R. Guerrieri, "Forward and Reverse Link Constraints in UHF RFID with Passive Tags," *Proc. 2010 IEEE Intl. Symp. on Electromagnetic Compatibility*, pp. 680-685.

(4) D.G. Kuester, D.R. Novotny, J.R. Guerrieri, R.H. Direen, Z. Popović, "Reference Modulation for Calibrated Measurements of Tag Backscatter," *Proc. 2011 IEEE Intl. Conf. on RFID*, 12-14 Apr 2011.

(5) D.G. Kuester, D.R. Novotny, J.R. Guerrieri, Z. Popović, "Testing Performance Trends of Passive UHF RFID Tags," *Proc. 2011 IEEE Intl. Conf. on RFID Tech. and Applications*, pp. 401-409.

7.2 Other Contributions

This thesis consists solely of material that the author published as main author, but he also collaborated extensively within NIST on other subjects.

The high transmit power of fixed readers makes interference problems related to RFID a serious concern. Publications on this topic are listed below:

(6) K.A. Remley, M.R. Souryal, W.F. Young, D.G. Kuester, D.R. Novotny, J.R. Guerrieri, "Interference Tests for 900 MHz Frequency-Hopping Public-Safety Wireless Devices," *Proc. 2011 IEEE Symp. on Electromagnetic Compatibility*, pp. 497-502, 14-19 Aug. 2011.

(7) D.R. Novotny, J.R. Guerrieri, D.G. Kuester, "Potential interference issues between FCC part 15

compliant UHF ISM emitters and equipment passing standard immunity testing requirements," *IEEE Electromagnetic Compatibility Magazine*, vol. 1, no. 3, pp. 92-96, Sept. 2012 (**invited**).

(originally from *Proc. 2009 IEEE Intl. Symp. on Electromagnetic Compatibility*, pp. 161-165, 17-21 Aug. 2009).

(8) M.R. Souryal, D.R. Novotny, D.G. Kuester, J.R. Guerrieri, K.A. Remley, "Impact of RF Interference between a Passive RFID System and a Frequency Hopping Communications System in the 900 MHz ISM Band," *IEEE Electromagnetic Compatibility Magazine*, vol. 1, no. 3, pp. 97-102, Sept. 2012 (**invited**)

(originally from *Proc. 2011 IEEE Symp. on Electromagnetic Compatibility*, pp. 497-502, 14-19 Aug. 2011).

(9) D.R. Novotny, J.R. Guerrieri, D.G. Kuester, "A Reference Modulated Scatterer for ISO 18000-6 UHF Tag Testing," *IEEE Electromagnetic Compatibility Magazine*, vol. 1, no. 3, pp. 103-106, Sept. 2012 (**invited**).

The author also collaborated with the illustrious Dr. Leonardo Rinzani to perform sub-mm wave pseudowave measurements in support of a NASA Mars Lander project:

(10) L. Ranzani, E. D. Cullens, D. Kuester, K. J. Vanhille, E. Grossman, and Z. Popovic, "W-band micro-fabricated coaxially-fed frequency scanned slot arrays," IEEE Transactions on Antennas and Propagation, accepted for publication.

7.3 Future Work

Since this thesis laid the foundations for RFID backscatter measurement and metric standardization, there are a number of possible future directions that were not addressed in the thesis that would be natural extensions to the work. Among these, the author feels that the following two are of most immediate relevance and straightforward extensions: 1) multiple tone interrogation; and 2) sources of backscatter interference.

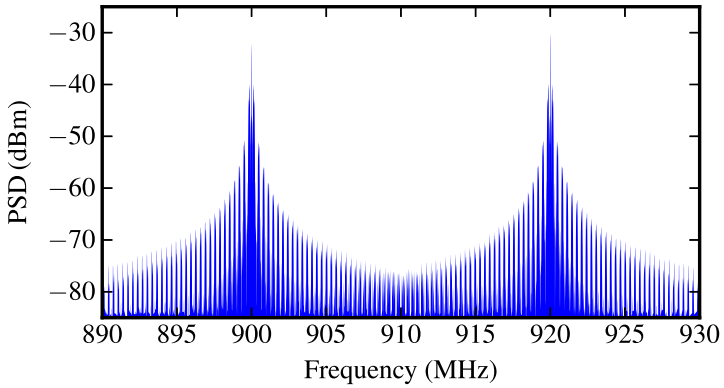

Figure 7.1: Response of a single passive UHF RFID tag chip to two tones. Interrogation modulation is supplied to a connectorized chip at 900 MHz.

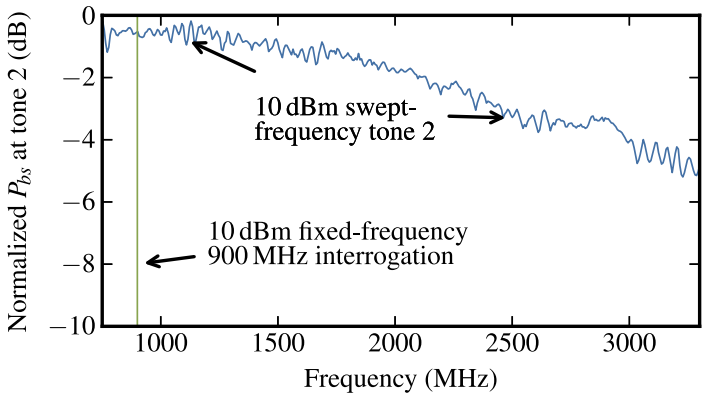

Figure 7.2: Normalized backscattered modulation power from a passive UHF RFID chip at a 2nd tone. The first tone, including the chip interrogation request, is at the same power level at 900 MHz.

Since the LO for passive backscatter communication is the carrier transmitted over the air, the input wave can be chosen arbitrarily and does not need to be a single-tone carrier. If the LO is two-tones, for example, the mixing process, as convolution in the frequency domain, will apply modulation sidebands to both tones. The only condition is that the load modulation must create adequate $\Delta\overline{\rho}_L$ at each frequency. The connectorized UHF RFID chip of Section **??** was excited with the testbed of Chapter 4 at 900 MHz, and an additional tone at 920 MHz. A spectral measurement demonstrates this effect in Fig. 7.1. When the chip is attached to a broad bandwidth impedance like coaxial test circuits, the chip can backscatter power at an very broad range of input frequencies, as in Fig. 7.2 (as long as it is also excited by a tone near UHF).

Publishing reader interference test data could be useful as well, since it is very common in the crowded 900 MHz channels.

The sidebands that are reflected about multiple tones could be leveraged as an approach to frequency diversity, since the same data is reflected at each carrier. The same effect could also be a parasitic source of interference upon other communication systems.

Other obvious directions for future work include extensions to sensing applications [112, 113], and measurements of higher order n-ary modulation, like 4QAM demonstrated in [15].

Finally, the testbed introduced in Chapter 4 is more complex and costly than necessary for commercial testing. A future design could integrate a much simpler monostatic calibration system onto a single circuit board. It would require only (1) calibrated P_{tx}, (2) detection with a high-linearity IQ demodulator, and (3) the calibration device proposed in this paper. In practice, this could be nearly as accurate as that proposed in this paper. One-time calibration with the new reference device needs a single use of a standard network analyzer.

References

[1] *Class-1 Generation-2 UHF RFID Protocol for Communications at 860 MHz - 960 MHz*. Tech. rep. Brussels, BE: GS1 EPCGlobal, 2008 (cit. on pp. 4, 36, 44, 45).

[2] *Radio frequency identification for item management — Parameters for air interface communications at 860 MHz to 960 MHz (Part C)*. Tech. rep. Geneva, CH: ISO/IEC, 2010 (cit. on pp. 4, 36, 102, 130).

[3] C Rosol. *RFID: Vom Ursprung einer(all)gegenw{ä}rtigen Kulturtechnologie*. Berliner (Programm) einer Medienwissenschaft 7.0 / Berliner (Programm) einer Medienwissenschaft. Berlin: Kulturverlag Kadmos, 2007 (cit. on p. 4).

[4] R. Kleinman and R. Mack. "Scattering by linearly vibrating objects". In: *IEEE Trans. Antennas Propag.* 27.3 (1979), pp. 344–352 (cit. on p. 5).

[5] GA Somers and DM Bruno. "Spectral characteristics of electromagnetic wave scattering byrotating propellers and its effect on clutter discrimination". In: *1994 IEEE Ant. Prop. Society Intl. Symposium Digest*. Vol. 1. 1994, pp. 144–147 (cit. on p. 5).

[6] *Erstling IFF transceiver - Wikipedia, the Free Encyclopedia* (cit. on p. 6).

[7] *The Thing (listening device) - Wikipedia, the Free Encyclopedia* (cit. on p. 6).

[8] H Stockman. "Communication by means of reflected power". In: *Proc. IRE* 36 (1948), pp. 1196–1204 (cit. on pp. 5, 6).

[9] A. Glinsky. "Theremin: Ether Music and Espionage". In: Champaign, IL, USA: University of Illinois Press, 2000, pp. 259–273 (cit. on p. 5).

[10] D. M. Dobkin. "The RF in RFID: Passive UHF RFID in Practice". In: Amsterdam; Boston: Elsevier-Newnes, 2008, pp. 7, 211 (cit. on pp. 5, 75).

[11] JH Richmond. "A modulated scattering technique for measurement of field distributions". In: *IRE Trans. Microwave Theory Tech.* 3.4 (1955), pp. 13–15 (cit. on p. 5).

[12] J.C. Bolomey and F.E. Gardiol. *Engineering Applications of the Modulated Scattering Technique*. Boston: Artech House, 2001 (cit. on p. 7).

[13] Tommy Henriksson, Nadine Joachimowicz, Bernard Duchene, et al. "A planar microwave breast imaging system based on the modulated scattering technique". In: *Proc. 5th Eur. Conf. Ant. Prop. (EUCAP)* (2011), pp. 3073–3076 (cit. on p. 7).

[14] Mario W.; Cardullo and William L. Parks III. *Transponder Apparatus and System*. 1973 (cit. on p. 7).

[15] SJ Thomas and Eric Wheeler. "Quadrature amplitude modulated backscatter in passive and semipassive UHF RFID systems". In: *IEEE Trans. Microwave Theory Tech.* (2012), pp. 1–8 (cit. on pp. 9, 162).

[16] Jordan S. Besnoff and Matthew S. Reynolds. "Near field modulated backscatter for in vivo biotelemetry". In: *2012 IEEE Intl. Conf. RFID*. Ed. by Besnoff2012. Apr. 2012, pp. 135–140 (cit. on p. 9).

[17] J. de Heinzelin de Braucourt. "Ishango". In: *Sci. Am.* (June 1962), pp. 105–116 (cit. on p. 11).

[18] Mamokgethi Setati. *African Mathematics*. Lanham, MD, USA: Rowman & Littlefield Publishing Group, Inc, 2011 (cit. on p. 12).

[19] Sean Williams. *The Ishango Bone - The World's Greatest Ancient Artefact?* 2010 (cit. on p. 12).

[20] Adam Schuster. *Hollerith Machine*. 2007 (cit. on p. 13).

[21] *Hollerith's Electric Tabulating Machine*. New York, NY, Apr. 1895 (cit. on p. 13).

[22] H.B. Brainerd. "Identification System". Pat. 3145291 (United States). 1959 (cit. on p. 11).

[23] William G. Crouse and John E. Jones. "Logic Circuit". Pat. 3145291 (United States). 1973 (cit. on p. 11).

[24] Ilhan M. Bilgutay. "Bar Code Font". Patent 3832686 (United States). 1974 (cit. on p. 11).

[25] JF Dickson. "On-chip high-voltage generation in MNOS integrated circuits using an improved voltage multiplier technique". In: *IEEE J. Solid-State Circuits* SC-11.3 (1976), pp. 374–378 (cit. on p. 17).

[26] Erez Falkenstein. "Characterization and Design of a Low-Power Wireless Power Delivery System". PhD thesis. University of Colorado at Boulder, 2011 (cit. on pp. 17, 66).

[27] Ting-wen Xiong, Xi Tan, Jing-tian Xi, et al. "High TX-to-RX Isolation in UHF RFID Using Narrowband Leaking Carrier Canceller". In: *IEEE Microwave Wireless Compon. Lett.* 20.2 (2010), pp. 124–126 (cit. on pp. 18, 102).

[28] Won-Gyu Lim, Seo-Young Park, Wang-Ik Son, et al. "RFID Reader Front-End Having Robust Tx Leakage Canceller for Load Variation". In: *IEEE Trans. Microwave Theory Tech.* 57.5 (May 2009), pp. 1348–1355 (cit. on pp. 18, 102).

[29] P. Pursula, I. Marttila, and K. Nummila. "Wideband adaptive isolator for UHF RFID reader". In: *Electron. Lett* 45.12 (2009), p. 636 (cit. on p. 18).

[30] Hyeong-Seok Jang, Won-Gyu Lim, and Jong-Won Yu. "Transmit/receive isolator for UHF RFID reader with wideband balanced directional coupler". In: *Proc. 2009 Asia Pacific Microwave Conf.* IEEE, Dec. 2009, pp. 233–236 (cit. on pp. 18, 102).

[31] Deogracias P. Villame and Joel S. Marciano. "Carrier suppression locked loop mechanism for UHF RFID readers". In: *Proc. 2010 Intl. Conf. RFID*, pp. 141–145 (cit. on p. 18).

[32] K. Penttila, L. Sydanheimo, and M. Kivikoski. "Implementation of Tx/Rx isolation in an RFID reader". In: *Int. J. Radio Freq. Identif. Technol. Appl.* 1.1 (2006), pp. 74–89 (cit. on p. 18).

[33] C Jin, SH Cho, and KY Jeon. "Performance Evaluation of RFID EPC Gen2 Anti-collision Algorithm in AWGN Environment". In: *Proc. 2007 Conf. Mechatronics Automation* (2007), pp. 2066–2070 (cit. on p. 20).

[34] Ki Yong Jeon and Sung Ho Cho. "Performance of RFID EPC C1 Gen2 Anti-collision in Multipath Fading Environments". In: *Proc. 2009 Second Intl. Conf. Comm. Theory, Reliability, Quality Service*. July 2009, pp. 125–128 (cit. on pp. 20, 137).

[35] J.D. Porter, R.E. Billo, and M.H. Mickle. "Effect of active interference on the performance of radio frequency identification systems". In: *Int. J. Radio Freq. Identif. Technol. Appl.* 1.1 (2006), pp. 4–23 (cit. on p. 20).

[36] L. Zhu and T.S.P. Yum. "The Optimal Reading Strategy for EPC Gen-2 RFID Anti-Collision Systems". In: *IEEE Trans. Commun.* 58.9 (2010), pp. 2725–2733 (cit. on p. 20).

[37] Ping Wang, Aiqun Hu, and Wenjiang Pei. "The Design of Anti-collision Mechanism of UHF RFID System based on CDMA". In: *IEEE Asia Pacific Conf. Circuits Systems, 2006. APCCAS 2006*. Vol. 00. 2006, pp. 1703–1708 (cit. on p. 20).

[38] *ISO/IEC 18046-3: Radio frequency identification device performance test methods — Test methods for tag performance*. Tech. rep. 2007 (cit. on pp. 20, 74, 109).

[39] Daniel G Kuester, David R Novotny, and Jeffrey R Guerrieri. "Forward and Reverse Link Constraints in UHF RFID with Passive Tags". In: *Proc. 2010 IEEE Symposium Electromagnetic Compatibility*. 2010, pp. 680–685 (cit. on pp. 20, 21, 74).

[40] M.R. Souryal, D.R. Novotny, D.G. Kuester, et al. “Impact of RF Interference between a Passive RFID System and a Frequency Hopping Communications System in the 900 MHz ISM Band”. In: *Proc. 2010 IEEE Symposium Electromagnetic Compatibility*. 2010, pp. 495–501 (cit. on pp. 21, 64).

[41] *Radio frequency identification device conformance test methods — Test methods for air interface communications at 860 MHz to 960 MHz*. Tech. rep. ISO/IEC standard 18047-6, 2006 (cit. on pp. 21, 36, 59, 65, 75, 79, 109, 114).

[42] PV Nikitin and KVS Rao. “Theory and measurement of backscattering from RFID tags”. In: *IEEE Antennas Propag. Mag.* 48.6 (2006), pp. 212–218 (cit. on pp. 21, 75).

[43] J.C. Bolomey, Santiago Capdevila, L. Jofre, et al. “Electromagnetic Modeling of RFID-Modulated Scattering Mechanism. Application to Tag Performance Evaluation”. In: *Proc. IEEE* 98.9 (2010), pp. 1555–1569 (cit. on pp. 21, 37, 63, 69, 75, 78, 80).

[44] S. Skali, C. Chantepy, and S. Tedjini. “On the measurement of the delta Radar Cross Section (ΔRCS) for UHF tags”. In: *Proc. 2009 Intl. Conf. RFID*. IEEE, Apr. 2009, pp. 346–351 (cit. on pp. 21, 36, 50, 69, 75, 116).

[45] A Pouzin, T P Vuong, S Tedjini, et al. “Determination of measurement uncertainties applied to the RCS and the differential RCS of UHF passive RFID tags”. In: *2009 IEEE Ant. Prop. Society Intl. Symposium Digest*. 2009, pp. 1–4 (cit. on pp. 21, 112).

[46] D.G. Kuester, D.R. Novotny, J.R. Guerrieri, et al. “Reference Modulation for Calibrated Measurements of Tag Backscatter”. In: *Proc. IEEE Conf. RFID*. 2011, pp. 154–161 (cit. on pp. 21, 37, 63, 112).

[47] D Gabor. “Theory of communication. Part 1: The analysis of information”. In: *Journal IEEE Part III: Radio Comm.* 93.26 (1946), pp. 429–441 (cit. on p. 22).

[48] Mathias Johansson. “The hilbert transform”. Master’s Thesis. Vaxjo University, 2004 (cit. on pp. 22, 24).

[49] E Bedrosian. “A product theorem for Hilbert transforms”. In: *Proc. IEEE* 21.5 (1963), pp. 868–869 (cit. on p. 23).

[50] Yuesheng Xu. “The Bedrosian identity for the Hilbert transform of product functions”. In: *Proc. American Mathematical Society* 134.9 (2006), pp. 2719–2728 (cit. on p. 23).

[51] Boualem Boashash. “Estimating and interpreting the instantaneous frequency of a signal. I. Fundamentals”. In: *Proc. IEEE* 80.4 (1992) (cit. on p. 23).

[52] John W. Pierre and Ph.D Robert Kubichek. *Spectral Analysis: Analyzing a Signal Spectrum (Application Note)*. Tech. rep. Tektronix, Inc., 2002, p. 2 (cit. on p. 23).

[53] Christoph Rauscher. *Fundamentals of Spectrum Analysis*. 1st. Munich, DE: Rohde & Schwarz, 2001, p. 11 (cit. on p. 23).

[54] *The Fundamentals of Signal Analysis, Application Note 243*. Tech. rep. Agilent, p. 63 (cit. on p. 23).

[55] R.B. Marks and Dylan F. Williams. “A General Circuit Waveguide Theory”. In: *J. Res. Nat. Inst. Stand. Technol.* 97.5 (1992), pp. 533–556 (cit. on pp. 24, 25).

[56] D.M Kerns and R.W. Beatty. “Basic Theory of Waveguide Junctions and Introductory Microwave Network Analysis”. In: Oxford: Pergamon Press, 1967, pp. 56–60 (cit. on pp. 24, 25, 29, 39, 63).

[57] K. Kurokawa. “Power Waves and the Scattering Matrix”. In: *IEEE Trans. Microwave Theory Tech.* 13.2 (Mar. 1965), pp. 194–202 (cit. on pp. 25, 26).

[58] D.F. Williams and R.B. Marks. “Comments on "Conversions between S, Z, Y, h, ABCD, and T parameters which are valid for complex source and load impedances" [and reply]”. In: *IEEE Trans. Microwave Theory Tech.* 43.4 (Apr. 1995), pp. 914–915 (cit. on p. 26).

[59] AA Muller, Pablo Soto, Dan Dascalu, et al. “A 3-D Smith Chart Based on the Riemann Sphere for Active and Passive Microwave Circuits”. In: *IEEE Microwave Wireless Compon. Lett.* 21.6 (2011), pp. 286–288 (cit. on p. 26).

[60] SF Adam. “A new precision automatic microwave measurement system”. In: *IEEE Trans. Instrum. Meas.* IM.4 (1968), pp. 308–313 (cit. on p. 26).

[61] Arkadiusz Lewandowski. “Covariance-Based Vector-Network-Analyzer Uncertainty Analysis for Time-and Frequency-Domain Measurements”. In: *IEEE Trans. Microwave Theory Tech.* 58.7 (2010), pp. 1877–1886 (cit. on p. 26).

[62] David M. Pozar. *Microwave Engineering*. 3rd. Hoboken, NJ: Wiley & Sons, 2005 (cit. on pp. 27, 64).

[63] *Evaluation of measurement data — Guide to the expression of uncertainty in measurement*. Tech. rep. September. Sèvres, France: Bureau International des Poids et Mesures, 2008 (cit. on p. 29).

[64] BN Taylor. “NIST Technical Note 1297: guidelines for evaluating and expressing the uncertainty of NIST measurement results”. In: (1994) (cit. on p. 29).

[65] I.a. Harris and F.L. Warner. “Re-examination of mismatch uncertainty when measuring microwave power and attenuation”. In: *IEE Proc. Microwaves, Optics Ant.* 128.1 (1981), p. 35 (cit. on pp. 31, 129).

[66] P. Miller. “Uncertianty Considerations in Spherical Near-Field Antenna Measurements”. In: *2007 Eur. Conf. Ant. Prop.* IET, 2008, pp. 1–7 (cit. on pp. 31, 129).

[67] Giuseppe De Vita. “Design criteria for the RF section of UHF and microwave passive RFID transponders”. In: *IEEE Trans. Microwave Theory Tech.* 53.9 (2005), pp. 2978–2990 (cit. on p. 36).

[68] Udo Karthaus. “Fully integrated passive UHF RFID transponder IC with 16.7-μW minimum RF input power”. In: *IEEE J. Solid-State Circuits* 38.10 (2003), pp. 1602–1608 (cit. on pp. 36, 37).

[69] Robert Blair Green. “The general theory of antenna scattering”. PhD thesis. The Ohio State University, 1963 (cit. on pp. 36, 53, 69, 75, 77–79).

[70] Pavel V. Nikitin, Rene Martinez, Shashi Ramamurthy, et al. “Phase based spatial identification of UHF RFID tags”. In: *Proc. 2010 IEEE Intl. Conf. RFID*. Apr. 2010, pp. 102–109 (cit. on pp. 36, 76).

[71] DG Kuester, DR Novotny, J.R. Guerrieri, et al. “Simple Test and Modeling of RFID Tag Backscatter”. In: *IEEE Trans. Microwave Theory Tech.* 60.7 (2012), pp. 2248–2258 (cit. on pp. 37, 53, 69, 78, 100, 110).

[72] K. Seemann and R. Weigel. “The system design of integrated passive transponder devices”. In: *2006 Asia-Pacific Microwave Conf.* 2006, pp. 1114–1117 (cit. on p. 39).

[73] Daniel Arnitz and Ulrich Muehlmann. “Wideband characterization of backscatter channels”. In: *Eur. Wireless 2011*. 2011, pp. 205–211 (cit. on p. 41).

[74] R.W. Lucky and J.C. Hancock. “On the optimum performance of N-ary systems having two degrees of freedom”. In: *Systems, IRE Transactions* 14.6 (1962), pp. 185–192 (cit. on p. 42).

[75] Richard Haberman. *Applied Partial Differential Equations with Fourier Sieries and Boundary Value Problems*. 2004th ed. Saddle River, NJ: Pearson Education, 2004, p. 469 (cit. on p. 44).

[76] Alan V. Oppenheim. *Signal and Systems*. 2nd. Englewood Cliffs, New Jersey: Prentice-Hall, 1983 (cit. on p. 50).

[77] PV Nikitin, KVS Rao, and RD Martinez. “Differential RCS of RFID tag”. In: *Electron. Lett* 43.8 (2007), pp. 431–432 (cit. on pp. 53, 57, 69, 78, 79).

[78] F Fuschini, C Piersanti, F Paolazzi, et al. “Analytical Approach to the Backscattering from UHF RFID Transponder”. In: *IEEE Antennas Wirel. Propag. Lett.* 7 (2008), pp. 33–35 (cit. on pp. 53, 57, 79).

[79] K Penttila and M Keskilammi. “Radar cross-section analysis for passive RFID systems”. In: *IEE Proc. Microwaves, Ant. Prop.* 153.1 (2006), pp. 103–109 (cit. on pp. 55, 79).

[80] Anna Aleksieieva and Martin Vossiek. “Design and optimization of amplitude-modulated microwave backscatter transponders”. In: *German Microwave Conf., 2010*. Vol. 8. c. IEEE, 2010, pp. 134–137 (cit. on pp. 55, 79).

[81] Danilo De Donno, Luca Catarinucci, Riccardo Colella, et al. “Differential RCS and sensitivity calculation of RFID tags with Software-Defined Radio”. In: *2012 IEEE Radio Wireless Symposium*. Ieee, Jan. 2012, pp. 9–12 (cit. on pp. 55, 79).

[82] Antonis G. Dimitriou, Aggelos Bletsas, and John N. Sahalos. “Practical Considerations of ASK Modulated Passive Tags”. In: *Proc. Eur. Conf. Ant. Prop. (EUCAP)*. 2011, pp. 3476–3480 (cit. on p. 55).

[83] Bernard Sklar. *Digital Communications*. 2nd. Prentice-Hall, 1988 (cit. on p. 61).

[84] Franco Fuschini, Carmine Piersanti, Francesco Paolazzi, et al. “On the Efficiency of Load Modulation in RFID Systems Operating in Real Environment”. In: *IEEE Antennas Wirel. Propag. Lett.* 7 (2008), pp. 2008–2011 (cit. on pp. 61, 64).

[85] J D Griffin and G D Durgin. “Complete Link Budgets for Backscatter-Radio and RFID Systems”. In: *IEEE Antennas Propag. Mag.* 51.2 (Apr. 2009), pp. 11–25 (cit. on p. 61).

[86] JD Griffin. “Gains for RF tags using multiple antennas”. In: *Ant. Prop., IEEE* 56.2 (2008), pp. 563–570 (cit. on p. 62).

[87] L.W. Mayer and A.L. Scholtz. “Sensitivity and impedance measurements on UHF RFID transponder chips”. In: *Int EURASIP Workshop RFID Techn.,* 2007, pp. 1–10 (cit. on pp. 63, 68, 132).

[88] R.W.P. King. *The theory of linear antennas*. Boston: Harvard University Press, 1956 (cit. on p. 66).

[89] JK Ryoo, JY Choo, and H Park. “Full wave simulation of flip-chip packaging effects on RFID transponder”. In: *Proc. 2007 IEEE Intl. Conf. RFID* (2007), pp. 37–40 (cit. on p. 66).

[90] Hannes Reinisch, Gunter Hofer, Stefan Gruber, et al. “A fully EPC compatible Multi frequency Passive RFID Tag with -11.4 dBm Sensitivity”. In: *2011 IEEE Intl. Conf. RFID-Technologies Applications*. Ieee, Sept. 2011, pp. 207–213 (cit. on p. 67).

[91] *Impinj ® Monza ® X-2K Dura Datasheet*. Tech. rep. Impinj, 2012 (cit. on p. 68).

[92] *NXP UCODE G2iM and G2iM+ Datasheet*. Tech. rep. February. NXP Semiconductors, 2012 (cit. on p. 68).

[93] Jari-Pascal Curty, Michel Declercq, Catherine Dohollain, et al. *Design and Optimization of Passive UHF RFID Systems*. New York: Springer, 2007 (cit. on p. 68).

[94] P.V. Nikitin and K. Rao. “Effect of Gen2 protocol parameters on RFID tag performance”. In: *Proc. 2009 Intl. Conf. RFID*. Apr. 2009, pp. 117–122 (cit. on pp. 68, 102).

[95] Stoyan Iliev, Johann-Friedrich Luy, and Robert Weigel. “Read Range and Power Efficiency of the UHF RFID Systems”. In: *2009 German Microwave Conf.* 2 (Mar. 2009), pp. 1–5 (cit. on p. 69).

[96] C.A. Balanis. *Antenna Theory: Analysis and design*. 3rd. Hoboken, NJ, 2005 (cit. on pp. 72, 77).

[97] Erez Falkenstein, Michael Roberg, and Zoya Popović. “Low-Power Wireless Power Delivery”. In: *IEEE Trans. Microwave Theory Tech.* 60.7 (2012), pp. 2277–2286 (cit. on p. 74).

[98] *IEEE Standard 145: Standard Definitions of Terms for Antennas*. Tech. rep. IEEE, 1993 (cit. on p. 75).

[99] A Pouzin, T P Vuong, S Tedjini, et al. “Bench test for measurement of differential RCS of UHF RFID tags”. In: *Electron. Lett* 46.8 (Apr. 2010), pp. 590–592 (cit. on p. 75).

[100] RC Hansen. “Relationships between antennas as scatterers and as radiators”. In: *Proc. IEEE* 77.5 (1989), pp. 659–662 (cit. on p. 78).

[101] J C Bolomey and F Gardiol. “Optimization of passive RFID tag antennas”. In: *2008 IEEE Ant. Prop. Society Intl. Symposium Digest*. 2008, pp. 1–4 (cit. on p. 78).

[102] Pekka Pursula, Mervi Hirvonen, Kaarle Jaakkola, et al. “Antenna effective aperture measurement with backscattering modulation”. In: *IEEE Trans. Antennas Propag.* 55.10 (2007), pp. 2836–2843 (cit. on p. 79).

[103] Bomson Lee. “Review of RFID tag antenna issues at UHF band”. In: *2008 Asia-Pacific Microwave Conf.* 2008, pp. 1–4 (cit. on p. 79).

[104] M Nikkari, T Bjorninen, L Sydanheimo, et al. “Performance of a passive UHF RFID tag in reflective environment”. In: *2008 IEEE Ant. Prop. Society Intl. Symposium Digest*. 2008, pp. 1–4 (cit. on p. 79).

[105] A Bletsas, A G Dimitriou, and J N Sahalos. “Improving Backscatter Radio Tag Efficiency”. In: *IEEE Trans. Microwave Theory Tech.* PP.99 (2010), p. 1 (cit. on p. 79).

[106] A Pouzin, Tan-Phu Vuong, S Tedjinp, et al. “Measurement of Radar Cross Section for Passive UHF RFID Tags”. In: *2007 Eur. Conf. Ant. Prop.* 2007, pp. 1–6 (cit. on p. 79).

[107] Jong-Wook Lee, Hongil Kwon, and B Lee. “Design Consideration of UHF RFID Tag for Increased Reading Range”. In: *2006 IEEE MTT-S Intl. Microwave Symposium Digest*. 2006, pp. 1588–1591 (cit. on p. 79).

[108] C.C. Yen, AE Gutierrez, D Veeramani, et al. “Radar cross-section analysis of backscattering RFID tags”. In: *IEEE Antennas Wirel. Propag. Lett.* 6 (2007), pp. 279–281 (cit. on p. 79).

[109] L Sydanheimol, J Nummela, L Ukkonen, et al. “Characterization of Passive UHF RFID Tag Performance”. In: *IEEE Antennas Propag. Mag.* 50.3 (June 2008), pp. 207–212 (cit. on p. 79).

[110] E Colin, A Moretto, C Ripoll, et al. “Delta RCS of UHF RFID taking into account the shunt resistance in the tag model”. In: *2009 IEEE North-East Workshop*. June 2009, pp. 1–4 (cit. on p. 79).

[111] J.C. Bolomey, Luis Jofre, and Santiago Capdevila. “Reciprocity-based formulation of RFID tag response in arbitrary environments”. In: *2008 Intl. Symposium Ant. Prop.* 1. 2008 (cit. on p. 80).

[112] Gaetano Marrocco. “RFID Grids : Part I — Electromagnetic Theory”. In: *IEEE Trans. Antennas Propag.* 59.3 (2011), pp. 1019–1026 (cit. on pp. 80, 110, 162).

[113] Stefano Caizzone. “RFID Grids : Part II — Experimentations”. In: *IEEE Trans. Antennas Propag.* 59.8 (2011), pp. 2896–2904 (cit. on pp. 80, 110, 146, 162).

[114] *IEEE Std 181-2003: Standard on Transitions, Pulses, and Related Waveforms*. Tech. rep. Institute of Electrical and Electronics Engineers, 2003 (cit. on p. 104).

[115] Paul D. Hale and C. M. Jack Wang. “Calculation of Pulse Parameters and Propagation of Uncertainty”. In: *IEEE Trans. Instrum. Meas.* 58.3 (Mar. 2009), pp. 639–648 (cit. on p. 104).

[116] John Canny. “A Computational Approach to Edge Detection”. In: *IEEE Trans. Pattern Anal. Mach. Intell.* PAMI-8.6 (Nov. 1986), pp. 679–698 (cit. on p. 104).

[117] LA Goodman. “On the exact variance of products”. In: *Journal American Statistical Society* 55.292 (1960), pp. 708–713 (cit. on p. 111).

[118] J. H. Van Vleck, F. Bloch, and M. Hamermesh. “Theory of Radar Reflection from Wires or Thin Metallic Strips”. In: *J. Appl. Phys.* 18.3 (1947), p. 274 (cit. on p. 115).

[119] VV Liepa and S Chang. “Measured back scattering cross section of thin wires”. In: *1999 IEEE Ant. Prop. Society Symposium Digest* 33.8077 (1999), pp. 1980–1982 (cit. on p. 115).

[120] David R Novotny, Daniel G. Kuester, and Jeffrey R. Guerrieri. “A reference modulated scatterer for ISO18000-6 UHF tag testing”. In: *IEEE Electromagnetic Compatibility Magazine* 1.3 (July 2012), pp. 103–106 (cit. on p. 126).

[121] P.V. Nikitin, K.V.S. Rao, R. Martinez, et al. “Sensitivity and Impedance Measurements of UHF RFID Chips”. In: *IEEE Trans. Microwave Theory Tech.* 57.5 (May 2009), pp. 1297–1302 (cit. on p. 130).

[122] Xianming Qing, Chean Khan Goh, and Zhi Ning Chen. “Impedance Characterization of RFID Tag Antennas and Application in Tag Co-Design”. In: *IEEE Trans. Microwave Theory Tech.* 57.5 (May 2009), pp. 1268–1274 (cit. on p. 130).

[123] Hiroyuki Yojima, Yu Tanaka, Yohtaro Umeda, et al. “Dynamic impedance measurement of UHF passive RFID tags for sensitivity estimation”. In: *2010 Intl. Symposium Comm. Information Technologies*. IEEE, 2010, pp. 344–349 (cit. on p. 132).

[124] R. W. Beatty and D. M. Kerns. “Recently Developed Microwave Impedance Standards and Methods of Measurement”. In: *IRE Trans. Instrum.* I-7.3 (Dec. 1958), pp. 319–321 (cit. on p. 132).

[125] Joshua Griffin and Gregory Durgin. “Link Envelope Correlation in the Backscatter Channel”. In: *IEEE Commun. Lett.* 11.9 (Sept. 2007), pp. 735–737 (cit. on p. 137).

[126] JD Griffin. “Multipath Fading Measurements at 5.8 GHz for Backscatter Tags With Multiple Antennas”. In: *IEEE Trans. Antennas Propag.* 58.11 (2010), pp. 3693–3700 (cit. on p. 137).

[127] Lukas W. Mayer, Martin Wrulich, and Sebastian Caban. “Measurements and channel modeling for short range indoor UHF applications”. In: *Proc. 2006 Eur. Conf. Ant. Prop.* Vol. 2006. October. Nov. 2006, pp. 1–5 (cit. on p. 137).

[128] H.G. Wang, C.X. Pei, and C.H. Zhu. “A Link Analysis for Passive UHF RFID System in LOS Indoor Environment”. In: *2008 Intl. Conf. Wireless Comm., Networking Mobile Computing*. IEEE, Oct. 2008, pp. 1–7 (cit. on p. 137).

[129] W. Su, K.M. Beilke, and T.T. Ha. “A Reliability Study of RFID Technology in a Fading Channel”. In: *Conf. Record 2007 Signals, Systems Computers*. IEEE, 2008, pp. 2124–2127 (cit. on p. 137).

[130] J.W. Jung, J.H. Hwang, Y.J. Moon, et al. “Multipath fading measurement on the circularly propagated UHF RFID reader antennas in a practical area”. In: *2008 Asia-Pacific Symposium Electromagnetic Compatibility*. May. 2008, pp. 315–318 (cit. on p. 137).

Appendix A

Backscatter Link Variables and Notation

Variable	Description
$\bar{p}$	Tag operating point parameter, or "excess available power" ($\bar{p} = P_{tx}/P_{tx0} = P_3/P_{30}$)
P_3	Available power to tag chip
P_{30}	Minimum available power from loaded port 3 of E to turn on a tag chip
P_{bs}	Received BPSK modulation power
P_L	Delivered power into a tag chip (power harvesting state)
P_{L0}	Minimum P_L for tag turn-on, "tag chip sensitivity"
P_{tx}	Available transmit power from a reader port
P_{tx0}	Minimum available transmit power from a reader port to turn on a tag

Power

Table A.1: (continued)

ρ_3	Tag antenna reflection coefficient (E_{33} loaded by the reader)
$\rho_{bs}(t)$	Time-varying reflection coefficient with tag load modulation (monostatic reader)
ρ_{In}	Reflection coefficient of reader port n
$\overline{\rho}_n$	Time-averaged† reflection coefficient of port n loaded by the tag
ρ_L	Linearized reflection coefficient of the tag chip (power harvesting state)
ρ_L	Linearized reflection coefficient of the tag chip (reflective state)
$\tau_{bs}(t)$	Time-varying transmission coefficient with tag load modulation (bistatic reader)
$[E]$	Three-port scattering parameter network representing communication channel effects

Pseudowave scattering parameters

†Averaged over a large integer number of tag modulation symbols

Z_3	Input impedance at port 3 of E, with ports 1 and 2 loaded by a transceiver
Z_L	Tag chip input impedance (power harvesting state), including bonding parasitics
Z_R	Tag chip input impedance (reflective modulation state), including bonding parasitics

Impedance parameters

$\tilde{\rho}_L$	Power wave reflection coefficient between tag chip and antenna (power harvesting state)
$\tilde{\rho}_R$	Power wave reflection coefficient between tag chip and antenna (reflective modulation state)

Power wave parameters

Table A.1: (continued)

η_L	Power delivered to a tag chip, relative to an ideal conjugate match to the antenna
η_{L0}	η_L at the minimum turn-on operating point
η_{mod}	Tag backscatter modulation power relative to incident power
η_{rx}	Power absorbed by reader receiver, relative to a Z_0-matched receiver
η_{tx}	Power accepted by reader transmit antenna, relative to a Z_0-matched transmit antenna
	Circuit Efficiencies
L_{bs}	Backscatter path loss
L_{mod}	$-10\log_{10}\eta_{mod}$
L_L	$-10\log_{10}\eta_L$
L_{rx}	
L_{tx}	$-10\log_{10}\eta_{tx}$
	Link Losses

Table A.1: Passive UHF RFID Link Parameters